

Doctoral Thesis

Designing Ionic Pathways to Improve Overall
Kinetics of Lithium ion Batteries

Tae-Hee Kim

Department of Energy Engineering
(Battery Science and Technology)

Graduate School of UNIST

2015

Designing Ionic Pathways to Improve Overall Kinetics of Lithium ion Batteries

Tae-Hee Kim

Department of Energy Engineering
(Battery Science and Technology)

Graduate School of UNIST

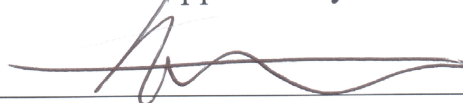
Designing Ionic Pathways to Improve Overall Kinetics of Lithium ion Batteries

A thesis/dissertation
submitted to the Graduate School of UNIST
in partial fulfillment of the
requirements for the degree of
Doctor of Philosophy

Tae-Hee Kim

7. 17. 2015

Approved by



Advisor

Hyun-Kon Song

Designing Ionic Pathways to Improve Overall Kinetics of Lithium ion Batteries

Tae-Hee Kim

This certifies that the thesis/dissertation of Tae-Hee Kim is approved.

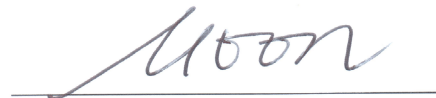
7. 17. 2015



Advisor: Hyun-Kon Song



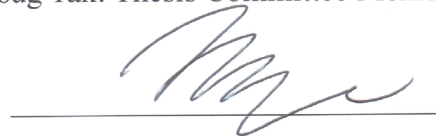
Jaephil Cho: Thesis Committee Member #1



Hoi Ri Moon: Thesis Committee Member #2



Yongsug Tak: Thesis Committee Member #3



Joo-Hwan Sung: Thesis Committee Member #4

Abstract

Lithium-ion batteries (LIBs) have been considered as the most attractive energy storage systems. They have been used in a wide range of applications from portable devices to large-scale stationary energy storage systems (ESSs) due to their merits superior to other energy storage systems such as lead-acid, Na-S, and redox flow batteries. They have higher cell voltages at > 3.6 V, higher efficiencies at > 90 % and longer cycle life when compared with their alternatives. However, more research and development activities would be required before large-scale LIBs are widely spread for automotive and stationary fields. Power densities as well as energy densities should be improved higher with cost reduction.

Many efforts have been devoted to not only discovering high-performance active materials but also enhancing ionic and electric conductivities. In order to increase ionic conductivities, smaller particles in a nanoscale level are favored to give larger surface area and shorter ionic diffusion length. Electric conductivities are enhanced by coating active materials with conductive materials such as metallic and carbonaceous compounds. The main topic of this thesis is how to design ionic pathways for improving overall kinetics of LIBs even if electric conductivity enhancement is involved. As the simplest strategy which can be used as a startup, nanosizing in the primary particle level was tried for LiMnPO_4 olivine (LMP) to overcome its poor electric and ionic conductivities. By confining $\text{Mn}_3(\text{PO}_4)_2$ precipitation on surface of a precursor seed of Li_3PO_4 , the size of LMP particles is limited to less than 100 nm for a smaller dimension. Larger active area and shorter ionic transport length resulting from the nanosizing improved kinetic properties of LMP as a cathode material for LIB cells. When compared with LMP particles synthesized by a conventional co-precipitation method, the performances are recognized to be considerably enhanced.

As the next strategy, the primary-particle-level nanosizing was evolved to the secondary-structure level of morphology control. Hollow structures with porous shells were designed for a conversion-reaction-based anode material Fe_3O_4 . The structure was chosen because hollow particles benefit from larger surface area on which active materials meet electrolyte, shorter pathways for lithium ions to pass through and voids within hollow shell providing buffer space during lithiation. The hollow structure was proved more beneficial in terms of electrochemical performances when compared with its non-hollow counterpart. Hollow void of ~ 80 nm diameter accommodated volume expansion during lithiation while the porous shell structure allowed lithium ions move through in a facile manner and enhanced accessibility to surface of the active materials.

As the third strategy of morphological control following primary- and secondary-structure levels, higher level structures were designed for another conversion-reaction-based anode materials, Co_3O_4 .

Two different morphologies of Co_3O_4 (plate-like and rod-like) were achieved through pseudomorphic conversion, depending on macroscopic morphologies of parent metal-organic-frameworks (MOFs). Both Co_3O_4 nanostructures were composed of almost identical 10 nm-sized primary nanocrystals. These Co_3O_4 nanomaterials were utilized as an electrode in lithium ion batteries (LIBs), and their electrochemical properties were comparatively investigated. It was revealed that the different cyclability and rate capability are attributed to their different microstructures. The pseudo-monolithic integration of primary and secondary structures at higher level was the governing factor, which determined the electrochemical performances of the Co_3O_4 electrode.

In addition to the morphology controls in nanoscales, crystallographic parameters of graphite as an anode material were controlled for the same purpose of improving ionic conduction or transport during faradaic reactions. To widen the ionic pathways inside active materials, the d-spacing of graphite increased from 0.3359 nm to 0.3395 nm by oxidizing natural graphite under a mild condition. Oxygen-containing functional groups were developed not only at edges but also on planes of graphite. Subsequent thermal reduction of the oxidized graphite eliminated a portion of the functional groups, but did not change d-spacing significantly. The enlargement of d-spacing reduced kinetic hindrance of lithium ion movement within the expanded graphite by reserving more space for the ionic transport route. In addition, the activation energy of lithium ion intercalation in expanded graphite are reduced by surface charge polarization of graphite induced by hydrogen bonds between oxygen atoms of carbonates in electrolytes and hydrogen atoms of surface functional groups. The expanded graphite showed higher delithiation capacities especially at high currents.

By designing ionic pathways of electroactive materials, overall kinetics was enhanced, resulting in a much better improved electrochemical storage system.

Keywords: lithium ion batteries (LIBs), morphology, kinetics, ionic conductivity, electric conductivity, lithium manganese phosphate, iron oxides, cobalt oxides, expanded graphite

Contents

Abstract	i
Contents	iii
List of Figures	v
List of Tables	x
Chapter 1. Introduction	1
1.1 Lithium-ion Batteries (LIBs)	1
1.1.1 Principle of LIBs.....	1
1.1.2 Characteristics of LIBs	2
1.1.3 Cathode materials.....	3
1.1.4 Anode materials	5
1.2 Strategies to Improve the Kinetics of LIBs.....	6
1.2.1 Ionic Transport.....	7
1.2.2 Li Solid-State Diffusion.....	8
1.2.3 Electron transport.....	8
1.3 Research purpose	9
Chapter 2. Restricted growth of LiMnPO₄ nanoparticles evolved from a precursor seed	11
2.1 Introduction.....	11
2.2 Experiments	11
2.2.1 Preparation	11
2.2.2 Cell construction	13
2.3 Results and discussion	13
2.3.1 Preparation	13
2.3.2 Electrochemical performances	18
2.4 Conclusion	19
Chapter 3. Hollow versus non-hollow: The electrochemical preference in a case study of the conversion reaction of Fe₃O₄	20
3.1 Introduction.....	20

3.2 Experiments	21
3.2.1 Preparation	21
3.2.2 Electrochemical analysis.....	22
3.3 Results and discussion	23
3.3.1 Morphological evolution of hollow structure	23
3.3.2 Electrochemical preference of hollowness to non-hollowness	28
3.4 Conclusion	31
Chapter 4. Preparation of Co₃O₄ electrode materials with different microstructures via pseudomorphic conversion of Co-based metal-organic frameworks	32
4.1 Introduction.....	32
4.2 Experiments	33
4.2.1 Electrochemical measurements.....	33
4.3 Results and discussion	33
4.4 Conclusion	38
Chapter 5. Enlarging the d-spacing of graphite and polarizing its surface charge for driving lithium ions fast	39
5.1 Introduction.....	39
5.2 Experiments	40
5.2.1 Mild oxidation of graphite to EG* and subsequent thermal reduction of EG* to EG	40
5.2.2 Characterization	40
5.3 Results and discussion	41
5.4 Conclusion	54
Chapter 6. Summary	56
Chapter 7. References.....	57
Chapter 8. Acknowledgement.....	67

List of Figures

Figure 1.1. Working scheme of conventional lithium-ion batteries (LIBs).

Figure 1.2. The crystal structure of (a) layered structure, (b) spinel structure, and (c) olivine structure.

Figure 1.3. Various cathode materials according to the order in development.

Figure 1.4. The factors to influence on kinetics in the viewpoint of ionic and electron transports.

Figure 1.5. Four strategies to enhance the kinetics in this thesis.

Figure 2.1. Synthesis of LMP via two different strategies for precipitation: (a) surface-confined precipitation and (b) co-precipitation.

Figure 2.2. (a-i) Schematic illustrations and electron microscopy images of LMP particles from each step of the surface-confined precipitation: (a-c) the first precipitates (Li_3PO_4) (d-f) the mixture of the first (orange) and the second (green) particles obtained after the second precipitation; (g-i) the sample obtained after calcination. (j-k) Schematic illustrations and electron microscopy images of co-precipitated LMP as a control for comparison.

Figure 2.3. X-ray diffraction patterns of the first intermediate precipitate (Li_3PO_4 , a and b), the mixed intermediate precipitate ($\text{Li}_3\text{PO}_4 + \text{Mn}_3(\text{PO}_4)_2$, c), the thermally treated one (LiMnPO_4 , d) and carbon-coated one (LiMnPO_4 , e) obtained through each step of the surface-confined precipitation. For a comparison, the co-precipitated LMP is shown (f).

Figure 2.4. (a) A representative transmission-electron-microscopic (TEM) image of a single carbon-coated LMP particle with its Fourier-transformed pattern as an inset. (b) A line mapping of the constituents of a single carbon-coated LMP particle in the same scale of (a). (c) Raman spectra of bare LMP (black, intensity-magnified by $10\times$) and carbon-coated LMP (red). (d) X-ray diffraction (XRD) pattern of carbon-coated LMP. There was no significant difference between bare and carbon-coated LMPs in terms of the XRD pattern.

Figure 2.5. (a–c) Potential profiles of half coin cells of sequentially precipitated LMP (seq-LMP, a and c) and co-precipitated LMP (co-LMP, b). $1C = 150 \text{ mAh g}^{-1}$. The cells in a and b were charged at $0.04 C$ up to 4.5 V followed by keeping the potential until current flowed below a hundredth of the charging current. Then they were discharged at various C rates as indicated. The cells in c were charged at various C rates of constant current as indicated (not followed by keeping them at constant voltage). Then they were discharged at $0.04 C$ immediately after being charged. (d) C -rate dependency of plateau potential (E_{plateau}) during discharge or charge. Red solid circle, seq-LMP during discharge; red open circle, seq-LMP during charge; black open square, co-LMP during discharge.

Figure 3.1. Ratio of surface-to-volume ratios (S/V) of hollow to non-hollow sphere geometry as the function of dimensionless number of shell thickness to particle radius of the hollow sphere at mass = constant with the assumption of density = constant (a) and at apparent volume = constant (b).

Figure 3.2. Evolution from carbon balls (CBall, a-c) via Fe^{3+} -adsorbed CBall (C@Fe^{3+} , d-f) and hollow-sphere-structured Fe_2O_3 (h- Fe_2O_3 , g-i) to carbon-coated hollow-sphere-structured Fe_3O_4 (h- $\text{Fe}_3\text{O}_4\text{@C}$, j-l): schematic diagrams for the first column; scanning electron microscopic (SEM) images for b and e; and transmission electron microscopic (TEM) images for others. White arrow in l indicates carbon layer.

Figure 3.3. Line mapping of each element identified by energy dispersive spectra (EDS): (a) CBall, (b) CBall@ Fe^{3+} , (c) h- Fe_2O_3 and (d) h- $\text{Fe}_3\text{O}_4\text{@C}$

Figure 3.4. (a) Change of zeta potentials (ζ) of CBall to h- $\text{Fe}_3\text{O}_4\text{@C}$. (b) X-ray diffraction patterns of hollow and non-hollow Fe_2O_3 and $\text{Fe}_3\text{O}_4\text{@C}$. (c) Pore size distribution calculated from N_2 adsorption/desorption isotherms.

Figure 3.5. Electron microscopic images of non-hollow controls: (a) nh- Fe_2O_3 ; (b and c) nh- $\text{Fe}_3\text{O}_4\text{@C}$; and (d) h- $\text{Fe}_3\text{O}_4\text{@C}$ for comparison. (SEM for a, b and d; TEM for c)

Figure 3.6. (a and b) The potential profiles during charge (lithiation) and discharge (delithiation) at the first and second cycle of h- $\text{Fe}_3\text{O}_4\text{@C}$ (a) and nh- $\text{Fe}_3\text{O}_4\text{@C}$ (b). (c) Discharge capacity (Q_{dch}) change as a function of C -rate. (d) Cycle retention at $0.2 C$ and $1 C$.

Figure 3.7. SEM images of electrode composites based on h- $\text{Fe}_3\text{O}_4\text{@C}$ (a to c) and nh- $\text{Fe}_3\text{O}_4\text{@C}$ (d)

and e) for comparison between before (a and d) and after (b and e) one hundred charge/discharge cycles at 0.2C or at 1C (c). The electrode composites consisted of a 70:20:10 mixture of the active material (h-Fe₃O₄@C or nh-Fe₃O₄@C), a conductive agent (Super P) and PAA/CMC (1:1 wt%, polyacrylic acid/carboxymethyl cellulose) as a binder. The scale bar in (a) is applied to other images.

Figure 4.1. SEM and TEM images. (a-c) for p-Co₃O₄ and (d-f) r-Co₃O₄.

Figure 4.2. Illustration of a hierarchical structure in Co₃O₄ nanomaterials. Within p-Co₃O₄ and r-Co₃O₄ nearly identical primary particles are agglomerated to form the secondary structures (100 to 300 nm), which finally construct the macroscopic tertiary architectures.

Figure 4.3. (a) N₂ sorption isotherms and (b) NLDFT pore size distribution curve of p-Co₃O₄ as black one and r-Co₃O₄ as red one.

Figure 4.4. Electrochemical characteristics of p-Co₃O₄ and r-Co₃O₄ in the left and right columns, respectively. (a and b) Potential profiles during lithiation and delithiation at the first and second cycles. (c and d) Capacity retention during the repeated cycles of charge and discharge at 0.1 C for 100 cycles. (e and f) Capacity dependency on discharge rates. Charge rates were fixed at 0.1 C.

Figure 4.5. SEM images of composite electrodes containing (a) p-Co₃O₄ and (b) r-Co₃O₄. The interconnected secondary particles is clearly shown in (b) while the primary particles agglomerates without connectivity between them recognized in (a).

Figure 5.1. Morphological characterization. SEM images of bare graphites (a and b), EG* (c and d) and EG (e and f).

Figure 5.2. Crystallographic characterization. (a) X-ray diffraction patterns. The intensities were normalized by that of the (002) peak of the corresponding material. (b) Comparison of d-spacing values and domain sizes. The values were calculated from the 2θ location and full width at half maximum of the (002) peak by using Bragg's law and Scherrer equation, respectively.

Figure 5.3. C1s photoemission spectra of graphite (a), EG* (b) and EG (c).

Figure 5.4. Characterization of graphitization by Raman spectra. (a) Raw data. Three different bands (G, D and D') were indicated by dashed lines. (b) Comparison of Raman shifts at peaks of the G band.

The same colors of the corresponding samples were used in (a). (c) Comparison between EG* and EG by normalizing intensities by that of the D band.

Figure 5.5. Galvanostatic delithiation at different current rates. (a to c) Potential profiles of the bare graphite (a), EG* (b) and EG (c). (d) C-rate dependency of capacities.

Figure 5.6. Differential capacity (dQ/dV) curves of bare graphite and EG during the 1st lithiation. Integrated areas are directly related to the amounts of SEI layer.

Figure 5.7. XPS depth profiles of C1s spectra of (a) bare graphite, (b) EG* and (c) EG. There were no significant changes of peak at 285 eV with NG. However, the peaks of EG* and EG increased with time.

Figure 5.8. TOF-SIMS depth profiles of (a) bare graphite, (b) EG* and (c) EG.

Figure 5.9. (a) Potential profiles of EG* and EG at the first and second cycles during lithiation at 0.1 C and delithiation at 0.1 C. (b) Capacity retention of EG* and EG along cycles consisting of lithiation at 0.1 C followed by delithiation at 0.1 C. (c) Differential capacity curves of the bare graphite and EG at the second cycle. The red arrows indicate the potential scan directions. Stages were indicated in blue. (d) Differential capacity curves of EG at 0.1 C and 0.5 C. The gaps between blue dotted lines mean the overpotential.

Figure 5.10. Galvanostatic lithiation of EG at different C-rates with a fixed current (0.1C) during delithiation.

Figure 5.11. Electrochemical impedance spectra of the bare graphite (dotted lines) and EG (solid lines) measured in situ during galvanostatic delithiation at 0.1 C.

List of Tables

Table 1.1. Characteristics of electrochemical energy storage systems.

Table 5.1. Compositions of chemical bonds relevant to carbon estimated from C1s photoemission spectra in Figure 5.3.

Chapter 1. Introduction

1.1 Lithium-ion Batteries (LIBs)

1.1.1 Principle of LIBs

In the late of 1970s, researcher at Oxford University discovered that lithium ions can be intercalated into the crystal lattice of cobalt or nickel oxides, resulting in LiCoO_2 or LiNiO_2 .¹ The LIBs contain no metallic lithium and is therefore much safer on recharge than the Li-metal cell.

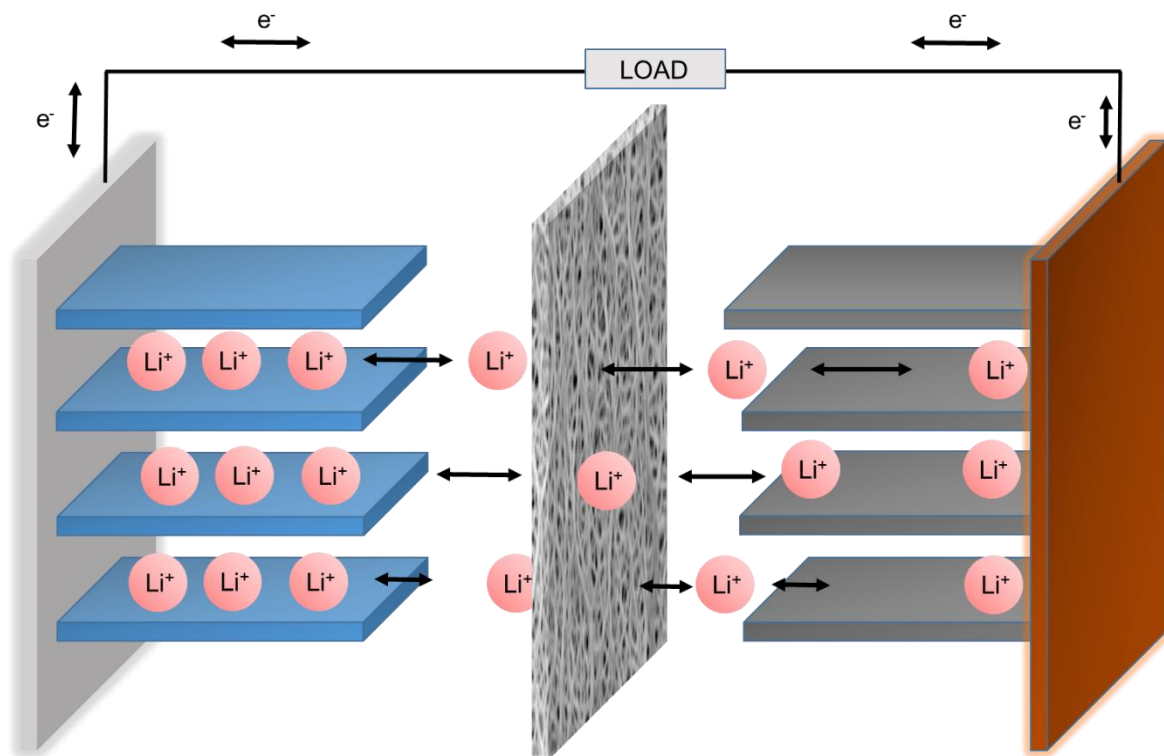


Figure 1.1. Working scheme of conventional lithium-ion batteries (LIBs).

The working principle of LIBs is illustrated in figure 1.1. Lithium ions are extracted from cathode materials on charging, which pass through lithium-ion selective membrane by the aid of electrolyte containing lithium salt to anode while electron move along the external circuit in equal numbers or at an equal rate to balance the charge neutrality. On discharging, the lithium ions and electrons go back to the cathode side, respectively. Hence, LIBs are so called “Rocking chair batteries”. Electrochemical potential difference between cathode and anode materials generates the operating voltage applied to the load.

1.1.2 Characteristics of LIBs

As one of electrochemical energy storage systems, LIBs have spread widely due to attractive advantages compared with other rechargeable electrochemical energy storage systems (Table 1).² Long charge/discharge cycle is available and self-discharge is low, which enable mobile devices to adopt LIBs to satisfy the need of the market. High gravimetric energy density due to the lightness of lithium element and high cell voltage around 3.6 V makes LIBs be used for not only mobile devices but also large energy storage such as UPS and electric vehicles. After being commercialized in 1991 by Sony Corp., the performance of LIBs are getting improved, however, manufacture cost is still high. Most experts agree that manufacturing cost for LIBs would fall in coming years, but nobody knows how far and how quickly. More inexpensive LIBs is capable of widening adoption of electric vehicles.

Table 1.1. Characteristics of electrochemical energy storage systems.

	NiCd	NiMH	Lead Acid	Li-ion	Reusable Alkaline
Gravimetric Energy Density (Wh/kg)	45-80	60-120	30-50	110-160	80 (initial)
Internal Resistance (mΩ)	100-200 6V pack	200-300 6V pack	<100 12V pack	150-250 7.2V pack	200-2000 6V pack
Cycle Life (to 80% of initial capacity)	1500	300-500	200-300	500-1000	50 (to 50%)
Fast Charge Time	1h typical	2-4h	8-16h	2-4h	2-3h
Self-discharge / Month (RT)	20%	30%	5%	10%	0.3%
Cell Voltage (nominal)	1.25V	1.25V	2V	3.6V	1.5V
Load Current - peak - best result	20C 1C	5C 0.5C or lower	5C 0.2C	>2C 1C or lower	0.5C 0.2C or lower
Operating Temperature (discharge only)	-40 to 60°C	-20 to 60°C	-20 to 60°C	-20 to 60°C	0 to 65°C
Typical Battery Cost (US\$, reference only)	\$50 (7.2V)	\$60 (7.2V)	\$25 (6V)	\$100 (7.2V)	\$5 (9V)
Cost per Cycle (US\$)	\$0.04	\$0.12	\$0.10	\$0.14	\$0.10-0.50
Commercial use since	1950	1990	1970	1991	1992

Commercialized LIBs have small power 5- to 10-kW/20 kW and large 1-Mw/15-minute discharge time at rated power. In the past a few years, LIBs technology has emerged for stationary storage applications. Plug-in hybrid electric vehicles (PHEVs) and pure electric vehicles (EVs) which need large capacities of 15 to 20 kWh for PHEVs and up to 50 kWh for EVs.³ To commercialize LIBs as a large-scale energy storage system, higher energy and power density are necessary. Energy density (Wh/kg) is originated from the voltage and capacity. Voltage is determined by the difference in the potentials between cathode and anode, hence cathode material having larger potential versus Li/Li⁺ and anode material having smaller potential versus Li/Li⁺ are favored. It is important to develop much higher capacity materials. Indeed, electrolyte which has larger electrochemical window (~5 V versus Li/Li⁺) should be guaranteed.

1.1.3 Cathode materials

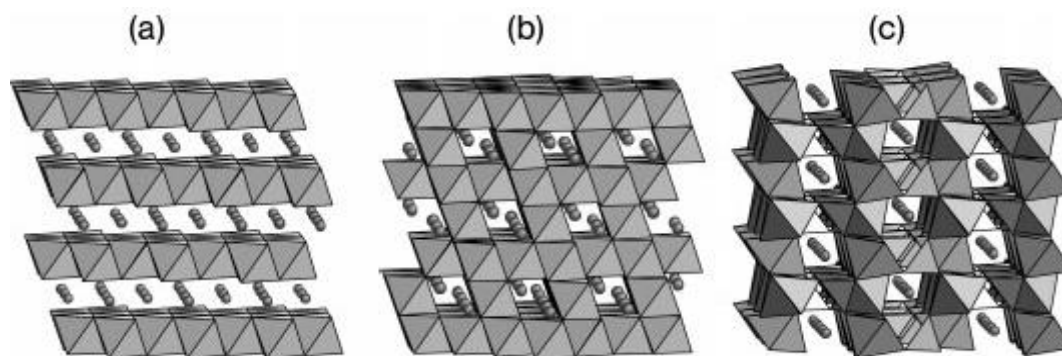


Figure 1.2. The crystal structure of (a) layered structure, (b) spinel structure, and (c) olivine structure.

Cathode materials are categorized by crystal structures (Figure 1.2).⁴ Layered structures were the first candidates.⁵ Covalently bonded slabs are held together while adjacent slabs have relatively weak *van der Waals* forces. Lithium ions can move through the space between layers. LiCoO₂ is a representative layered structure material. It has hexagonal α -NaFeO₂ structure in which Li ions exist between two CoO₂ layers. Although it has high theoretical capacity of 274 mAh g⁻¹, its practical capacities are much lower (130~140 mAh g⁻¹) because phase change occurred when x in Li_xCoO₂ is under 0.5 during charge process, that is to say α -NaFeO₂ structure changes to monoclinically distorted CdCl₂ structures. Many researchers increased charge cut-off voltage to increase reversible capacity by coating metal oxide on the LiCoO₂ surface. Cho's group coated SnO₂ on the LiCoO₂ and could increase charging cut-off voltage up to 4.4 V, resulting in the improved initial capacity (166 mAh g⁻¹) and 87% cyclability after 50 cycles.⁶ The group also conducted Al₂O₃ coating on the LiCoO₂ surface. Al₂O₃ coated LiCoO₂ was charged up to 4.4 V, which showed much higher initial capacity (174 mAh g⁻¹) and 94% cyclability after 70 cycles.⁷

Although there are many advantages, weak point is cost. Cobalt is expensive. In order to reduce the cost, cobalt was replaced with nickel and manganese. However, LiNiO_2 is unstable structure due to the off-stoichiometry drying synthesis and Ni^{2+} destroys a layer structure, hindering Li^+ reintercalation, resulting in decreasing cell performance. Unstable layered structure of LiMnO_2 changes to stable spinel structure. It was impossible to replace all cobalt with nickel or manganese. Partially substitution of Co ions with Ni^{2+} and Mn^{2+} was developed, so called “442” or “333” materials (Ni:Mn:Co ratio). LiNiCoMnO_2 (NCM) and LiNiCoAlO_2 (NCA) became more popular, now most cell makers employed them in current electric vehicles.

Another cathode candidate is spinel-framework structure, LiM_2O_4 ($M = \text{Ti, V, Mn}$). LiMn_2O_4 is the representative material. It has good thermal stability compared to LiCoO_2 and is low cost due to manganese element. Although theoretical capacity is 148 mAh g^{-1} , practical capacity is around 120 mAh g^{-1} . In a regular hexahedron structure Li ions exist in tetrahedral site (8a) and Mn^{3+} or Mn^{4+} ions exist in octahedral site (16d). Li ions can move through not only tetrahedral site (8a) but also empty octahedral site (16c), exhibiting two different working voltages at 4 V and 3 V versus Li/Li^+ , respectively. Tetrahedral site (8a) is energetically stable and need high activation energy to move Li ions. When Mn^{4+} in cubic structure MnO_6 is reduced to Mn^{3+} in tetragonal structure MnO_6 , lattice parameters are rapidly changed, leading to deterioration of cell performance. This is Jahn-Tell distortion effect. Mn^{2+} dissolution formed from Mn^{3+} is also a big problem to solve. That’s why only 4 V region is used. For higher voltage and capacity, manganese ions are substituted for nickel ions.

Phospho-olivine structures materials, LiMPO_4 ($M = \text{Fe, Mn}$), have been emerged due to the structural stability. Strong covalent bonding between P^{5+} and O^{2-} guarantees good stability and good cycle life during lithium insertion and extraction. Low cost of Fe and Mn is also attractive point. LiFePO_4 was emerged in advance. It exhibits almost capacity near to theoretical capacity of 170 mAh g^{-1} . Despite of excellent thermodynamics, relatively low working voltage (3.45 V vs Li/Li^+) and very low intrinsic ionic and electrical conductivities are limitations in the viewpoint of kinetics. LiMnPO_4 showing higher working voltage around 4.1 V and low cost have got spotlights as an alternative olivine cathode material. Due to the intrinsic properties of Mn, ionic and electrical conductivities are much lower than LiFePO_4 . Low conductivities were overcome somewhat by coating carbonaceous and other conductive materials on the surface of LiMPO_4 and creating ion-conducting surface phase through controlled off-stoichiometry.^{8,9}

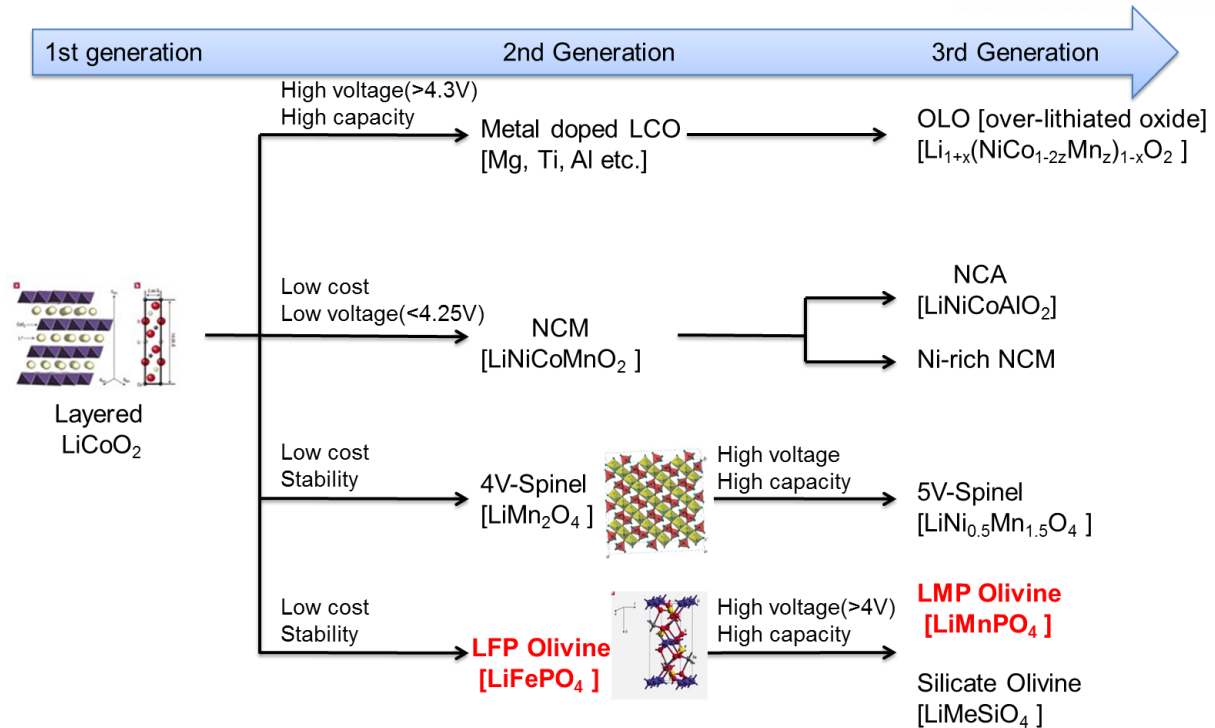


Figure 1.3. Various cathode materials according to the order in development.

1.1.4 Anode materials

Lithium metal has been considered as an anode material due to high energy density, high voltage, and high energy density. Despite of many electrochemical properties, researches of lithium metal as an anode were abandoned due to the dendritic formation of lithium during charge process which causes poor cyclability and dangerous safety problem. To replace the lithium metal anode, various materials which react with lithium ions were discovered and suggested.

The kinds of anode materials can be divided by reaction mechanism with lithium ions. These are intercalation compounds, conversion reaction compounds, and alloying reaction compounds.

Graphite is a representative intercalation compound. Carbon was satisfied as an anode material due to low cost and the lowest reduction potential which is close to the reduction potential of Li/Li^+ . Graphite has a layered structure and lithium ions can be intercalated into the graphite layers. Due to insertion between empty graphitic layers, there are no structural deformation, but distance between layers is slightly enlarged. It guarantees long cycle life and fast kinetics. Since the development of graphite anode, there is no a powerful rival up to now. Current LIBs in the commercialization use only graphite anode while several different cathode materials are used.

$\text{Li}_4\text{Ti}_5\text{O}_{12}$ (LTO) is another intercalation compounds. LTO compounds react with lithium ions at 1.55 V vs. Li/Li^+ . SEI layer is not formed because the organic electrolytes are decomposed under 1 V vs. Li/Li^+ , enabling high coulombic efficiency. There is no concern about the lithium dendrite formation.

In addition, zero strain in LTO during Li ions insertion guarantees excellent cyclability. However, its low theoretical capacity of 175 mAh g⁻¹ and poor lithium ion diffusion (10^{-14} to 10^{-17} cm² s⁻¹) and poor electrical conductivity ($<10^{-13}$ S cm⁻¹) are the weak points compared to other anode candidates.^{10, 11}

Conversion reaction based compounds are described in form of MX (M; transition metal, X; anion). Metal oxides are the representative conversion reaction compounds. These materials usually have three times larger capacities than commercialized natural graphites. There is large hysteresis between potential profile during charge and discharge process, which can be main problem for applications demanding high voltage. Large volume expansion around 100% causes pulverization of active materials and electrical isolation, leading to poor cyclability. Conversion reaction compounds are far away from the commercialization.

In recent years, silicon and germanium based on alloying reaction with lithium ions have been considered as alternative anode materials due to their high capacities. Si has >3500 mAh g⁻¹ at room temperature, close to the capacity of lithium metal and Ge has 1384 mAh g⁻¹. Since the atoms of metals are closely arranged to adjacent atoms, a huge volume expansion occurs when metals react with lithium ions making metal-Li alloys. Si and Ge are expanded up to 280% and 250%, respectively, resulting in short cycle life and low stabilities.

1.2 Strategies to Improve the Kinetics of LIBs

It is important to improve the electrochemical performance to apply LIBs for various applications. High power density with fast kinetics of LIBs is a requisite factor for the commercialization of electric vehicles which is one of the highly marketable product.

Before I discuss how to improve the performance of LIBs, it is necessary to review what factors influence on the performance. In the view point of kinetics, charge-transfer rates and ionic/electronic transport are dominant factors which influence on kinetics. The former is intrinsic properties of active materials. The latter, which I have focused, are ionic transport, Li solid-state diffusion, and electron transport. The first factor, ionic path, depends on the thickness and porosity of separator, ionic conductivity of electrolyte, pore structure of electrode, surface area of active materials, and composition and thickness of SEI layer. The second, Li solid-state diffusion, is determined by particle size and diffusion coefficient of active materials. The characteristic diffusion time is proportional to the square of diffusion length and inversely proportional to diffusion coefficient ($t \sim L^2/D$).¹² That is, nanostructured electroactive materials with short diffusion length is preferred. The last, electron path, is predestined from electronic conductivity of active materials, conduction aid such as carbon black, porosity of electrode, and other parts such as lead, tab, welding, etc.. For LIBs to work, all factors should be optimized as a saw-toothed wheel mesh smoothly.

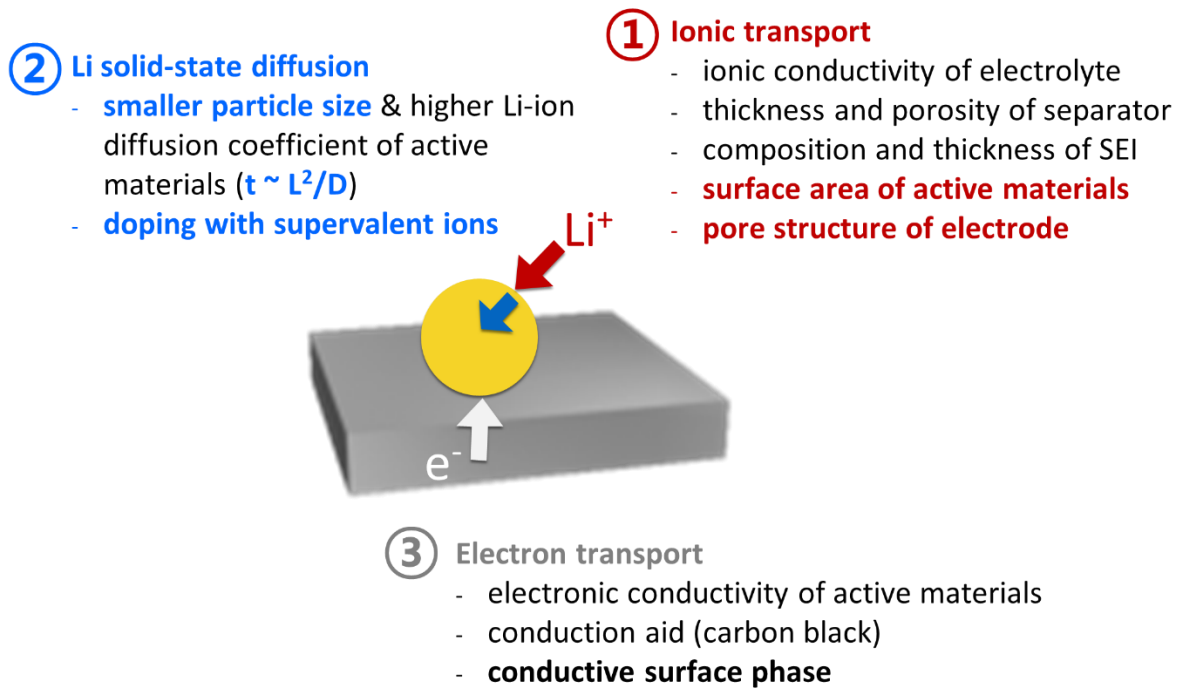


Figure 1.4. The factors to influence on kinetics in the viewpoint of ionic and electron transports.

1.2.1 Ionic transport

Porous electrodes enhance ionic transport across the interface between electrode and electrolyte.¹³ The term of pore is defined as voids between particles and integral part of a solid framework. The voids are created by casting and drying process. Integral porosity is independent of particle size, which depends on synthesis conditions and methods. Pore structures have several advantages for LIBs. Pores offer large good access of the electrolyte to the electrode surface. Much larger surface area in a pore electrode help charge transfer to facilitate because large contact area reduce specific current density, resulting in less electrode polarization and easier charge transfer at the interface.

Soft-template method using surfactants and solvent is easy to control porous materials. Cationic surfactants such as alkyltrimethylammonium and anionic sulfate or sulfonic surfactants were used as soft-templates to synthesize porous TiO_2 electrode.^{14, 15} In case of that temperature of crystallization of active material is higher than that of decomposition of surfactants, that is, high temperature is necessary to obtain well-ordered crystalline, hard-template method can be an alternative. Infiltration of precursor into hard-template such as silica or carbon structure and heat treatment are common way to prepare mesoporous electrodes. Cathode materials such as LiFePO_4 and LiMn_2O_4 as well as anode materials such as Co_3O_4 and SnO_2 were synthesized by using silica known as KIT-6 or SBA-15.¹⁶⁻¹⁹

1.2.2 Li solid-state diffusion

The rate of charge delivery is determined by Li solid-state diffusion step through the solid particles in which a battery stores charge. By shortening the diffusion length, lithium solid-state diffusion can be faster. He et al. compared the different size of antimony nanocrystals (Sb NCs) and microcrystal as anode materials for lithium ion batteries and sodium ion batteries.²⁰ Both 10 nm and 20 nm Sb NCs showed excellent rate capabilities as compared with bulk Sb. The gap of capacities among them were getting large as current densities increased. The size effect was more clearly observed in sodium ion batteries due to the larger size of sodium ion than that of lithium ions. In addition to zero-dimensional spherical nanoparticles, one-dimensional nanowires and nanorods were also favorable for a high power rechargeable lithium batteries.^{16, 21-23}

However, smaller nanoparticle is not always excellent as electroactive materials. Kim et al. prepared different size of Si particles by using reverse micelles at high temperature and pressure and showed that the electrochemical performance of 10 nm sized Si particles were better than that of 5 nm sized and 20 nm sized Si particles.²⁴ Son et al. synthesized different sizes of the GeO₂ particles from 2 nm to 35 nm, among which the 6 nm sized GeO₂ showed the best performance because the quantum confinement effect and agglomeration of nanoparticles made the 2 nm sized GeO₂ worse than 6 nm sized particles.²⁵

Doping is another approach to enhance the diffusion rate. Zinc-doped LiFePO₄ showed boosted diffusion coefficient due to that doped zinc atoms act as a kind of pillar which enlarge the lattice volume give larger space for the movement of lithium ions, not destroying the lattice structure of LiFePO₄.²⁶ Veluchamy et al. synthesized boron-substituted at 16d site of the cubic spinel structure which have higher diffusion coefficient of lithium.²⁷

1.2.3 Electron transport

Intrinsic electronic conductivity of cathode materials can be enhanced by doping it with supervalent cations because most cathode materials are semiconductor defined by their band gaps (0.3 to 2.7 eV). Incorporation of Mg in LiCoO₂ enhanced conductivity^{28, 29} and Shi et al. discovered that Mg-doping increased Co⁴⁺ concentration which shift the Fermi level into the valence band. Co 3d orbital is overlapped with the O 2p electrons, resulting in the enhanced electron transport.³⁰ Chung et al. synthesized doped LiFePO₄ with the metals supervalent to Li⁺.³¹ The conductivity of doped LiFePO₄ was superior to that of other cathode such as LiCoO₂ and LiMn₂O₄ in their lithiated/delithiated states at room temperature.

Conductive agent including Super P, Ketjen black, and acetylene black commonly used are also an important factor for electron transport. Cheon et al. mixed Lonza-KS6 (6 um) and Super P (30 nm) as

a binary conductive agent in a LiCoO_2 cathode.³² Although ionic diffusion rate decreased, charge transfer resistance decreased, resulting in the improvement of kinetics. Spahr et al. studied the newly developed conductive carbon C-ENERGY Super C65 and C45.³³ Both carbon enhance the electrical conductivity. Especially, Super C45 can be used even at dry-mixing due to the lower viscosity and facile dispersibility. Guoping et al. studied the effect of different kinds of nano-carbon conductive additives on the resistance and electrochemical behavior.³⁴ Compared to acetylene black and carbon fibers, carbon nanotubes were the best due to Their higher crystalline and particle size in nanoscale enhanced rapid electron transport and lower percolation threshold.

Carbon coating is the commonly used method to enhance the electrical conductivity by providing pathways for electron transport due to the dispersed carbon networks. Oh et al. exhibited discharge capacities of micrometer-size LiFePO_4 spheres by coating homogeneous double carbon coating layer.³⁵ In situ carbon coating is preferred due to the complete coating primary particles with conductive carbon and abridgment of post carbonization process. Wang et al. used aniline as a carbon source and prepared polyaniline coated FePO_4 by means of catalytic effect of Fe^{3+} ions.⁸ Through the heat treatment, uniformly carbon-coated LiFePO_4 were obtained. Many researchers wrapped electroactive materials with graphene or graphene oxides which have high electrical conductivities. N-doped graphene- SnO_2 sandwich papers exhibited enhanced rate capability as well as large capacity.³⁶

1.3 Research Scope

I have designed ionic pathways of electroactive materials to improve the lithium ions transport and diffusion (Figure 1.5). By fabricating active materials in nanoscale, surface area on which active materials reacts with lithium ions increase and ionic and electronic transport length are shortened, resulting in enhancing the kinetics. This strategy was applied to lithium manganese phosphate, iron oxide, and cobalt oxide. Smaller nanoparticles of LiMnPO_4 (LMP) were synthesized by sequential precipitation method instead of co-precipitation. Hollow sphere iron oxides were designed not only to increase Li ion active sites exposed to the electrolyte but also to provide buffer space for volume expansion. Two different morphologies (plate and rod shapes) of hierarchical architecture of Co_3O_4 composed of 10 nm primary particles were synthesized by conversion of metal-organic frameworks (MOFs) and their electrochemical properties were comparatively investigated.

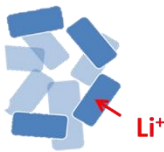
On the other hand, the resistance of lithium ions diffusion within active materials can be controlled by adjusting lattice parameters in unit cell such as lattice constant. This idea was applied to graphite anode material. Lithium ion diffusion was enhanced between graphitic layers by expanding d-spacing largely. In addition, the hydrogen-containing bonds in functional groups at edge sides partially induced negativity of carbons in graphite, leading to the reduction of the energy barrier of lithium ion

intercalation.

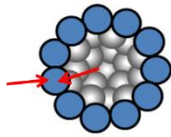
By designing ionic pathways of electroactive materials, overall kinetics was enhanced, resulting in a much better improved electrochemical storage system.

Morphology Control of Particles i) to increase active sites (surface area) with Li-ions
 ii) to shorten ionic/electronic transport length

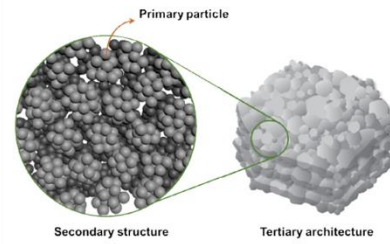
1 primary nanoparticles
 ($t \sim L^2/D$)



2 hollow sphere nanostructure



3 a hierarchical structure with nanoparticles in microscale



Modifying Intrinsic Parameter of Crystalline

4 Widening Li-ion diffusion channel

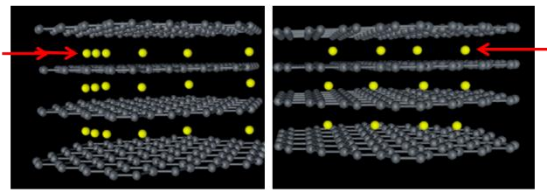


Figure 1.5. Two strategies and four applications to enhance the kinetics of lithium-ion batteries in this thesis.

Chapter 2. Restricted growth of LiMnPO_4 nanoparticles evolved from a precursor seed

2.1 Introduction

Phospho-olivines (LiMPO_4 where $M = \text{Fe, Mn, Co, Ni}$) have been considered as one of the most potential cathode materials for LIBs, based on a well-defined two phase reaction coupled with one equivalent electron: $\text{LiMPO}_4 \leftrightarrow \text{Li}^+ + \text{MPO}_4 + \text{e}^-$.³⁷⁻⁴⁶ The strongest reason for interests in the materials is their relative high theoretical capacity ($\sim 170 \text{ mAh g}^{-1}$) compared with that of more traditional cathode materials such as LiCoO_2 layered structure (140 mAh g^{-1} within a structurally stable range⁴⁷) and LiMn_2O_4 spinel (148 mAh g^{-1}).⁴⁸ However, the higher capacity of LiMPO_4 does not always lead to higher energy density because energy density results from the product of its working potential as well as its capacity. LiFePO_4 , the most representative member of the phospho-olivine family, shows its energy density at 585 Wh kg^{-1} that is the value lower than that of LiMn_2O_4 spinel (607 Wh kg^{-1}). The main cause of the inferior energy density of LiFePO_4 is its low working potential at 3.45 versus $\sim 4.1 \text{ V}$ for LiMn_2O_4). By changing the transition metal constituent of LiMPO_4 from Fe to Mn, Co or Ni, its working potential is controlled to be higher values: 4.1 V for $M=\text{Mn}$ in LiMPO_4 ,⁴⁹ 4.8 V for Co,⁵⁰ and 5.2 V for Ni.⁵¹

In the case of $M = \text{Fe}$ in phospho-olivines, we demonstrated that a sequential precipitation in which two different intermediate precipitates (Li_3PO_4 and $\text{M}_3(\text{PO}_4)_2$) are formed not simultaneously but consecutively leads to a hollow secondary structure consisting of carbon-coated primary particles.⁵² The resultant structure was helpful to overcome demerits of LiFePO_4 such as low electronic and ionic conductivities: ($k_e = 10^{-9}$ to $10^{-8} \text{ S cm}^{-1}$ and $D_i = 10^{-8}$ to $10^{-8} \text{ cm}^2 \text{ s}^{-1}$, respectively).⁴⁸ In the other members of the phospho-olivine family, the demerits become even more serious with slower electronic transport (k_e) even if higher energy density is thermodynamically achievable: $k_e = 10^{-11}$ to 10^{-8} , 10^{-11} to 10^{-9} and 10^{-14} to $10^{-11} \text{ S cm}^{-1}$ while $D_i = 10^{-9}$ to 10^{-7} , 10^{-9} to 10^{-5} and $10^{-5} \text{ cm}^2 \text{ s}^{-1}$ for $M = \text{Mn, Co}$ and Ni in order.^{46, 53, 54} Therefore, the sequential precipitation method with some modification was applied to LiMnPO_4 system in this work to get the same advantages (Figure 2.1).

2.2 Experiments

2.2.1 Preparation

Olivine LiMnPO_4 was synthesized by precipitating $\text{Mn}_3(\text{PO}_4)_2$ on thermally hardened Li_3PO_4 seeds (Figure 2.1). The Li_3PO_4 seeds were precipitated by introducing 10 mmol H_3PO_4 to a solution prepared by dissolving 30 mmol LiOH in 12 ml water. The seeds were filtered and then thermally hardened at $300 \text{ }^\circ\text{C}$ for 3 h. The thermally hardened seeds were re-dispersed in 12 ml water and 10 mmol MnSO_4

was added to the re-dispersed solution. The dried mixture of Li_3PO_4 and $\text{Mn}_3(\text{PO}_4)_2$ was calcined at 600 °C for 10 h in an inert atmosphere. For coating the resultant LMP, sucrose was mixed with LMP in water at 50 wt% of the active materials followed by drying and heating at 600 °C for 6 h. As a control, LMP was prepared by co-precipitation. The same amounts of precursors were used as those of our surface-confined method described above.

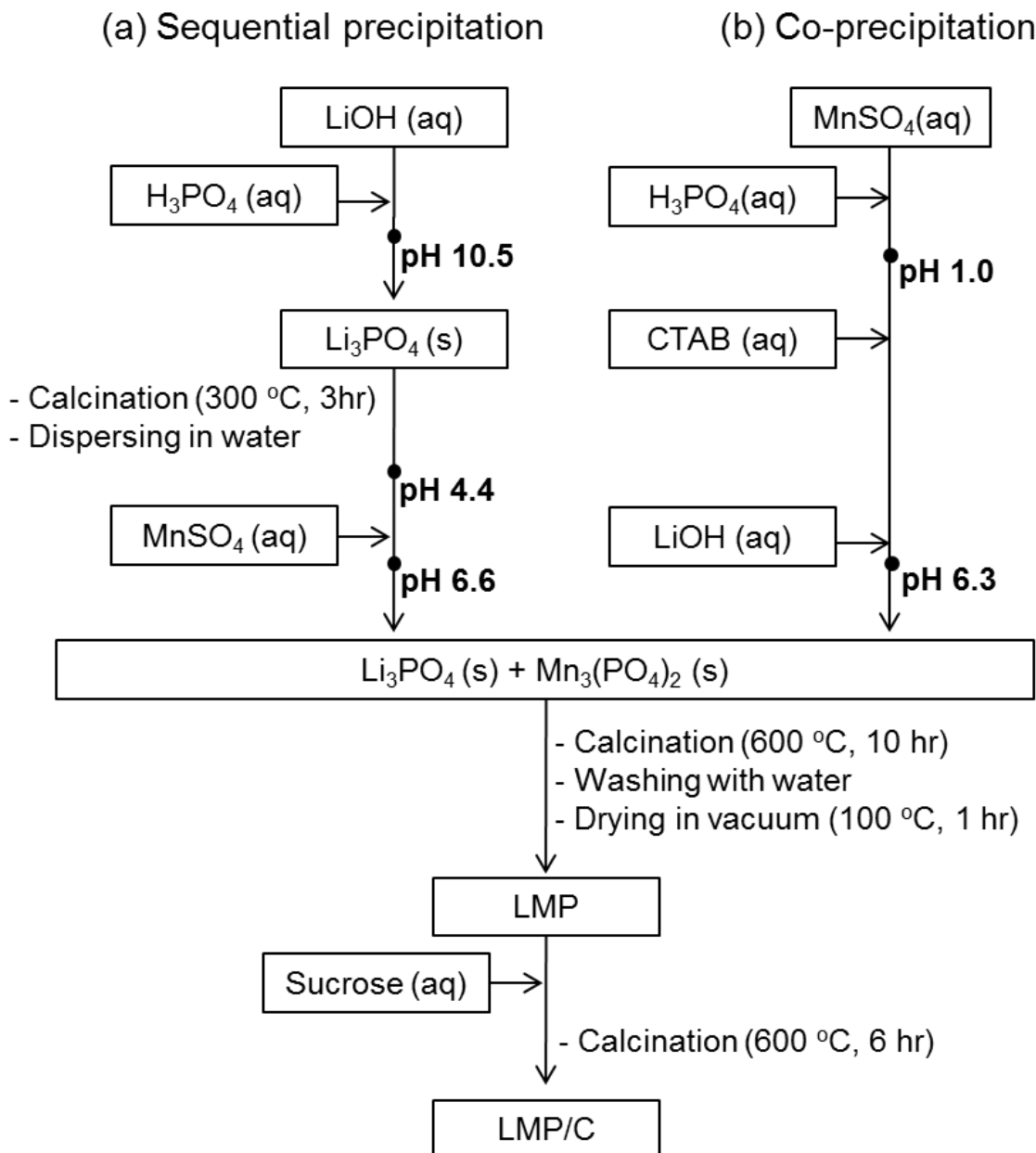


Figure 2.1. Synthesis of LMP via two different strategies for precipitation: (a) surface-confined precipitation and (b) co-precipitation.

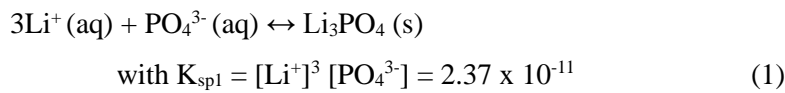
2.2.2 Cell construction

The 2016R-type coin half cell configuration was used with 1.15 M LiPF₆ in 3:7 (v/v) ethylene carbonate/dimethyl carbonate (EC/DMC) as electrolyte for charge and discharge tests. Lithium foil was used as anode. Cathode was constructed by mixing active materials, polyvinylidene fluoride (PVdF) as a binder and Super P carbon black as a conduction enhancer at a weight ratio of 7:1:2 in N-methyl-2-pyrrolidone as a solvent. The mixed slurry was cast onto Al foil by a doctor blade coater; heated at 110 °C for 1 h to evaporate its solvent; and then pressed by using a roll press. The resultant electrodes are specified by densities of the active materials: areal density (d_a) = 2.54 mg cm⁻²; volumetric density (d_v) = 0.63 g cm⁻³; thickness = 40 μm.

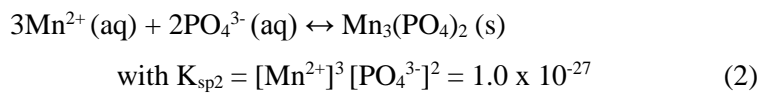
2.3 Results and discussion

2.3.1 Preparation

In the first precipitation step, the first intermediate precipitate Li₃PO₄ is formed with a solubility product K_{sp1} :⁵⁵



Filtered Li₃PO₄ precipitates were sintered at 300 °C for 3 h for thermal hardening and then re-dispersed in water. Formation of the second precipitate Mn₃(PO₄)₂ is followed with the lower value of solubility product K_{sp2} :⁵⁶



PO₄³⁻ is supplied only by re-solubilization process of pre-formed Li₃PO₄ particles to keep its equilibrium at K_{sp1} so that the formation of Mn₃(PO₄)₂ is localized specifically on surface of the Li₃PO₄ particles.

Morphology of precipitates was traced step-by-step by electron microscopes (Figure 2.2). The first precipitate Li₃PO₄ was shaped as a hollow sphere (diameter = ~ 300 nm) by the re-solubilization-precipitation cycles between Li₂HPO₄ and Li₃PO₄ (Figure 2.2a-c).⁵² The ~70 nm-thick shell of the hollow spheres consists of primary particles of ~10 nm diameter. The solid sphere in Figure 2.2a represents a primary particle of Li₃PO₄ without the exact consideration of dimension: wall of the hollow sphere consists of multiple layers of the primary particles. Precipitation of Mn₃(PO₄)₂ on surface of each primary particle of Li₃PO₄ leads to grouping the particles into a fragmented unit, disassembling the hollow secondary structure (Figure 2.2d-f). A trace of hollow spheres still observed in insets of Figure 2.2e and f confirms that the nanoparticles originate from wall of the hollow structure. During calcination at 600 °C for 6 h, each fragment of mixed precipitates (Li₃PO₄ + Mn₃(PO₄)₂) turns into a single LMP particle (Figure 2.2g-i). The size-restriction effect of the surface-confined precipitation can be clearly

emphasized when the electron-micrographic images are compared between our method and co-precipitation (Figure 2.2j and k): 70 nm × 150 nm to 100 nm × 300 nm for our surface-confined precipitation versus 180 nm × 340 nm to 330 nm × 480 nm for co-precipitation.

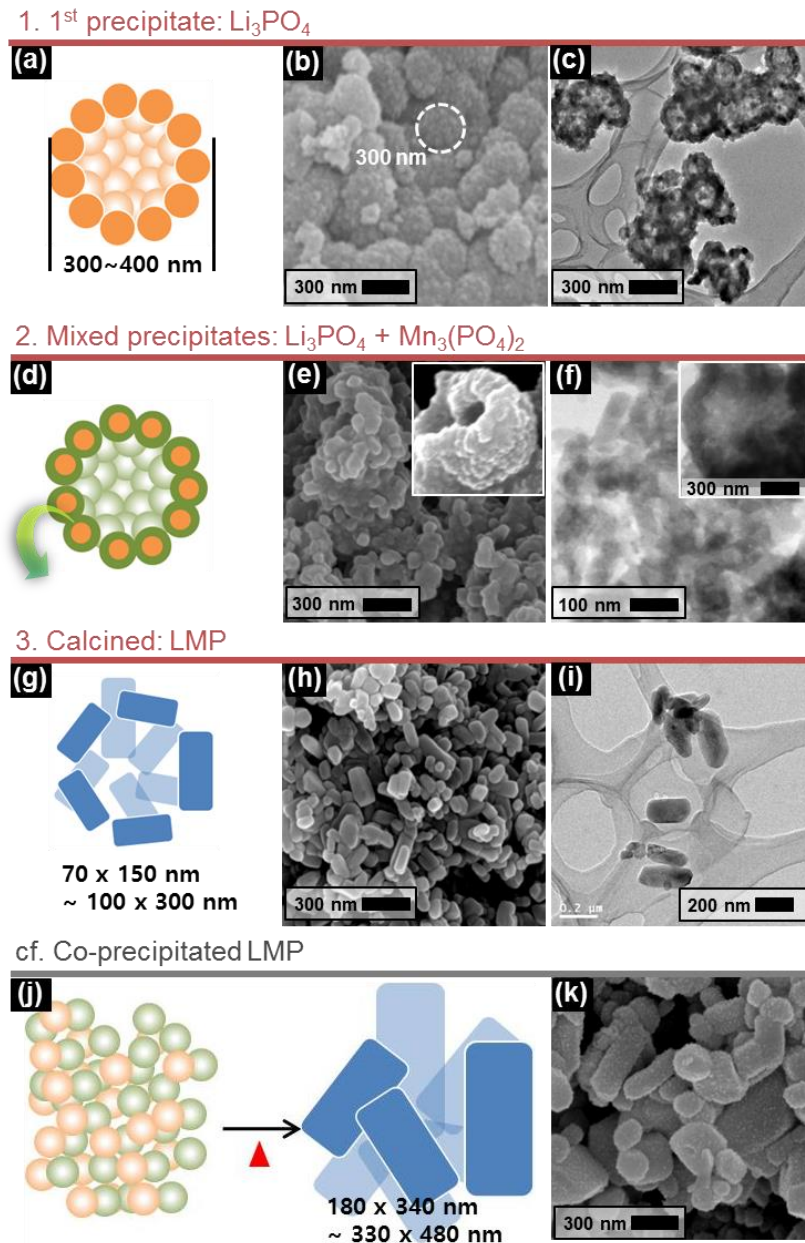


Figure 2.2. (a-i) Schematic illustrations and electron microscopy images of LMP particles from each step of the surface-confined precipitation: (a-c) the first precipitates (Li_3PO_4) (d-f) the mixture of the first (orange) and the second (green) particles obtained after the second precipitation; (g-i) the sample obtained after calcination. (j-k) Schematic illustrations and electron microscopy images of co-precipitated LMP as a control for comparison.

When compared with $M = \text{Fe}$ in LiMPO_4 ($K_{\text{sp}} = 1.0 \times 10^{-36}$), the hollow secondary structure of Li_3PO_4 was not maintained in the case of $M = \text{Mn}$. The structural difference is believed to come from the difference of K_{sp} . As presumed from its higher value of K_{sp} , $\text{Mn}_3(\text{PO}_4)_2$ is more difficult to precipitate or requires more amount of free PO_4^{3-} in aqueous phase for precipitation. Therefore, more amount of Li_3PO_4 is required to be dissolved for initiating the second precipitation when Mn^{2+} ion is introduced to the suspension of Li_3PO_4 made via the first precipitation step. More abundant loss of mass before the second precipitation leads to weakening a structural prop of the hollow secondary structure.

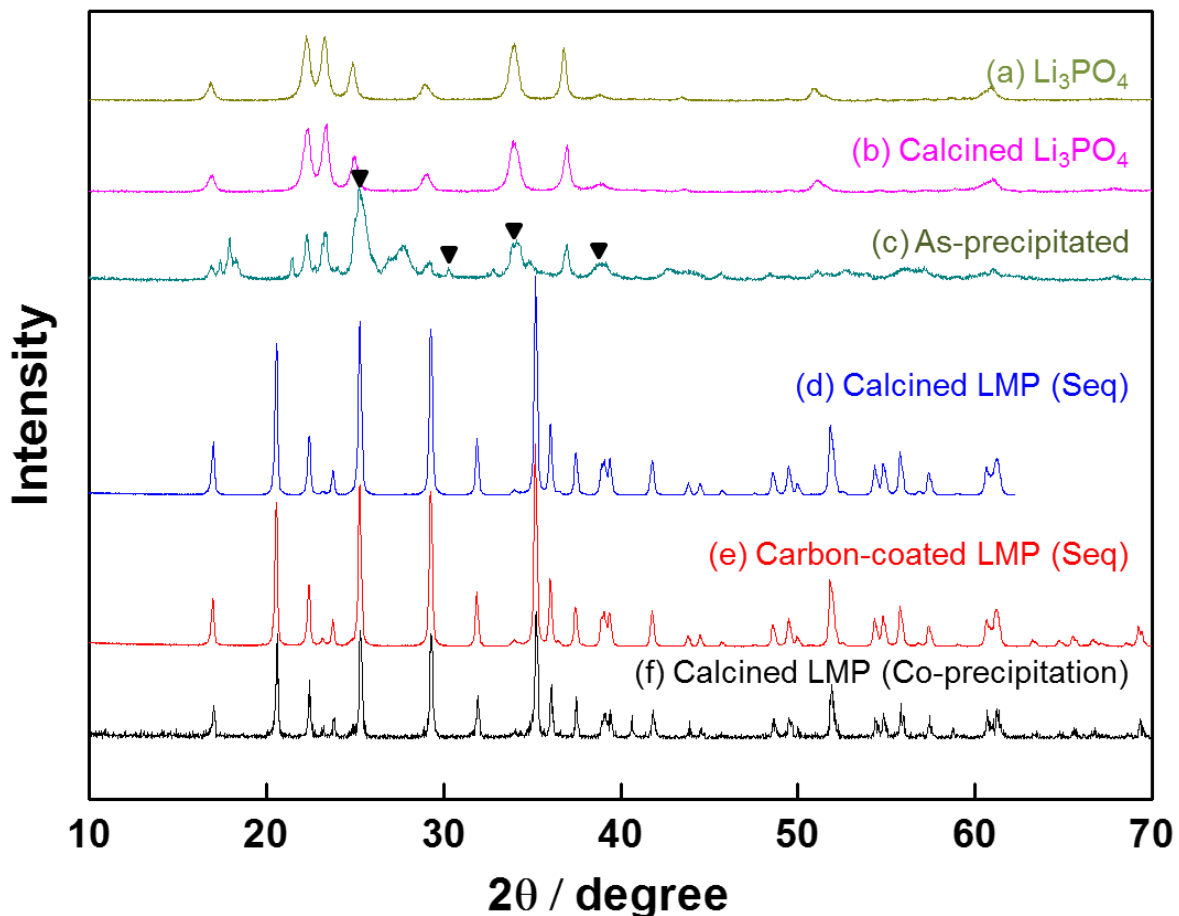


Figure 2.3. X-ray diffraction patterns of the first intermediate precipitate (Li_3PO_4 , a and b), the mixed intermediate precipitate ($\text{Li}_3\text{PO}_4 + \text{Mn}_3(\text{PO}_4)_2$, c), the thermally treated one (LiMnPO_4 , d) and carbon-coated one (LiMnPO_4 , e) obtained through each step of the surface-confined precipitation. For a comparison, the co-precipitated LMP is shown (f).

The crystallographic structure by X-ray diffraction (XRD) and the chemical composition by inductively coupled plasma atomic emission spectroscopy (ICP-AES) proved the successful synthesis of LMP olivine, however, with Li_3PO_4 as a minor impurity phase (Figure 3). The molar composition of

LMP was estimated at Li:Mn:P = 1.2:0.96:1.0 by ICP-AES. From the stoichiometric calculation with an assumption of the mixture consisting of $\text{LiMnPO}_4 + x \text{Li}_3\text{PO}_4$, ~6.5 molar%, equivalent to ~5 wt% Li_3PO_4 , was detected. The minor phase can be easily removed by weak acid such as diluted acetic or phosphoric acid. The products from each step of the surface-confined precipitation were also identified by XRD. There was no difference between before and after thermal hardening process, XRD showing well-defined crystalline Li_3PO_4 . After the second precipitation, unknown peaks that would be assigned to the second precipitate Mn_3PO_4 appeared in addition to the spectra of previous step.

Due to its low electronic conductivity, surface-coating with a conductive material is required for LMP like the case of its sister compound LiFePO_4 . Carbon as a conductive material is well known to play a crucial role for enhancing performances of cathode materials for LIBs. Higher carbon contents in a coating and/or an electrode composite are expected to result in less loss of energy by facilitating electron flow between current collectors and active materials. Even if cell capacity is roughly proportional to carbon contents, the details of carbons would be more important: graphitic degree, percolation extent, ratio between coating and bulk and so on. An in situ carbon-coating where a carbon precursor is assembled into a composite with active material during synthesis (here, precipitation) was tried but failed. The same technique was used in our previous work for LiFePO_4 with CTAB (cetyltrimethylammonium bromide) as a carbon precursor.⁵² In this work, good quality of carbon coating (2 to 4 wt%) wrapping primary particles was successfully obtained even if CTAB is completely decomposed to a zero mass at <300 °C much lower than calcination temperature of the LiFePO_4 (endothermic peak at 260 °C under an inert atmosphere in thermogravimetric analysis (TGA), preliminary data). On the contrary, there was very little (0.04 to 0.08 wt% within error range of analysis) or no carbon contents remaining for LMP with CTAB as a carbon precursor after calcination. We believe that this difference of degree of CTAB carbonization comes from the difference of metals (M in LiMPO_4). When considering that Fe, Ni, Cr, Al and Cu are generally recognized as catalysts for carbonization,^{57, 58} not Mn but Fe is considered to make some helpful catalytic effects on carbonization. This interpretation can be supported by the fact that a considerable amount of carbon (~1.5 wt%) was obtained with $\text{Li Mn}_{0.5}\text{Fe}_{0.5}\text{PO}_4$ from CTAB in our preliminary experiments.

Instead of the in situ carbon coating, therefore, LMP was coated with carbon in a widely used post-synthetic way of sucrose coating followed by calcination. Nanoparticles were successfully coated homogeneously with 8.5 wt% carbon (assayed by a combustion method), which is clearly shown by TEM and a line mapping of carbon element (Figure 2.4a and b). By carbon coating, in Raman spectra, phosphate-related peak at 950 cm^{-1} turned unclear with two high-intensity peaks assigned to carbon's D and G bands at 1345 cm^{-1} and 1590 cm^{-1} (Figure 2.4c). No significant crystallographic difference was observed between bare and carbon-coated LMP (Figures 2.3 and 2.4d). The Rietveld-refined lattice

parameters based on the orthorhombic Pmnb matched closely to the values from a crystallographic database (JCPDS No. 33-0804): bare and carbon-coated LMPs versus database, a (\AA) = 6.1030 and 6.0988 versus 6.1000; b (\AA) = 10.4406 and 10.4385 versus 10.4600; c (\AA) = 4.7462 and 4.7415 versus 4.7440.

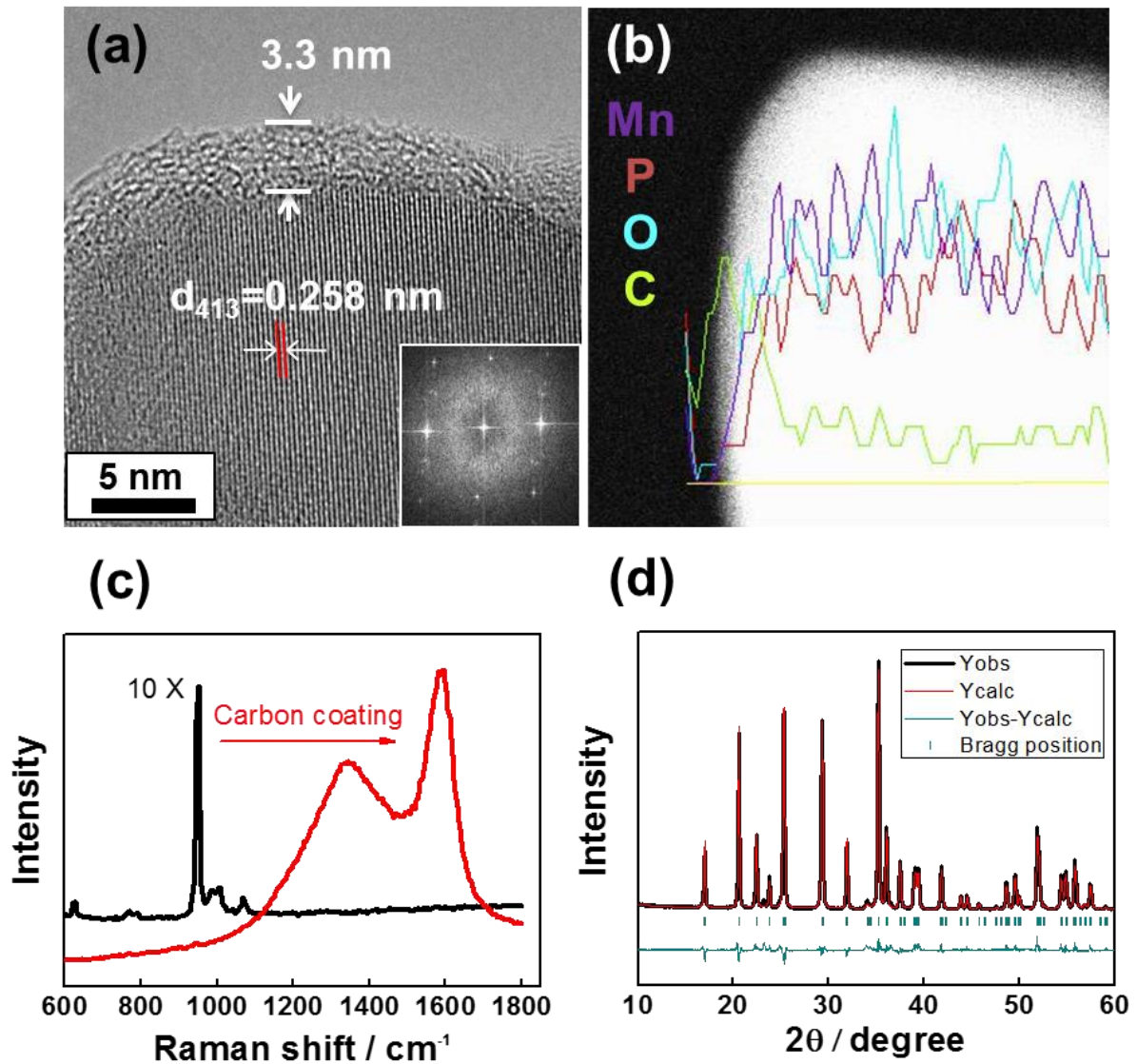


Figure 2.4. (a) A representative transmission-electron-microscopic (TEM) image of a single carbon-coated LMP particle with its Fourier-transformed pattern as an inset. (b) A line mapping of the constituents of a single carbon-coated LMP particle in the same scale of (a). (c) Raman spectra of bare LMP (black, intensity-magnified by 10x) and carbon-coated LMP (red). (d) X-ray diffraction (XRD) pattern of carbon-coated LMP. There was no significant difference between bare and carbon-coated LMPs in terms of the XRD pattern.

2.3.2 Electrochemical performances

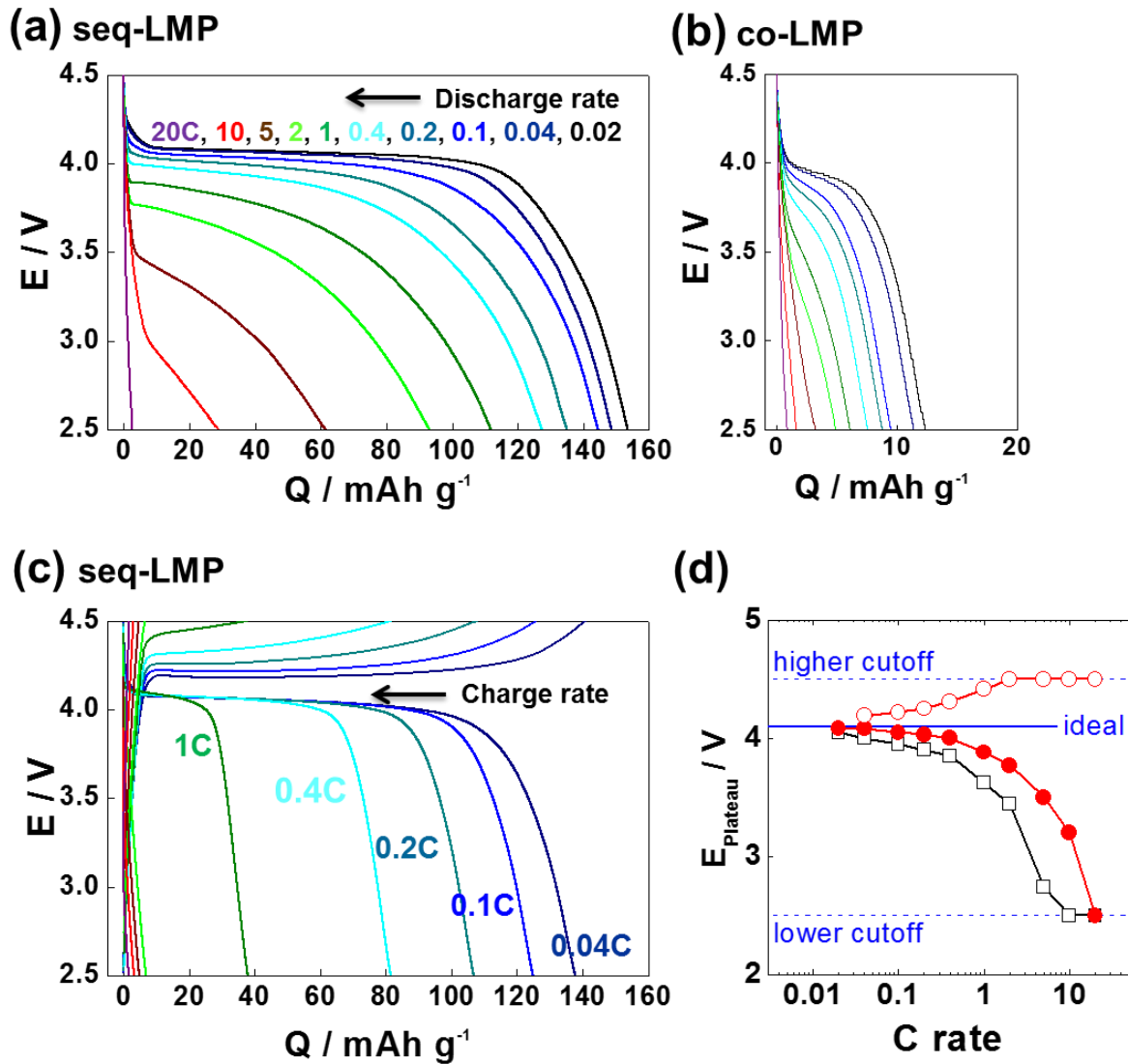


Figure 2.5. (a-c) Potential profiles of half coin cells of sequentially precipitated LMP (seq-LMP, a and c) and co-precipitated LMP (co-LMP, b). 1C = 150 mAh g⁻¹. The cells in a and b were charged at 0.04 C up to 4.5 V followed by keeping the potential until current flowed below a hundredth of the charging current. Then they were discharged at various C rates as indicated. The cells in c were charged at various C rates of constant current as indicated (not followed by keeping them at constant voltage). Then they were discharged at 0.04 C immediately after being charged. (d) C-rate dependency of plateau potential (E_{plateau}) during discharge or charge. Red solid circle, seq-LMP during discharge; red open circle, seq-LMP during charge; black open square, co-LMP during discharge.

The LMP prepared by the surface-confined precipitation (seq- LMP) was tested as a cathode material

for LIBs. In spite of its poor conductivities, the LMP showed good discharge performance from 153 mAh g⁻¹ at 0.02 C to 62 mAh g⁻¹ at 5 C (Figure 2.5a). However, it was difficult at >10 C to find a flat potential behavior based on faradaic reaction of LMP because operational current exceeds the kinetics of lithiation of MnPO₄ during discharge process. When compared with co-precipitated LMP (co-LMP, Figure 2.5b), the improvement of discharge capacities of seq-LMP would be emphasized. The distinguishingly superior capacities of seq-LMP over co-LMP are ascribed to its smaller particle size: $d_{seq} = \sim 1/3d_{co}$ (70 to 100 nm for seq-LMP versus 180 to 330 nm for co-LMP) where d = a characteristic dimension of LMP particles. The particle size affects primarily ionic conductance (as an extensive property, not conductivity) and also indirectly electronic conductance. With the same amount of carbon for coating, smaller particles lead to higher degree of percolation of conductive network. The conductance of seq-LMP-based electrodes would be about ten ($\approx 3^2$) times as high as that of co-LMP electrodes if the following assumption is applicable: electric conductance from current collector to a LMP particle \propto connectivity of the LMP particle to a conductive phase \propto surface area of the LMP particle. In addition to discharge capacity, deviation of plateau potential ($E_{plateau}$) from ideal value (4.1 V) in voltage profiles is a measure of goodness of charge transport. The gap of $E_{plateau}$ between seq-LMP and co-LMP widens as the discharge rate increases, proving better properties of seq-LMP (Figure 2.5d).

In addition to discharge properties, charge characteristics were also investigated (Figure 2.5c). Even if high working potential of LMP (versus LiFePO₄) provides an advantage in terms of energy density for discharge, the narrower potential margin from the working potential (ideally 4.1 V) to the cut-off potential (4.5 V) leads to a demerit of incomplete charge at fast rates (without keeping voltage at the cut-off potential). The asymmetric potential margin is the main reason why charge capacity is much less than discharge capacity even at the same rate even if asymmetric kinetics of LMP might be partly responsible: for example, 128 mAh g⁻¹ for discharge versus 82 mAh g⁻¹ for charge at 0.4 C.

2.4 Conclusion

In this work, we proposed the method to restrict the growth of particle size of LMP during precipitation (called surface-confined precipitation from the viewpoint of synthetic mechanism or sequential precipitation from the viewpoint of synthetic method). The size-limited nanoparticles of <100 nm in a shorter dimension delivered good performances at fairly high rates when compared with a co-precipitated counterpart. This surface-confined precipitation method provides a cost-effective strategy for synthesizing high performance LMP, not including ball milling processes for pulverizing particles and mixing with carbon particles but enabling a continuous synthetic process.

Chapter 3. Hollow versus nonhollow: The electrochemical preference in a case study of the conversion reaction of Fe_3O_4

3.1 Introduction

Conversion-reaction-based materials such as transition metal oxides, sulfides, nitrides and phosphides have been considered as prospective anode materials of lithium ion batteries replacing the most conventionally used intercalation-based material, graphite. The main driving force to push them into a front is their high capacity estimated at around 1000 mAh g^{-1} which is much higher than the theoretical capacity of graphite at 372 mAh g^{-1} . The conversion-reaction-based materials can be described as binary compounds M_mX_x , where M = transition metal and X = anion with the corresponding stoichiometric coefficient m and x. M_mX_x is converted to its corresponding metal M embedded in Li_2X matrix during lithiation when negatively enough potential is applied. The reaction was revealed reversible on nano-dimensional particles of M_mX_x .^{59, 60} Despite of their high specific capacity, several drawbacks should be overcome. Low electric conductivity (e.g., $10^{-14} \text{ S cm}^{-1}$ at room temperature for $\alpha\text{-Fe}_2\text{O}_3$)⁶¹ leads to decreasing capacity with increasing discharge rate (1085 mAh g^{-1} at 0.1 C to 200 mAh g^{-1} at 5 C with nanoparticles of $<20 \text{ nm}$).⁶² Large volume change (volume expansion to more than 200% after lithiation)⁶³⁻⁶⁶ causes serious capacity decay after charge/discharge cycling (1083 mAh g^{-1} at the first cycle to 353 mAh g^{-1} at the 50th cycle at 0.1 C with nanoparticles of $\sim 50 \text{ nm}$).⁶⁷

Various strategies have been implemented to fix the shortcomings of the conversion-reaction-based materials.^{62, 68-78} One of the directions for improvement is to develop morphology to facilitate the accessibility of Li^+ ions into the primary particles of M_mX_x and simultaneously to enlarge the contact area between the material and electrolyte.^{64, 79-81} Hollow sphere nanostructures with their porous shell have been chosen to satisfy the requirements^{66, 81-90} because of (1) their large surface area on which active materials meet electrolyte and (2) the short pathways of Li^+ to pass through. By a simple calculation based on geometry, the surface area ratio of hollow to non-hollow sphere is 2.65 at a fixed mass (or at a fixed true volume with an identical density) and 1.64 at a fixed apparent volume when thickness of shell is 20% dimension of radius of hollow sphere ($t_h/r_h = 0.2$, e.g., 70-100 nm diameter sphere with 7-10 nm shell as shown in our hollow sphere) (Figure 3.1). Characteristic dimension of diffusion length is estimated at 3.5 to 5.0 nm (=shell thickness/2) for the hollow geometry and 27.6 to 39.4 nm (=radius) for its corresponding non-hollow geometry at the fixed-mass case. The hollow sphere nanostructure can be obtained by various methods. Inside-out Ostwald ripening led to a hollow structure of SnO_2 with diameter = 150 to 250 nm and shell thickness = 30 nm.⁹¹ Monodispersed Ga_2O_3 hollow

spheres (diameter = 370 nm and shell thickness = 16 nm) were obtained by a sacrificial carbon templates.⁹² A hollow sphere secondary structure of LiFePO₄ nanoparticles was prepared by a solubilization-reprecipitation mechanism caused by the difference of solubility products of two different precipitates (diameter = 300 nm and shell thickness = 25 nm).⁹³ Hollow Fe₂O₃ (diameter = ~1 μm and shell thickness = 50-100 nm) was obtained by a facile quasiemulsion-based soft template method.⁸⁴ Also, carbon coating on the surface of the conversion-reaction-based materials^{64, 69, 87, 88, 94} or compositing of the active materials with carbon such as graphene^{73, 83, 95, 96} is helpful in a way to enhance the electric conductivity of electrodes.

In this work, we show improved rate capability and cycle retention by shaping Fe₃O₄ as the conversion-reaction-based material to a hollow nanosphere that is carbon-coated (h- Fe₃O₄@C). Even though various carbon-coated as well as hollow-sphere-structured metal oxides were tried to achieve the same purpose, there have been few works to develop the hollow sphere structure of the conversion-reaction-based materials in tens of nm size exhibiting high capacities (e.g., >1000 mAh g⁻¹ at 0.1 C) for lithium ion batteries: ~1 μm diameter with 50-200 nm shell from previous works.^{82, 84, 87} As far as we know, a hollow γ- Fe₂O₃ of ~12.5 nm diameter with 2.5 nm-thick shell was reported, showing such a high capacity higher than 1000 mAh g⁻¹.⁸⁶ Another but more important point of this work is on comparing hollow sphere geometry with the corresponding non-hollow geometry in terms of electrochemical benefits. Dimension of non-hollow control was carefully selected in a way that mass of each nanoparticle is equivalent to that of each h- Fe₃O₄@C.

3.2 Experiments

3.2.1 Preparation

Spherical carbon colloids (CBall) of ~200 nm in diameter were synthesized as a hard template by hydrothermally heating an aqueous solution of glucose (18.016 g in 100 ml water) in a Teflon-lined stainless steel autoclave at 160 °C for 10 h. After natural cooling to room temperature, the CBall was washed five times by centrifuging its dispersion in de-ionized water and ethanol at 10,000 rpm (10,174 × g) for 20 min every time. 1 g of the CBall dried at 70 °C overnight was re-dispersed ultrasonically in 200 ml ethanol for 1 h. 2.424 g Fe(NO₃)₃·9H₂O was introduced into the CBall-dispersed solution, followed by vigorous stirring for 2 h. The Fe³⁺-adsorbed CBall (CBall@Fe³⁺), centrifugally washed with ethanol and then dried at 70 °C overnight, was thermally treated at 450 °C for 1 h with 2.5 °C min⁻¹ as a ramping speed in Ar/Air (80:20%) atmosphere to remove CBall and oxidize the adsorbed Fe³⁺. The resultant hollow Fe₂O₃ (h- Fe₂O₃) was mixed with an aqueous solution of sucrose (50 wt%), followed by heating at 90 °C with stirring to evaporate water. The sucrose-coated h- Fe₂O₃ was calcined at 500 °C for 1 h in argon atmosphere, forming h- Fe₃O₄@C. In addition to the hollow samples, a

commercially available non-hollow nanoparticulate Fe_2O_3 (nh- Fe_2O_3 , Alfa Aesar) was converted to nh- Fe_3O_4 @C in the same way as used for coating h- Fe_2O_3 with carbon.

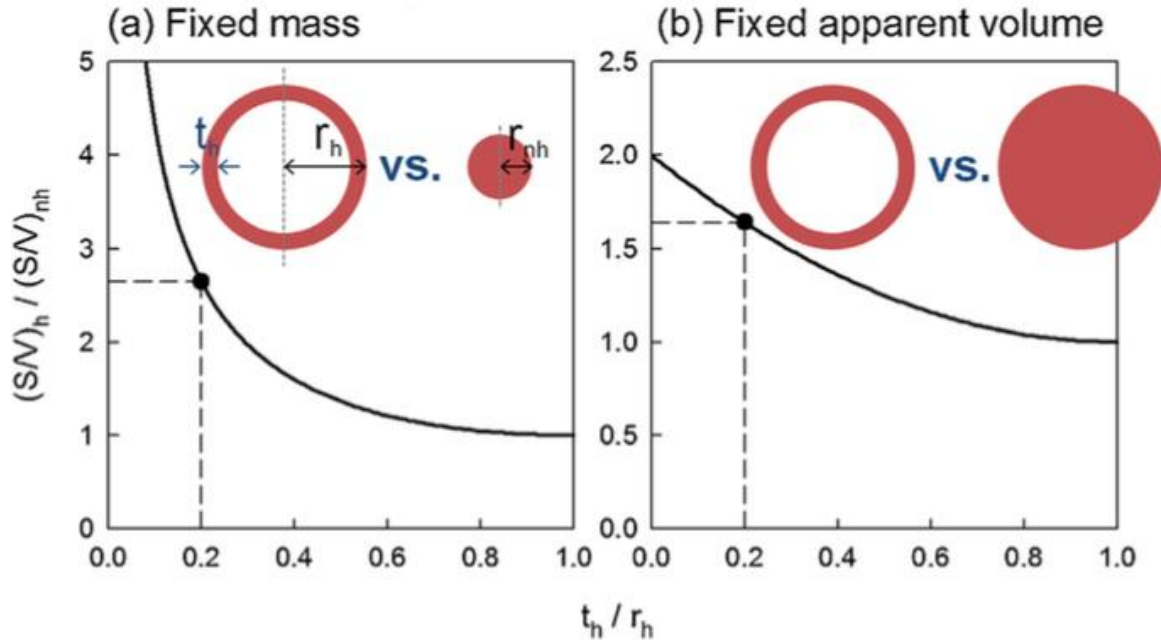


Figure 3.1. Ratio of surface-to-volume ratios (S/V) of hollow to nonhollow sphere geometry as the function of dimensionless number of shell thickness to particle radius of the hollow sphere at mass = constant with the assumption of density = constant (a) and at apparent volume = constant (b).

3.2.2 Electrochemical analysis

For electrochemical measurements, a 2032-type half coin cell configuration was adopted. As a working electrode, a 70:20:10 mixture of the active material (h- Fe_3O_4 @C), a conductive agent (Super P) and PAA/CMC (1:1, polyacrylic acid: carboxymethyl cellulose) as a binder was used, which is pasted on a Cu foil. The punched working electrode was assembled with a separator and lithium foil as a counter electrode in 1 M LiPF_6 in ethylene carbonated/diethylcarbonate (1:1, v/v) in an argon-filled glove box.

Cells were galvanostatically tested between 3.0 and 0.001 V vs. Li/Li^+ . The current for 1 C was defined as 1000 mA g^{-1} in this work (cf. theoretical capacity of Fe_3O_4 based on the conversion reaction = 926 mAh g^{-1}) because the capacities higher than theoretical values based on conversion reactions have been often obtained with the transition metal oxide anode materials.

3.3 Results and discussion

3.3.1 Morphological evolution of hollow structure

The h-Fe₃O₄@C was synthesized via a sacrificial hard-template method (Figure 3.2). Spherical carbon colloids of ~200 nm diameter were used as the template (CBall in Figure 3.2a-c), which were prepared by dehydrating glucose hydrothermally.⁹⁷ When Fe³⁺ ions are introduced into the ethanolic dispersion of the CBall, the positively charged Fe precursors are electrostatically attached to the negatively charged surface of the CBall (CBall@Fe³⁺ in Figure 3.2d-f). Zeta potential (ζ) of the carbon sphere colloids were estimated at -61 mV. The change of ζ to +6.4 mV after Fe³⁺ addition confirms that the positively charged ions were adsorbed onto the CBall (Figure 3.4a). Very tiny objects (<1 nm) identified as Fe³⁺ ions or their clusters (Figure 3.3) were found on the surface of CBall in high resolution transmission-electron-microscopic (TEM) images (the inset of Figure 3.2f). The dark-dotted surface is in exquisite contrast to the clean surface of CBall (the inset of Figure 3.2c).

By heating CBall@Fe³⁺ at 450 °C in a partial pressure of oxygen, CBall was completely removed, leaving a spherical shell of Fe₂O₃ hematite with a void space in its center (h- Fe₂O₃ in Figure 3.2g-i). The diameter of sphere significantly decreased from ~200 nm of CBall to less than 100 nm of h- Fe₂O₃. The shrinkage results from further dehydration of the loosely cross-linked structure of the carbon spheres followed by complete oxidation of carbon with Fe³⁺ ions densified in surface layer⁹² or separate Fe₂O₃ islands aggregated. The continuous shell of interconnected Fe₂O₃ is evolved following the decreasing contour of CBall along the course of carbon removal. The resultant thickness of shell of h- Fe₂O₃ was ~10 nm.

For carbon coating to enhance the electric conductivity and to mitigate volume change during charging and discharging, the mixture of h-Fe₂O₃ powders with sucrose were calcined at 500 °C in an inert atmosphere (h-Fe₃O₄@C). The carbonization temperature was selected based on the experimental evidence that hematite Fe₂O₃ is fully reduced to Fe⁰ metal above 600 °C in our preliminary experiments. 7 wt% carbon (measured by a combustion-based elemental analysis) was coated on the surface of nanospheres while Fe₂O₃ in a single oxidation state of Fe(III) was carbo-reduced to Fe₃O₄ in a mixed oxidation state of Fe(III) and Fe(II). After the oxide formation (Fe₂O₃ and Fe₃O₄), the values of ζ returned to the negative figures since the positive charges of Fe³⁺ were matched and more overwhelmed by electronegativity of oxygen.

1. CBall

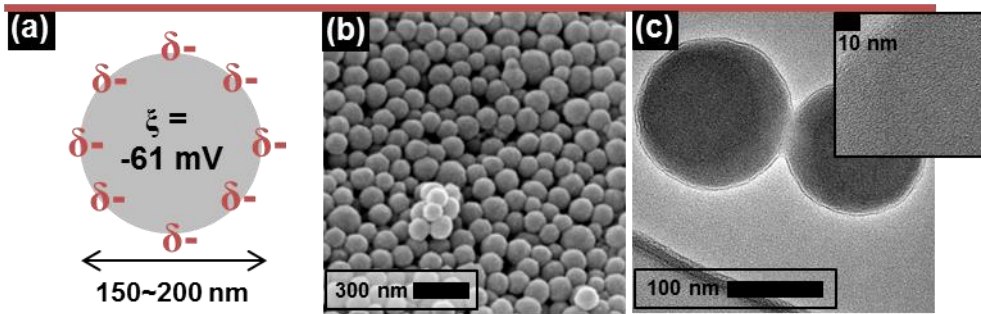
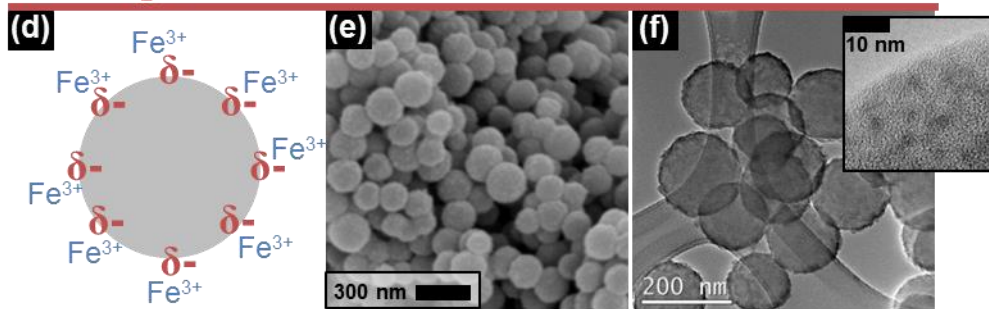
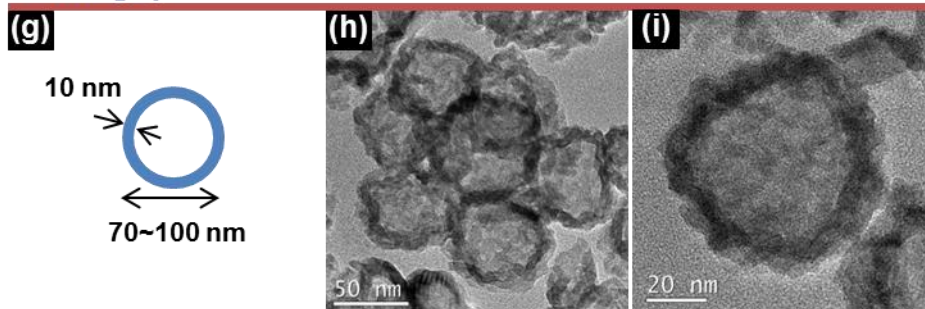
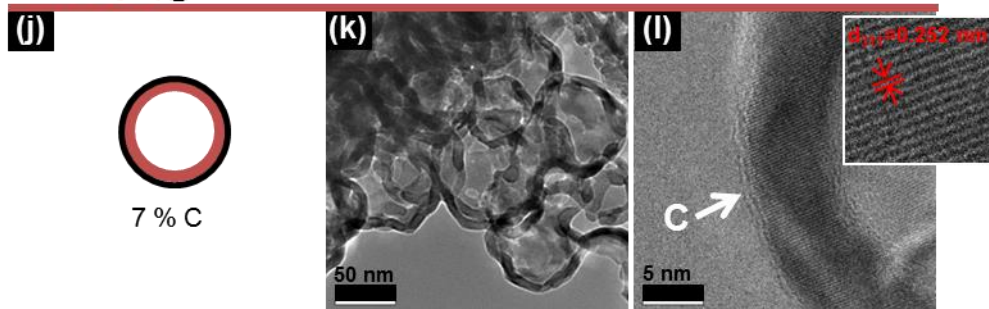
2. CBall@Fe³⁺3. h-Fe₂O₃4. h-Fe₃O₄@C

Figure 3.2. Evolution from carbon balls (CBall, a-c) via Fe³⁺-adsorbed CBall (C@Fe³⁺, d-f) and hollow-sphere-structured Fe₂O₃ (h-Fe₂O₃, g-i) to carbon-coated hollow-sphere-structured Fe₃O₄ (h-Fe₃O₄@C, j-l): schematic diagrams for the first column; scanning electron microscopic (SEM) images for b and e; and transmission electron microscopic (TEM) images for others. White arrow in l indicates carbon layer.

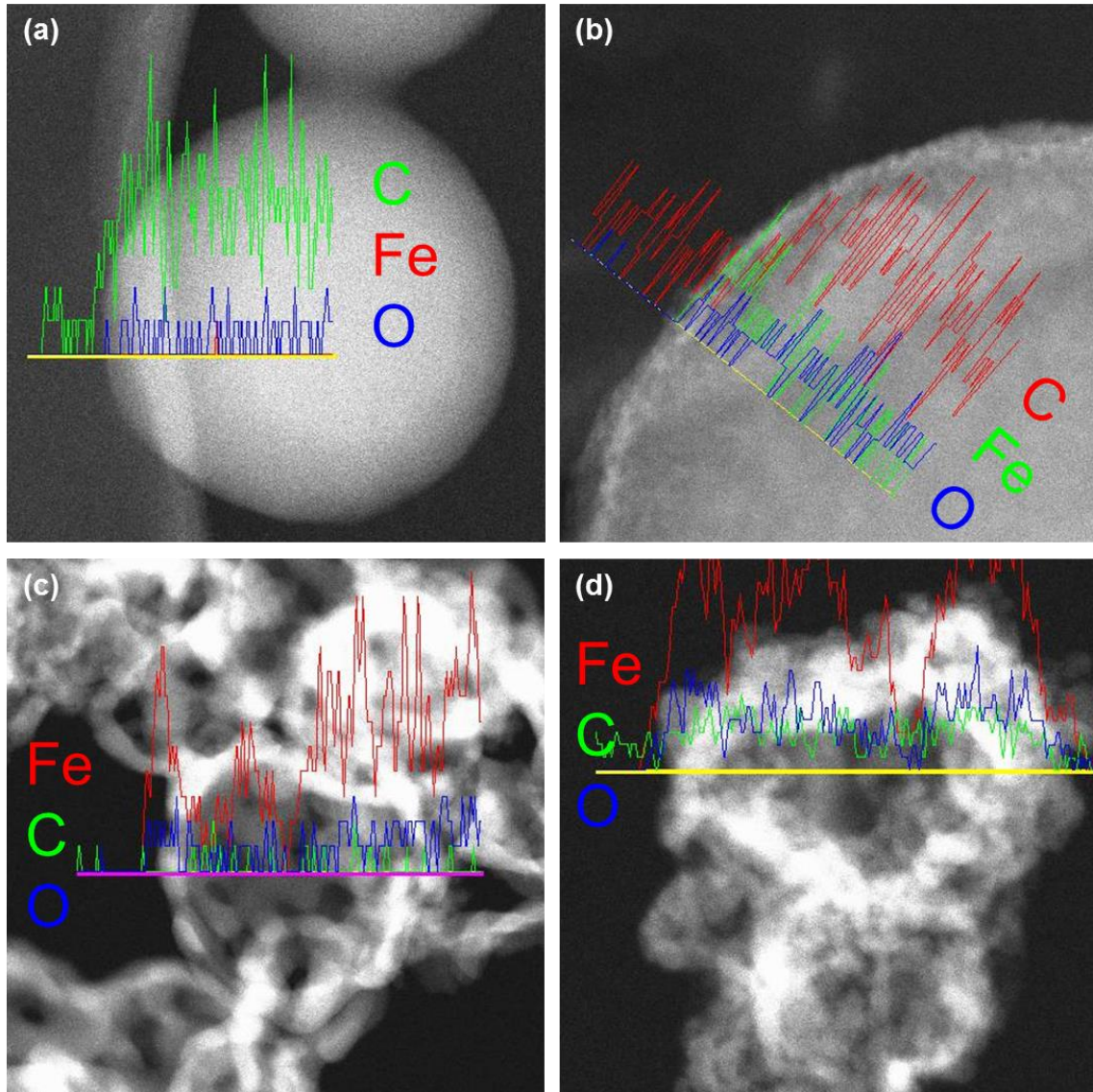


Figure 3.3. Line mapping of each element identified by energy dispersive spectra (EDS): (a) CBall, (b) CBall@Fe³⁺, (c) h-Fe₂O₃ and (d) h-Fe₃O₄@C

X-ray diffraction patterns confirm the formation of Fe₂O₃ and its conversion to Fe₃O₄ in presence of sucrose as the carbon precursor(Figure 3.4b). In addition to our hollow samples, commercially available non-hollow nanoparticular Fe₂O₃ (nh-Fe₂O₃, 20 to 40 nm size provided by Alfa Aesar, 50 to 80 nm agglomerates as shown in Figure 3.5) and its converted form with carbon coating (nh- Fe₃O₄@C) were compared. It should be emphasized that the size of selected nanoparticles is around the dimension of solid spheres that have the mass equivalent to that of our h-Fe₂O₃ or h-Fe₃O₄@C as mentioned above (27.6 to 39.4 nm × 2 = 55 to 80 nm in the secondary agglomerate level). The h-Fe₂O₃ was identified as hematite while the nh-Fe₂O₃ was maghemite. After calcination in presence of carbon precursor, there were no significant crystallographic differences between hollow and the corresponding non-hollow

Fe₃O₄@C in terms of a qualitative viewpoint (magnetite). The main peak indicating (311) corresponds to 0.252 nm spacing of the crystalline lattice fringe shown in TEM image (Figure 3.2l).

Pore size distributions calculated from nitrogen adsorption isotherms confirm the morphology revealed by electron microscopy, providing more detailed information of morphology of the shells of hollow samples (Figure 3.4c). Barrett, Joyner and Halenda method (BJH) and Horvath-Kawazoe method (HK) were used to calculate pore size distribution of meso/macropores and micropores, respectively. The hollow iron oxides (h-Fe₂O₃ and h-Fe₃O₄@C) had around 80 nm voids, the value of which is consistent with the information of TEM images (Figure 3.2h and i). Micropores at around 1.2 nm were developed probably in the shell of the hollow particles, which are responsible for 5.0% or 9.4% of total pore volume ($V_{\text{tot}} = 0.8$ to $0.64 \text{ cm}^3 \text{ g}^{-1}$ for h-Fe₂O₃ to h-Fe₃O₄@C) and 4.8 to 32% of total surface area calculated by Brunauer, Emmett and Teller equation ($S_{\text{BET}} = 84$ to $89 \text{ m}^2 \text{ g}^{-1}$). Most of surface area and pore volume comes from the inner and outer surface of shell of the hollow particles while porous morphology of coated carbon layers contributed to the additional increase of micropores. On the other hand, there were little macropores with non-hollow particles even if they have micropores at the same micropore dimension of hollow samples. The micropores would come from inter-particle voids resulting from agglomeration. The origin of micropores of hollow samples is believed to be the same, that is to say, the space developed with Fe₂O₃ island aggregation during the removal process of carbon core template. S_{BET} was estimated at $41 \text{ m}^2 \text{ g}^{-1}$ for nh-Fe₂O₃, which is a half of S_{BET} of hollow particles. The relative ratio of S_{BET} of the hollow to the non-hollow is 2.05, which is at least roughly consistent with the value calculated based on geometry above (2.65). The deviation from calculated values comes from the fact that a fraction of the non-hollow nanoparticles has dimensions smaller than the size of solid spheres that have the mass equivalent to that of our h-Fe₂O₃ or h-Fe₃O₄@C. The increase of surface area to $75 \text{ m}^2 \text{ g}^{-1}$ with carbon coating results from porous structure of carbon layer (9.8 wt%). However, V_{tot} was conspicuously reduced from 0.22 to $0.05 \text{ cm}^3 \text{ g}^{-1}$, implying that inter-particle micro-voids were filled up with the porous carbon.

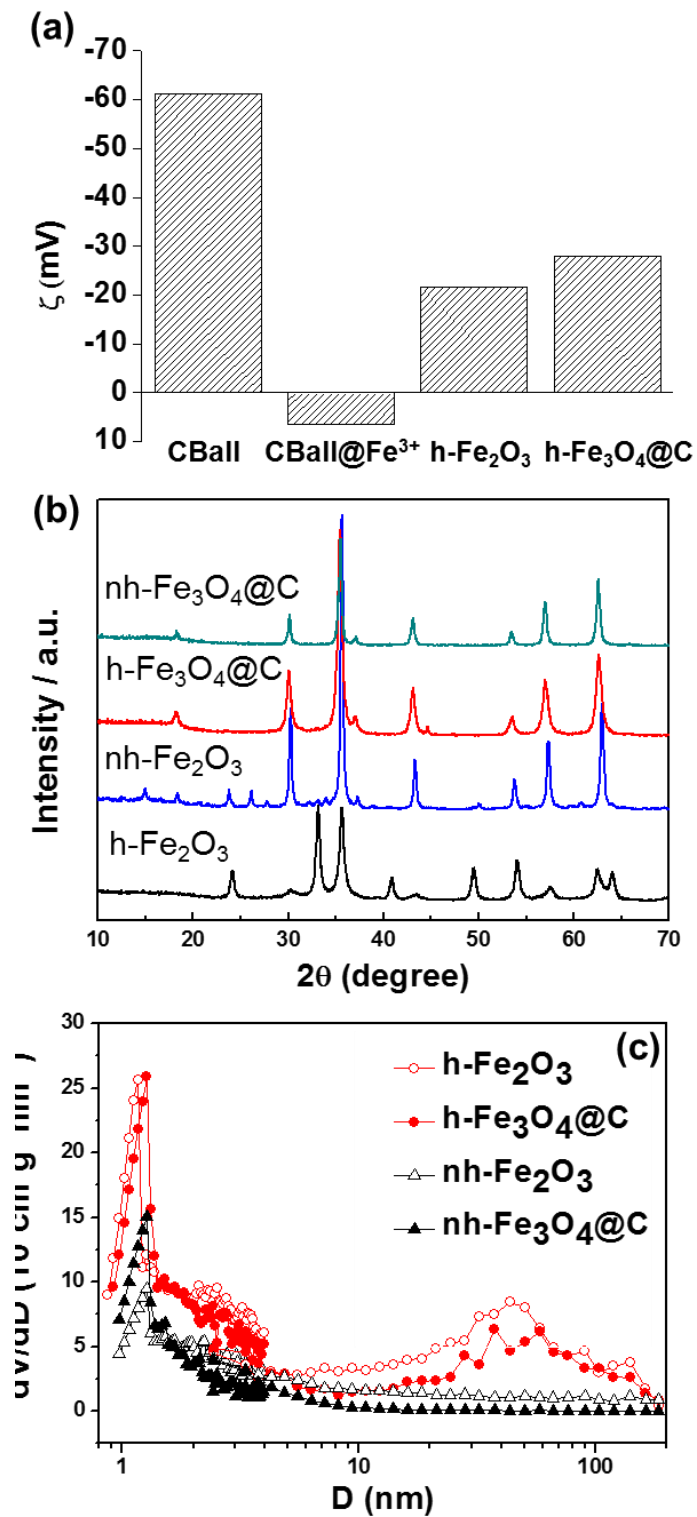


Figure 3.4. (a) Change of zeta potentials (ζ) of CBall to h-Fe₃O₄@C. (b) X-ray diffraction patterns of hollow and non-hollow Fe₂O₃ and Fe₃O₄@C. (c) Pore size distribution calculated from N₂ adsorption/desorption isotherms.

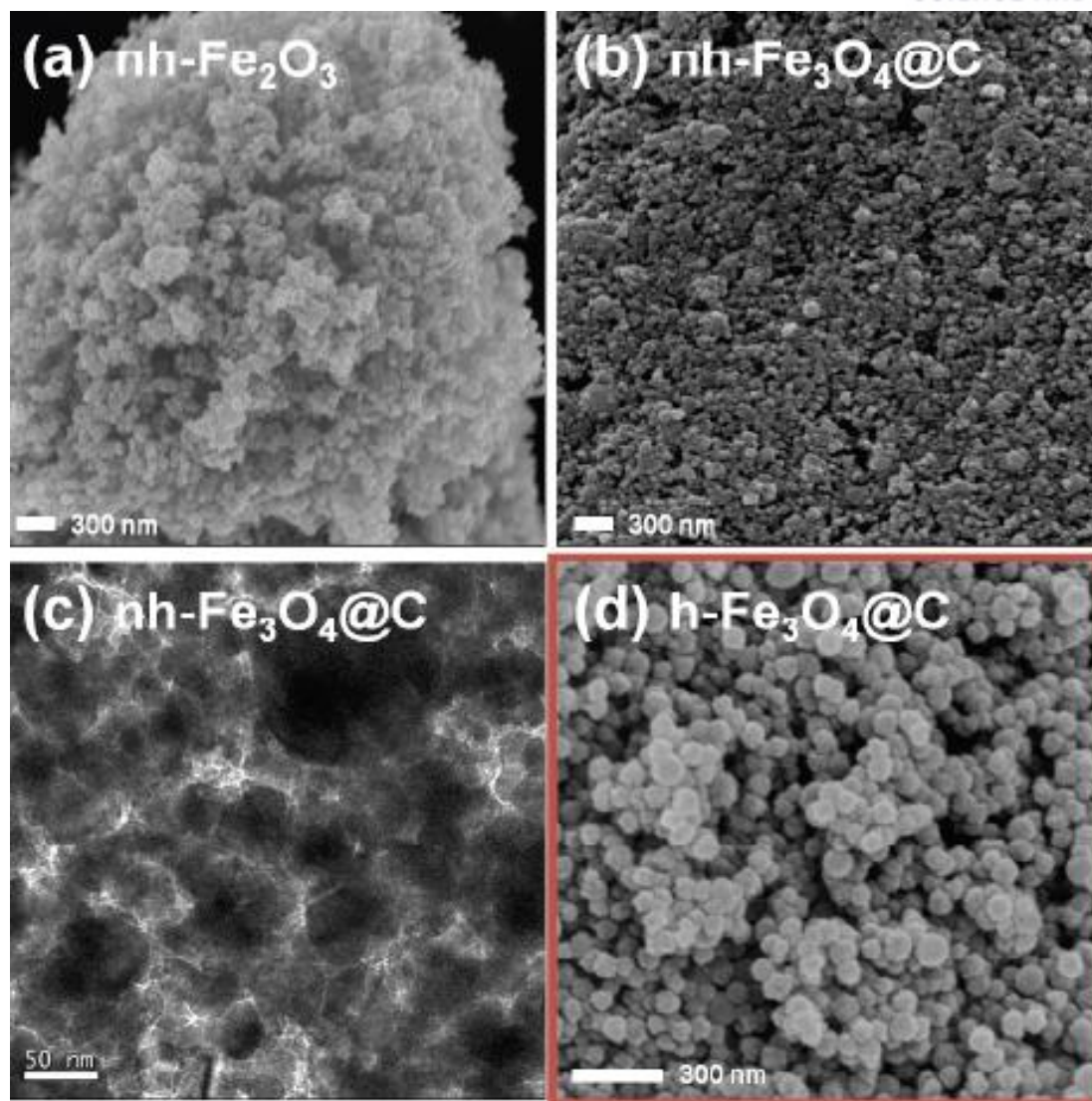


Figure 3.5. Electron microscopic images of non-hollow controls: (a) nh- Fe_2O_3 ; (b and c) nh- $\text{Fe}_3\text{O}_4@C$; and (d) h- $\text{Fe}_3\text{O}_4@C$ for comparison. (SEM for a, b and d; TEM for c)

3.3.2 Electrochemical preference of hollowness to non-hollowness

Carbon-coated hollow and non-hollow Fe_3O_4 particles (h- $\text{Fe}_3\text{O}_4@C$ and nh- $\text{Fe}_3\text{O}_4@C$) were electrochemically tested as an anode material of lithium ion batteries (Figure 3.6). The assembled coin half cells of h- $\text{Fe}_3\text{O}_4@C$ were initially lithiated from their open circuit voltages at ~ 3.0 V versus Li/Li^+ up to 0.001 V, showing two plateaus at different potentials (~ 0.9 V for the first and ~ 0.76 V for the second) (Figure 3.6a). Li^+ ions are intercalated into the conversion-reaction-based material at the first plateau before the conversion to Fe^0 metal that was embedded in Li_2O medium at the second plateau.⁶⁰ The sloping potential profile after the second or conversion plateau (< 0.76 V) is associated with formation of gel-like polymer films caused by metal-catalyzed electrolyte decomposition.⁹⁸ The

reversible conversion reactions were realized from the second cycle with both carbon-coated hollow and non-hollow Fe_3O_4 particles after the initial irreversibility was experienced at $\eta = 85.6\%$ ($=1098 \text{ mAh g}^{-1}/1283 \text{ mAh g}^{-1}$) with h- $\text{Fe}_3\text{O}_4@\text{C}$ and at $\eta = 90\%$ ($=441 \text{ mAh g}^{-1}/490 \text{ mAh g}^{-1}$) with nh- $\text{Fe}_3\text{O}_4@\text{C}$ (coulombic efficiency, $\eta = Q_{\text{dCh}}/Q_{\text{Ch}}$ where $Q = \text{capacity}$, dCh = discharge or delithiation and Ch = charge or lithiation). The initial efficiency (η at the first cycle) is higher than the values previously reported at 54.5 to 79%.^{66, 73, 75, 85} The values of η from the second cycles were kept beyond 98.6% for both carbon-coated Fe_3O_4 particles.

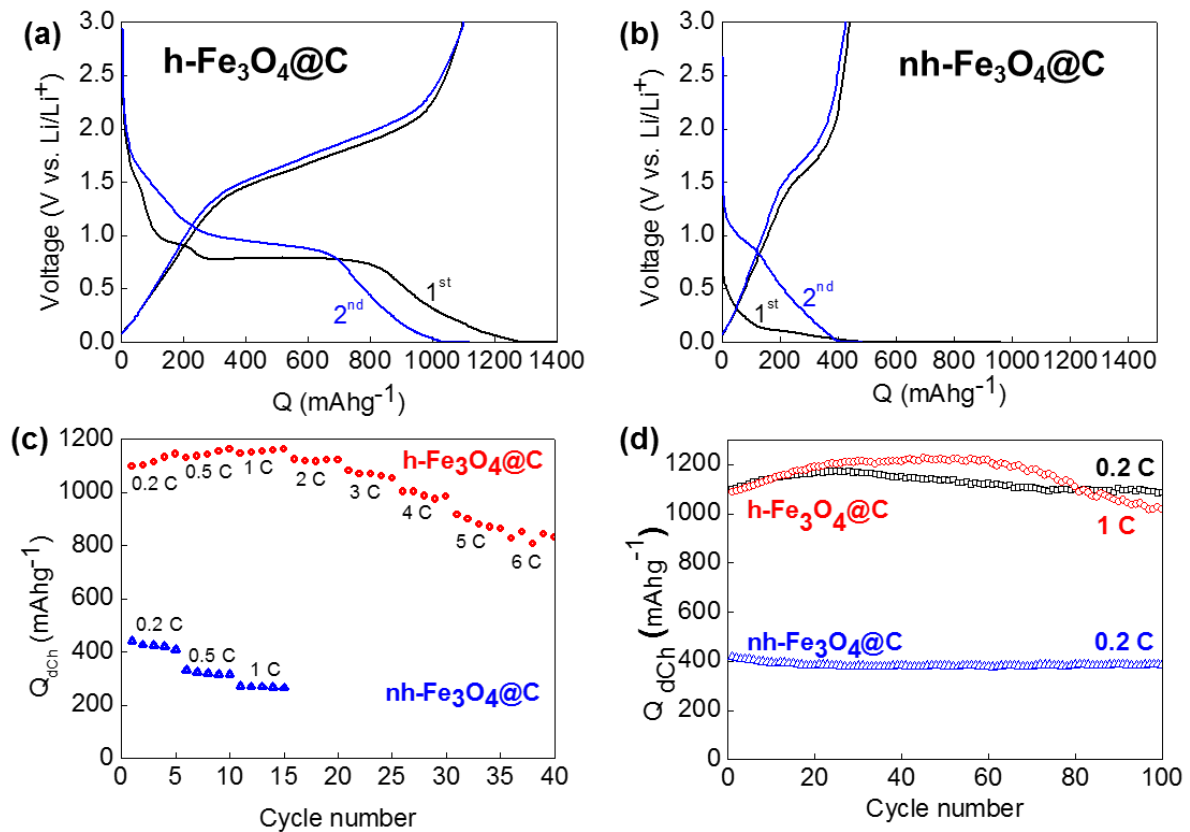


Figure 3.6. (a and b) The potential profiles during charge (lithiation) and discharge (delithiation) at the first and second cycle of h- $\text{Fe}_3\text{O}_4@\text{C}$ (a) and nh- $\text{Fe}_3\text{O}_4@\text{C}$ (b). (c) Discharge capacity (Q_{dCh}) change as a function of C-rate. (d) Cycle retention at 0.2 C and 1 C.

When compared with the non-hollow samples, the hollow Fe_3O_4 showed clearly enhanced rate capability (Figure 3.6c). The discharge capacities were delivered above 1100 mAh g^{-1} with h- $\text{Fe}_3\text{O}_4@\text{C}$ up to 2 C, followed by the capacity decrease at higher C-rates to 830 mAh g^{-1} at 6 C. The capacity of the hollow at 1 C ($\sim 1150 \text{ mAh g}^{-1}$) are ~ 4 times as high as that of the non-hollow (266 mAh g^{-1}) at the same rate as our own control. When compared with top three capacity records at high C-rates

in literatures, our capacity values from h- Fe₃O₄@C is the highest or at least most competitive: c.f. 922 mAh g⁻¹ at 1 C with porous hollow microsphere (diameter = 400 to 500 nm composed of 30 to 40 nanoparticles)⁶⁶; 1000 mAh g⁻¹ at 1 C with nanorods (width = ~50 nm, length = ~250 nm and thickness = ~20 nm) embedded in a network of single wall carbon nanotubes⁷³; 1050 mAh g⁻¹ at 0.2 C with 3D graphene/ Fe₃O₄ nanoparticle aerogel (diameter = 10 nm)⁷⁵.

In conversion reactions, severe pulverization of metal oxides caused by large volume expansion is a staple issue.⁶³⁻⁶⁵ The strong tolerance to volume expansion of our hollow nanostructure was confirmed by stable cycle retention at least up to 100 cycles at 0.2 C and 1 C (Figure 3.6d). The capacity decay relative to the capacity at the first cycle during discharge was 98.5% at 0.2 C and 92.1% at 1 C after 100 cycles. The non-hollow control also showed the stable cycle retention but the level of capacity was much lower. No significant morphological change of h-Fe₃O₄@C was observed even after 100 cycles at 1 C while vestiges resulting from serious volumetric change were found in the non-hollow counterpart (nh-Fe₃O₄@C) (Figure 3.7).

In terms of electrochemical preference between hollow and non-hollow sphere geometry in a fixed-mass case or when the geometries are compared in the same mass of electroactive material, it looks clear that hollow design of particles are superior to the corresponding non-hollow structure. This conclusion is based on gravimetrically normalized properties such as capacity in a unit of mAh g⁻¹ or energy density Whr kg⁻¹. When thinking about volumetrically normalized properties such as capacity in a unit of mAh cm⁻³, it is easily guessed that the hollow structure would provide performances inferior to the non-hollow counterpart due to its coarse geometry including large voids at its center. However, our Fe₃O₄ case study shows that it is not always true especially at high discharge rates. Considering the relative density of hollow to non-hollow (d_h/n_h) = 0.49 at t_h/r_h = 0.2, the ratio of gravimetric capacity of hollow to non-hollow at 1 C estimated at ~4 (1100 mAh g⁻¹/266 mAh g⁻¹) leads to the ratio of volumetric capacity at ~2. Hollow structure is still two times beneficial superior to non-hollow one in terms of volumetric capacity. The kinetic advantage of the hollow structure would be more and more emphasized as discharge rates increase.

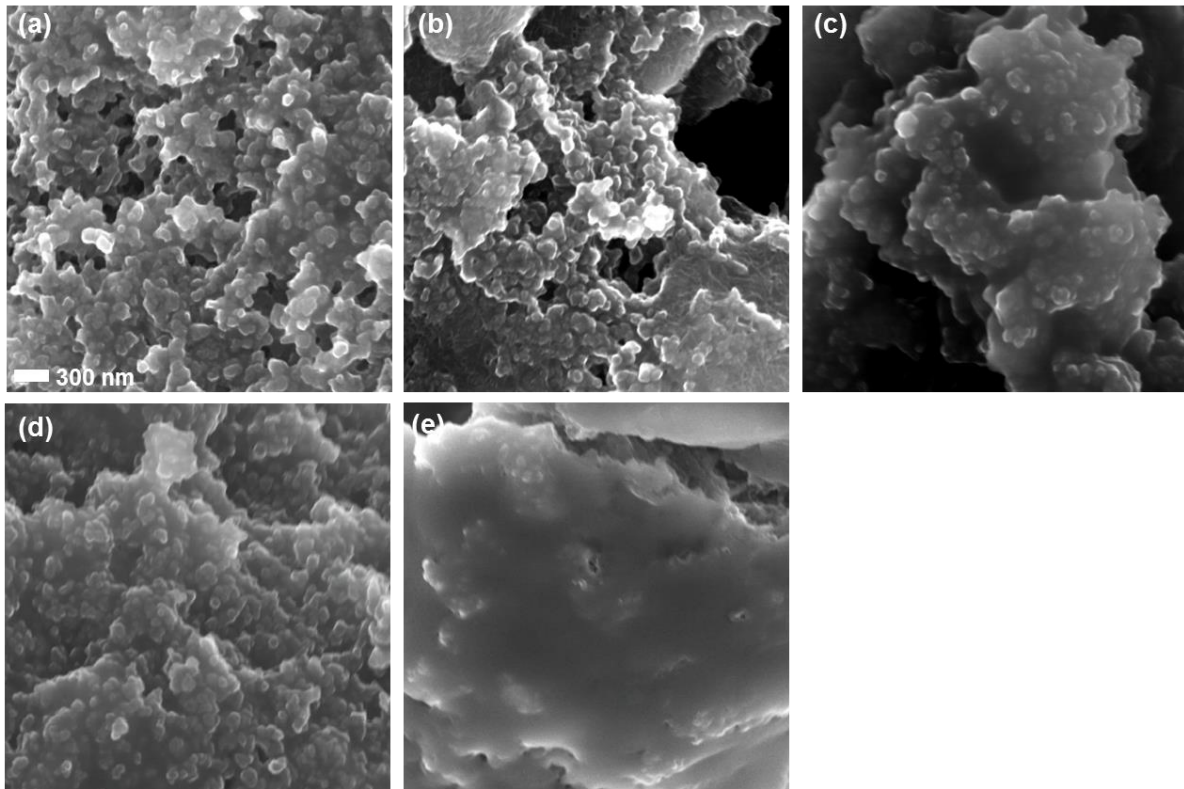


Figure 3.7. SEM images of electrode composites based on h- $\text{Fe}_3\text{O}_4\text{@C}$ (a to c) and nh- $\text{Fe}_3\text{O}_4\text{@C}$ (d and e) for comparison between before (a and d) and after (b and e) one hundred charge/discharge cycles at 0.2C or at 1C (c). The electrode composites consisted of a 70:20:10 mixture of the active material (h- $\text{Fe}_3\text{O}_4\text{@C}$ or nh- $\text{Fe}_3\text{O}_4\text{@C}$), a conductive agent (Super P) and PAA/CMC (1:1, polyacrylic acid/carboxymethyl cellulose) as a binder. The scale bar in (a) is applied to other images.

3.4 Conclusion

As a summary, we fabricated a carbon-coated hollow-sphere-nanostructured Fe_3O_4 (h- $\text{Fe}_3\text{O}_4\text{@C}$) by using a sacrificial hard template. Its hollow void of ~ 80 nm diameter accommodated volume expansion during charging while the porous shell structure enabled facile Li^+ ion transfer and enhanced accessibility to surface of the active material. Also, the carbon coating layer of the h- $\text{Fe}_3\text{O}_4\text{@C}$ enhanced electric conductivity, presumably partly responsible for depressing pulverization of the metal oxide. Due to the synergetic effects of all, the h- $\text{Fe}_3\text{O}_4\text{@C}$ worked kinetically faster as well as operationally more stable as an anode material of lithium ion batteries, compared with its non-hollow counterpart.

Chapter 4. Preparation of Co_3O_4 electrode materials with different microstructures *via* pseudomorphic conversion of Co-based metal-organic frameworks

4.1 Introduction

MOF-derived metal oxide nanocomposites are utilized as electrode materials for energy storage and conversion. Cho and co-workers reported the use of MIF-88-Fe synthesis as a precursor for the synthesis of nanoporous spindle-like $\alpha\text{-Fe}_2\text{O}_3$, which functions as an improved electrode material for lithium ion batteries (LIBs). This material was composed of 20 nm-sized primary nanoparticles, resulting in a nanoporous secondary structure.⁹⁹ Ogale et al. synthesized CuO nanostructures from a Cu-based MOF under an air atmosphere. The samples, which have a highly aggregated particulate morphology of ca. 40 nm CuO nanoparticles, displayed good electrochemical performances as an anode for LIBs.¹⁰⁰ By pyrolyzing $[\text{Co}_3(\text{NDC})_3(\text{DMF})_4]_n$ (NDC $\frac{1}{4}$ 2,6-naphthalenedicarboxylate; DMF $\frac{1}{4}$ N,N-dimethylformamide), Xu et al. synthesized agglomerated secondary structures with an average diameter of around 250 nm, which contained primary Co_3O_4 nanoparticles with a size of about 25 nm. This agglomerated Co_3O_4 material exhibited enhanced capacities and cyclability as an electrode material for LIB.¹⁰¹ Examples such as these illustrate that the development of metal oxide nanostructures as electrode materials for LIBs have largely focused on the use of primary nanoparticles and their agglomerated particles.

In addition to the effects of primary nanoparticles and secondary structures on electrochemical performances, it is worthwhile to investigate tertiary architectures between 10 to 100 μm as the highest level, which correspond to macroscopic shapes. Electric and ionic pathways to the redox-active sites of the primary particles are determined by secondary structure.^{52, 102-104} The tight integration of secondary structures is also crucial for enhanced charge transfer if other conductive agents are not present between the secondary agglomerates. Therefore, an important means of maximizing electrochemical performance involves the integration of secondary structures, which influences the tertiary structure. To the best of our knowledge, there are no reported comparison studies of metal oxide electrode materials having different macroscopic morphologies. Proper heat treatment of MOFs leads to pseudomorphic conversion with the retention of the parent MOF morphology. In other words, metal oxide nanostructures composed of the same primary particles, but with different secondary or tertiary architectures, can be generated via the pyrolysis of MOFs. By implementing this approach, the synthesis of two different MOFs comprising the same building blocks can provide an opportunity to study how macroscopic structure affects practical application.

Herein, we report the synthesis of two kinds of Co_3O_4 nanomaterials through pseudomorphic conversion wherein the macroscopic morphologies of the parent MOFs were well-maintained. We successfully synthesized both plate-shaped ($[\text{Co}_3(\text{BDC})_3(\text{DMF})_4]_n$, p-MOF) and rod-shaped ($[\text{Co}(\text{BDC})(\text{DMSO})]_n$, r-MOF) Co-MOFs, which are constructed from the same Co^{2+} ions and 1,4-benzenedicarboxylate (BDC) ligands. After optimized thermolysis, the Co-MOFs were transformed into Co_3O_4 materials having plate-like (p- Co_3O_4) or rod-like (r- Co_3O_4) morphologies, respectively. The electrochemical performances of these Co_3O_4 materials as LIB electrodes were investigated with respect to metal oxide microstructure.

4.2 Experiments

Two different shaped Co_3O_4 (plate and rod) were synthesized by the Moon's group.¹⁰⁵

4.2.1 Electrochemical measurements

The electrochemical properties of p- Co_3O_4 and r- Co_3O_4 were characterized using coin-type cells (CR2032) assembled in an Ar-filled glove box. The electrodes were fabricated by mixing the cobalt oxide powders (p- Co_3O_4 or r- Co_3O_4) with polyvinylidene fluoride (PVDF) as a binder and with Super P as a conducting agent at a weight ratio of 8 : 1 : 1 in N-methyl-2-pyrrolidinone solvent. The slurry was cast onto Cu foil and then dried in a vacuum oven at 120 °C for 2 h. A piece of polyolefin membrane, used as a separator, was placed between a piece of electrode and Li metal, used as a counter electrode. A 1 M solution of LiPF_6 in a mixture of ethylene carbonate (EC) and diethyl carbonate (DEC) at 1 : 1 v/v was used as an electrolyte. All the assembled coin cells were initially lithiated to 0.001 V at 0.1 C and then delithiated up to 3 V at the same rate. The conditions for the following galvanostatic lithiation and delithiation were indicated in figure captions in electrochemical tests for measuring cyclability and rate capability. 1 C was defined as 890 mA g^{-1} , considering the theoretical capacity calculated based on the conversion reaction of Co_3O_4 into Co and Li_2O (890 mAh g^{-1}).

4.3 Results and discussion

The textural properties of p- and r- Co_3O_4 , such as primary nanoparticles, secondary structures, and tertiary architectures, were carefully investigated by SEM and TEM (Figure 4.1). Because the organic components in MOFs are decomposed and liberated from the solid crystals during conversion, cracks on the crystal surfaces were observed but the external plate-like and rod-like morphologies remained. High magnification SEM and TEM images provide detailed structural information of p- Co_3O_4 and r- Co_3O_4 . As shown in TEM images (Figure 4.1b and e), the primary particles of Co_3O_4 in both the materials are observed as ca. 10 nm-sized nanocrystals, which were in agreement with the results

estimated by applying the Debye-Scherrer equation to the (311) reflection (diameters of 11 nm for both). Within $p\text{-Co}_3\text{O}_4$ and $r\text{-Co}_3\text{O}_4$ nearly identical primary particles agglomerated to form the secondary structures (100-300 nm), which finally constructed macroscopic tertiary architectures (a more intimate illustration is shown in Figure 4.2). As shown in Figure 4.1c and f, while $p\text{-Co}_3\text{O}_4$ was composed of secondary particles without the integrity between primary particles, the secondary particles of $r\text{-Co}_3\text{O}_4$ were monolithically well-integrated or connected to each other. To assess the porosity of the $p\text{-Co}_3\text{O}_4$ and $r\text{-Co}_3\text{O}_4$ structures, which is determined by secondary and tertiary structures, nitrogen adsorption-desorption measurements were conducted. As shown in Figure 4.3, $p\text{-Co}_3\text{O}_4$ and $r\text{-Co}_3\text{O}_4$ showed typical type IV isotherms with H3 hysteresis, indicating the presence of mesopores. The Brunauer-Emmett-Teller (BET) surface areas for $p\text{-Co}_3\text{O}_4$ and $r\text{-Co}_3\text{O}_4$ were $57\text{ m}^2\text{ g}^{-1}$ and $12\text{ m}^2\text{ g}^{-1}$, and the total pore volumes were 0.28 cc g^{-1} and 0.08 cc g^{-1} , respectively. The porosity difference between $p\text{-}$ and $r\text{-Co}_3\text{O}_4$ is attributed to the differing assemblage densities of primary Co_3O_4 nanocrystals as mentioned above. Consequently, compared with $r\text{-Co}_3\text{O}_4$, the higher surface area and porosity of $p\text{-Co}_3\text{O}_4$ imply a looser packing of nanoparticles in each plate in addition to spacing between the stacked plates. The pore size distribution curves analyzed by the nonlocal density functional theory (NLDFT) algorithm also supported these explanations. While the mesopores in $p\text{-Co}_3\text{O}_4$ are broadly distributed from 2 to 26 nm, $r\text{-Co}_3\text{O}_4$ possesses narrow pores ranging from 2 to 8 nm.

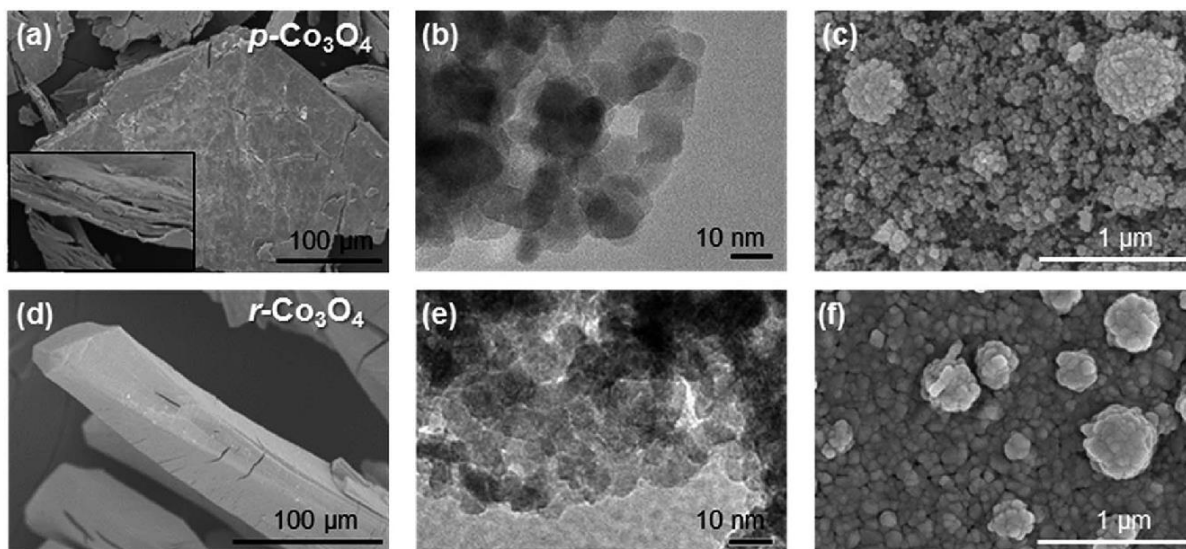


Figure 4.1. SEM and TEM images. (a-c) for $p\text{-Co}_3\text{O}_4$ and (d-f) $r\text{-Co}_3\text{O}_4$.

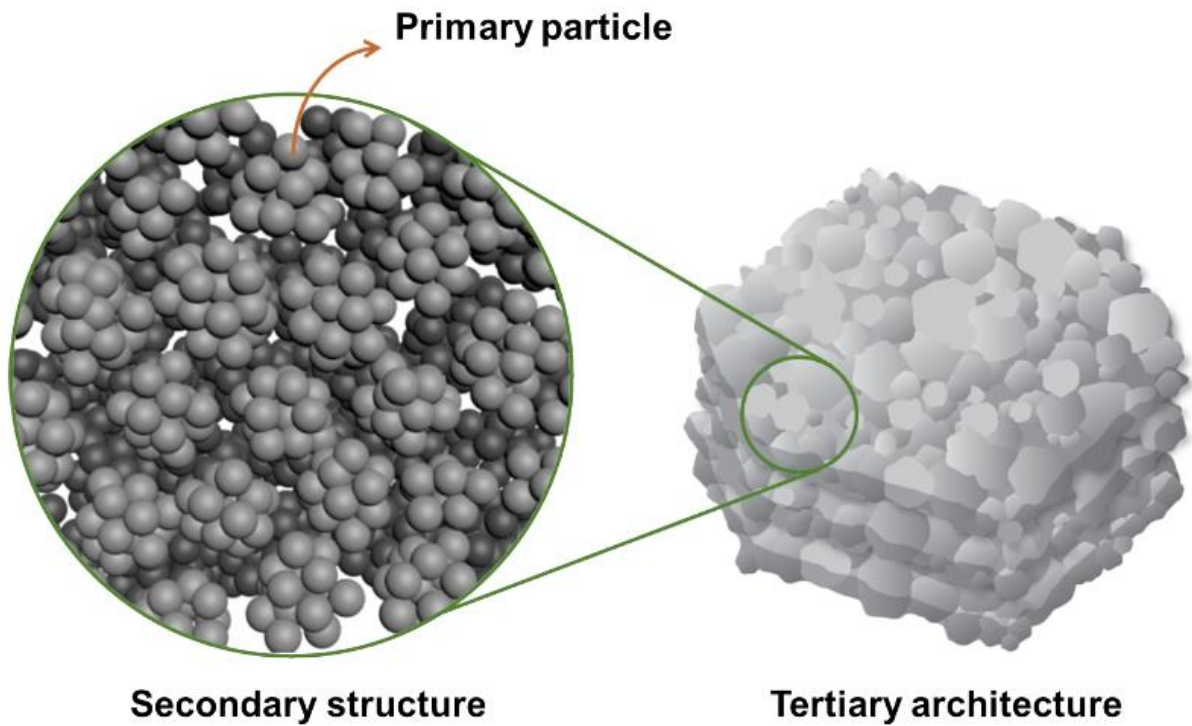


Figure 4.2. Illustration of a hierarchical structure in Co_3O_4 nanomaterials. Within $p\text{-Co}_3\text{O}_4$ and $r\text{-Co}_3\text{O}_4$ nearly identical primary particles are agglomerated to form the secondary structures (100 to 300 nm), which finally construct the macroscopic tertiary architectures.

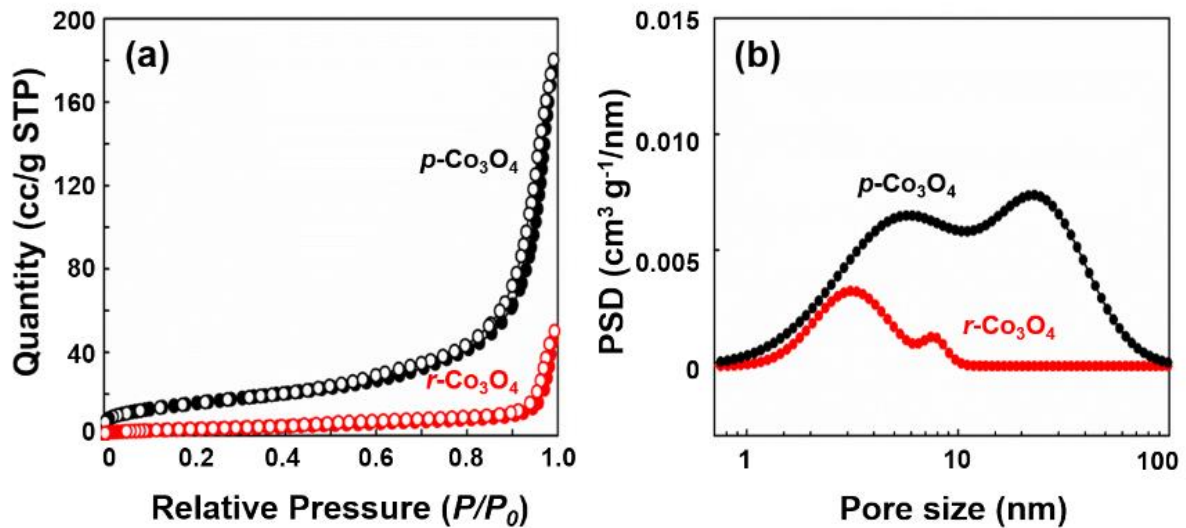


Figure 4.3. (a) N_2 sorption isotherms and (b) NLDFT pore size distribution curve of $p\text{-Co}_3\text{O}_4$ as black one and $r\text{-Co}_3\text{O}_4$ as red one.

The dependency of electrochemical characteristics on our Co_3O_4 nanostructures was investigated (Figure 4.4). As previously mentioned, the structures of our Co_3O_4 can be interpreted as multi-levelled. Primary particles of around 10 nm are similar for both p- Co_3O_4 and r- Co_3O_4 ; however, in terms of their secondary and tertiary architectures, cobalt oxides showed different degrees of assemblage as well as macroscopic shapes such as stacked plates or independent rods. Therefore, the morphological determinants of electrochemical performance can be described in terms of secondary structures and macroscopic, tertiary architectures.

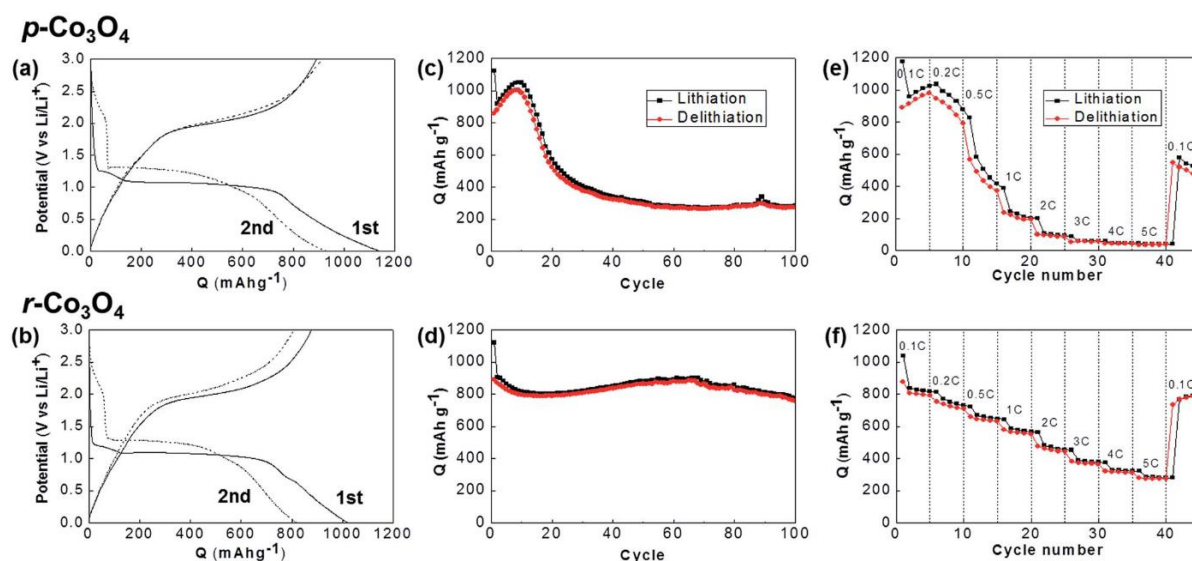


Figure 4.4. Electrochemical characteristics of p- Co_3O_4 and r- Co_3O_4 in the left and right columns, respectively. (a and b) Potential profiles during lithiation and delithiation at the first and second cycles. (c and d) Capacity retention during the repeated cycles of charge and discharge at 0.1 C for 100 cycles. (e and f) Capacity dependency on discharge rates. Charge rates were fixed at 0.1 C.

Both the cobalt oxides were lithiated by the same electrochemistry of the conversion reaction. During the initial lithiation caused by the negative potential shift, the solvent molecules of electrolyte were decomposed to form a solid electrolyte interface (SEI) layer at 1.2 V for both Co_3O_4 (Figure 4.4a and b). In the Li_2O matrix, the conversion reaction of Co_3O_4 to Co metal proceeded at a well-defined reduction potential, 1 V, which is responsible for the electrochemically reversible capacities. Additional capacities were delivered because of the pseudocapacitance of the gel-like polymer films formed at the potential-decreasing region after the conversion reactions.⁹⁸ Therefore, the capacities of Co_3O_4 have often been overestimated at values larger than the theoretical capacity of Co_3O_4 , calculated only on the basis of its conversion reaction (890 mAh g^{-1}). During subsequent delithiation, reverse reactions

proceeded, including pseudocapacitance discharging and backward conversion reactions. Size-confined Co metal particles catalytically decompose Li_2O during the backward conversion reaction forming Co_3O_4 .¹⁰⁶ Therefore, a capacity loss is involved between lithiation and delithiation at the first cycle because of the irreversible SEI formation reaction. However, the reversibility of the conversion reaction is guaranteed after the second cycle, showing coulombic efficiency higher than 95%.

Even if very similar electrochemical behaviors were observed during the initial cycles, the measured stability and kinetics of p- and r- Co_3O_4 were significantly different. The p- Co_3O_4 showed unstable capacity retention with a capacity increase up to the 10th cycle followed by a dramatic decrease up to the 20th cycle (Figure 4.4c). Conversely, its rod-shaped counterpart (r- Co_3O_4) was observed to be much more stable, providing an enhanced cyclability (with a capacity of $\sim 800 \text{ mAh g}^{-1}$), whereas the capacity of p- Co_3O_4 decreased to $\sim 300 \text{ mAh g}^{-1}$ after 100 cycles (Figure 4.4d). In addition to cyclic stability, the kinetics of the conversion reaction of r- Co_3O_4 was superior to that of p- Co_3O_4 (Figure 4.4e and f). The plate-shaped cobalt oxide did not deliver a meaningful capacity at discharge rates faster than 2 C: p- Co_3O_4 showed a lower capacity of less than 100 mAh g^{-1} at 2 C, whereas the capacity of r- Co_3O_4 was $\sim 400 \text{ mAh g}^{-1}$. In terms of capacity recovery after rate-variable tests, the rod-shaped oxides were also favored, showing the same capacity at 0.1 C.

Difference in cyclability and rate capability is attributed to different architectures at higher levels in p- and r- Co_3O_4 as previously identified by microscopies and nitrogen sorption studies (also see Figure 4.5). During conversion reaction, gel-like polymers are formed around metal/ Li_2O nanoparticles. The insulating polymer layers could isolate the active mass from electric pathways if the oxide particles were not interconnected, and this phenomenon was observed in the present system of p- Co_3O_4 .¹⁰⁷ However, the interconnected network of the active mass in r- Co_3O_4 (pseudo-monolithic structure) prevents the isolation from electric pathways. The importance of pseudomonolithic integrity for stable and kinetically fast performances is supported by other works. The cyclability of nanoparticle metal oxides was inferior to that of its micro-sized counterparts.^{107, 108} Lu et al. showed that the electrochemical performances, especially cyclability, were improved as Co_3O_4 particles were monolithically integrated from a physical agglomerate to nano-clusters and macro-porous platelets.¹⁰³ In addition to the abovementioned reason in terms of the primary and secondary levels of morphology, there is every possibility that the spacing between stacked plates in p- Co_3O_4 (as the tertiary-level structure) provides a reaction surface on which the gel-like polymer layers are formed during lithiation. A macroscopic portion of plates located within the body of stacks could be isolated from electric pathways due to the development of insulating polymer films because the inner plates are not the pseudo-monolithic extension of exterior plates.

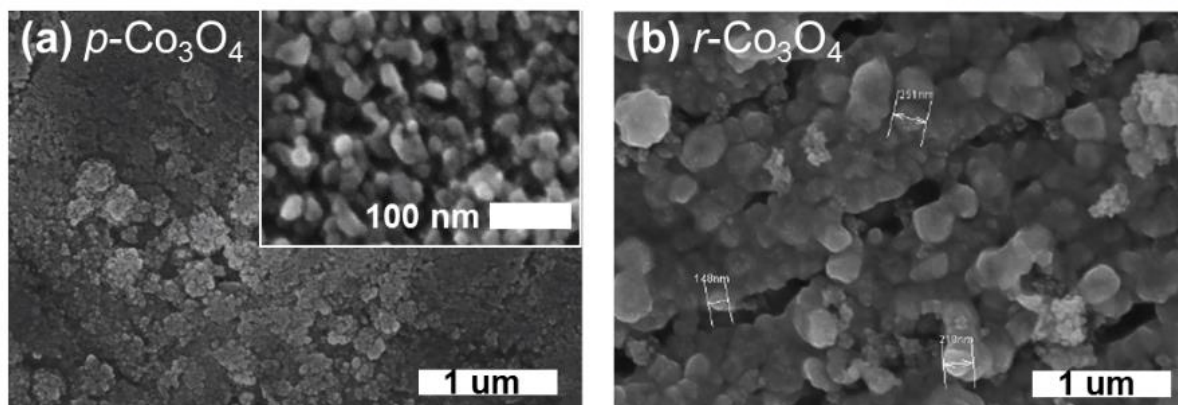


Figure 4.5. SEM images of composite electrodes containing (a) $p\text{-Co}_3\text{O}_4$ and (b) $r\text{-Co}_3\text{O}_4$. The interconnected secondary particles is clearly shown in (b) while the primary particles agglomerates without connectivity between them recognized in (a).

4.4 Conclusion

In conclusion, we successfully synthesized two kinds of Co_3O_4 nanomaterials through the pseudomorphic conversion of two Co-based MOFs, which are constructed with same building blocks. Both Co_3O_4 nanomaterials are composed of almost identical 10 nm-sized primary nanocrystals, each with its respective nanoporous secondary structures and macroscopic morphologies such as plate and rod shapes. These different higher level architectures of Co_3O_4 were utilized as an electrode in LIB, and their electrochemical properties were comparatively studied. It was revealed that the different cyclability and rate capability are attributed to their different microstructures. The present study can provide an idea of the development of electrode materials in LIBs from the viewpoint of higher level architectures.

Chapter 5. Enlarging the d-spacing of graphite and polarizing its surface charge for driving lithium ions fast

5.1 Introduction

Graphites have been dominantly used as an anode of lithium ion batteries (LIBs) due to their reversible structural change during lithiation and delithiation and low cost despite their relatively low capacity (theoretically, 372 mAh g⁻¹).¹⁰⁹ As LIB technologies develop, their application areas have been gradually extended from small mobile devices to large energy storage devices.¹¹⁰ Therefore, not only higher energy densities but also higher power densities are required. Though alloying-based or conversion-reaction-based compounds deliver higher capacities at slow charge or discharge rates than those of the intercalation-based graphites, they are significantly inferior to graphites in terms of kinetics.^{111, 112}

To increase the kinetics of lithiation/delithiation of graphites for guaranteeing high power densities, several approaches have been suggested. Park et al. controlled the peripheral d-spacing of graphite (d_o) by edge-selective functionalization, resulting in 190 mAh g⁻¹ at 50 C.¹¹³ Tossici et al. prepared KC₈-derived graphite of a larger interlayer distance (0.341 nm) due to potassium trespassing, which improved kinetics of the subsequent lithium intercalation.¹¹⁴

Graphite oxides and their derivatives such as graphene oxides, reduced graphene oxides and graphene sheets were used as anodes of LIBs.¹¹⁵⁻¹¹⁹ However, the enhancement of their capacities at low rates was focused. Also, the lithiation mechanism of the derivatives is not based on intercalation processes, which is electrochemically well-defined.^{117, 118} Enlarging the d-spacing into 0.6 to 0.7 nm by severe oxidation of graphites¹²⁰ does not result directly in kinetic improvement because the oxidation of graphites vastly decreases the electrical conductivity from 2500 S m⁻¹ for graphites to 0.021 S m⁻¹ for graphite oxides.¹²¹ That is to say, electron conduction decreases significantly even if ionic movement is enhanced through the widened ionic pathways. Not the lithium ion diffusion process but the electron conduction step determines the overall rates of intercalation.

In this work, we oxidized graphites in a mild (not severe) way to guarantee (1) expanding the d-spacing into the inter-graphitic distance at which the pi-pi stacking force is maintained and (2) keeping the electrical conductivity at a level of conductor without severe formation of defects to break the resonance structure of sp² hybrid configuration of graphitic planes. The resultant expanded graphites (EG*) and their thermally annealed version (EG) were characterized and compared with bare graphites by X-ray diffraction (XRD), X-ray photoelectron spectroscopy (XPS) and Raman spectroscopy. The delithiation kinetics of EG* and EG were proved to be superior to bare graphites under galvanostatic

stimulation conditions. Differential capacity analysis and in situ electrochemical impedance spectroscopy (EIS) revealed why the expanded graphites are excellent at high C-rates.

5.2 Experiments

5.2.1 Mild oxidation of graphite to EG* and subsequent thermal reduction of EG* to EG

EG* (* = functional groups) as an expanded and functionalized graphite was prepared from natural graphite powder (Aldrich) by the modified Hummers method.¹⁴ Graphite powder (1 g), potassium persulfate ($K_2S_2O_8$; 0.5 g) and phosphorus pentoxide (P_2O_5 ; 0.5 g) were mixed in sulfuric acid (H_2SO_4 ; 5 ml) with stirring until the reactants were dissolved. The mixture was kept in an oil bath at 80 °C for 4.5 h. After that, the mixture was diluted with DI water and stirred for about 5 min. Solid contents obtained after filtering and washing the mixture were transferred to a drying dish and left at room temperature overnight. Potassium permanganate ($KMnO_4$; 0.5 g) was slowly added as an oxidizing agent to H_2SO_4 (26 ml) containing the pretreated graphite in an ice bath. It should be noted that the amount of $KMnO_4$ used in this work is one-sixth of the amount used for synthesizing graphene oxide.¹²² The mixture was reacted at 35 °C for 2 h. After deionized water (46 ml) and 30% hydrogen peroxide (H_2O_2 ; 2.5 ml) were added, the resultant mixture was allowed to settle and the clear supernatant was decanted. 10% aqueous solution of HCl was added into the remaining mixture with stirring and then the mixture was filtered. The resulting solid was dried in air. The dried solid was added to deionized water. Solid contents were purified from the suspension through centrifugal dialysis. The collected precipitate was dried at 60 °C in oven. The resultant expanded graphite oxide (EG*) powder was thermally reduced in a furnace at 150 °C under an argon atmosphere. The ramping rate was fixed at 5 °C min⁻¹. EG* was re-graphitized to EG with fewer functional groups (indicated by * in EG*).

5.2.2 Characterization

Cold field emission scanning electron microscopy (FE-SEM; Hitachi, S-4800) was used to observe the morphology changes of natural graphite after mild oxidation and heat treatment. The crystallographic structures were studied using a high power X-ray diffractometer (XRD) and a Cu K α source (Rigaku, D/MAZX 2500V/PC). Functional groups of graphites were analysed by XPS (Thermo Fisher, K-alpha) and micro-Raman spectroscopy (WITec, alpha 300R). Carbon and oxygen contents were measured by elemental analysis based on the combustion method (LECO Co., TrueSpec Micro CHNS).

To characterize the electrochemical properties, CR2032 coin cells were assembled in an Ar-filled glove-box (less than 0.4 ppm of H_2O and 0.1 ppm of O_2). A mixture composed of active material (80 wt%), poly(vinylidene fluoride) (PVdF) (10 wt%) as a binder and Super P (10 wt%) as a conducting

agent were cast on Cu foil by using a doctor blade and then dried in a vacuum oven at 120 °C for 2 h. Lithium metal foil was used as a counter electrode while 1 M LiPF₆ dissolved in ethylene carbonate (EC)-diethyl carbonate (DEC) (1/1, vol%) was used as an electrolyte. Electrochemical performances were tested using a galvanostatic battery test system (WonA Tech) from 0.01 V to 1.5 V at different current rates (C-rates). Electrochemical impedance spectroscopy (EIS) was performed *in situ* during galvanostatic delithiation processes by synchronizing an applied current with sinusoidal current signals using a 300 mA sinus amplitude in the frequency range from 50 kHz to 10 Hz. The impedance data were recorded every 10 min during delithiation at 0.1C.

5.3 Results and discussion

Morphological changes at a sub-micrometer dimensional level were observed upon the mild oxidation and the subsequent thermal reduction (Figure 5.1). The bare graphite formed closely packed secondary particles of graphitic sheets with >15 μm size. The secondary particles consisted of flake-like primary particles. After the mild oxidation, however, the graphitic flakes were partly exfoliated in EG*. There were no significant differences observed after the subsequent thermal reduction from EG* to EG.

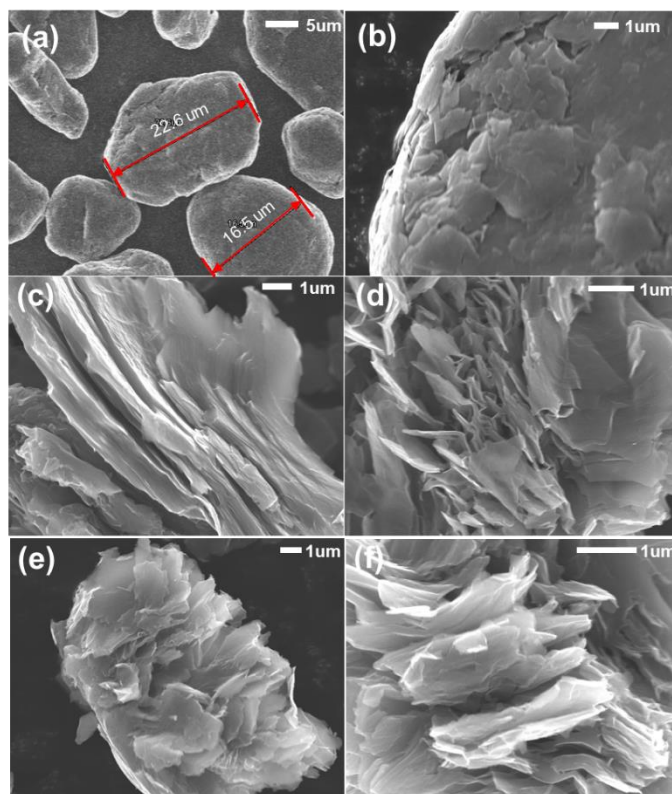


Figure 5.1. Morphological characterization. SEM images of bare graphites (a and b), EG* (c and d) and EG (e and f).

The degree of expansion between graphitic sheets was evaluated by XRD (Figure 5.2). A main peak of bare graphite detected at 26.5° along the (002) plane was very sharp, indicating that the graphite had a large domain size of crystallites with regular distance between graphitic sheets. After the mild oxidation (EG*), the (002) peak was shifted to the lower angle and broadened. Functional groups (discussed below with Figure 5.3) generated by the oxidizing agent at the edges or on the planes of graphites extend the distance between graphitic sheets irregularly.¹¹³ The representative d-spacing estimated at the (002) peak by the Bragg equation was changed from 0.3359 nm for the bare graphite to 0.3395 nm for EG*. The d-spacing distribution is responsible for the broadness of the (002) peak of EG* and the shoulder in its left between 20° and 25° . The domain size of the crystallites was accordingly reduced to half. After the subsequent thermal reduction, the 2θ location and broadness of the (002) peak and its left shoulder were not significantly changed. Only the crystallographic difference between EG* and EG was the relative portion of the shoulder to the (002) peak: the portion of larger d-spacing was discouraged by the thermal treatment at 150°C as graphitization proceeded.

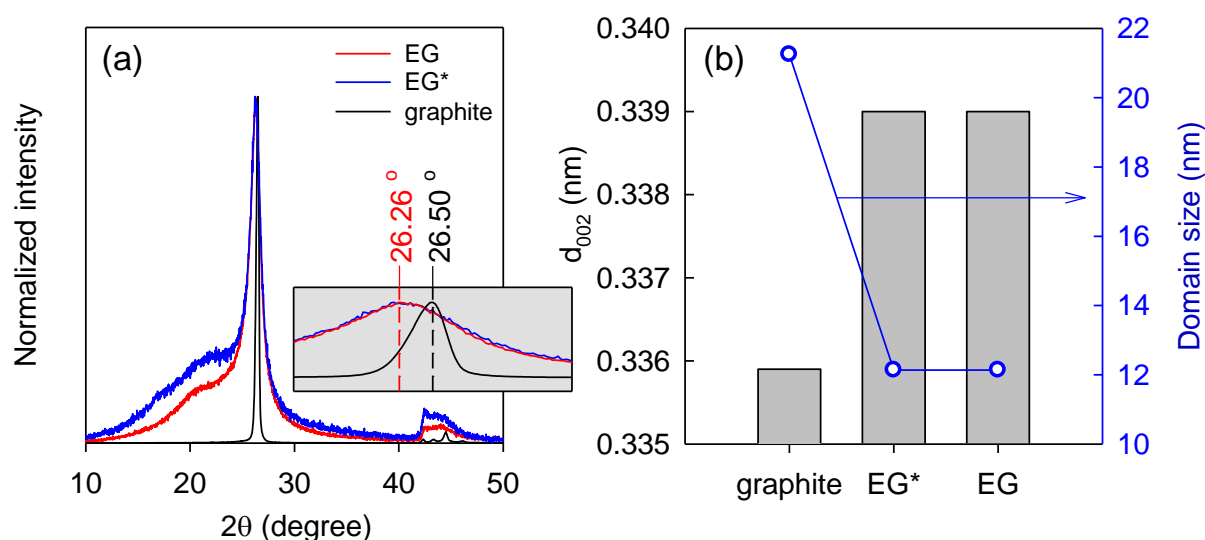


Figure 5.2. Crystallographic characterization. (a) X-ray diffraction patterns. The intensities were normalized by that of the (002) peak of the corresponding material. (b) Comparison of d-spacing values and domain sizes. The values were calculated from the 2θ location and full width at half maximum of the (002) peak by using Bragg's law and Scherrer equation, respectively.

Development of functional groups during the mild oxidation was clearly observed in C1s photoemission spectra (Figure 5.3a and b and Table 5.1). A portion of double bonds between carbons in the sp^2 hybrid configuration of graphite is oxidized into oxygencontaining functional groups (indicated by the increases of C-O and COOH), leaving single bonds between carbons indicating the sp^3

configuration (indicated by the decrease in C=C and the increase in C-C). Formation of the functional groups is thought to be the main driving force to expand the distance between graphitic layers in graphite.^{113, 123, 124} The chemical exfoliation of graphite into graphene oxide, achieved by severe oxidation, is the extreme case in which a large number of functional groups tethered to graphitic layers exhibits repulsive forces between the layers. In our mild oxidation, however, the layered structure of bare graphite was maintained macroscopically only with interlayer distance changing. After the subsequent thermal reduction (Figure 5.3b and c and Table 1), the C=C bonds between carbons indicating the sp^2 hybrid configuration were partially recovered while C-C bonds as well as other functional groups were slightly decreased. Elemental analysis based on a combustion method supported the reduction of functional groups during the thermal reduction: O/C molar ratio = 0.094 (EG*) versus 0.065 (EG).

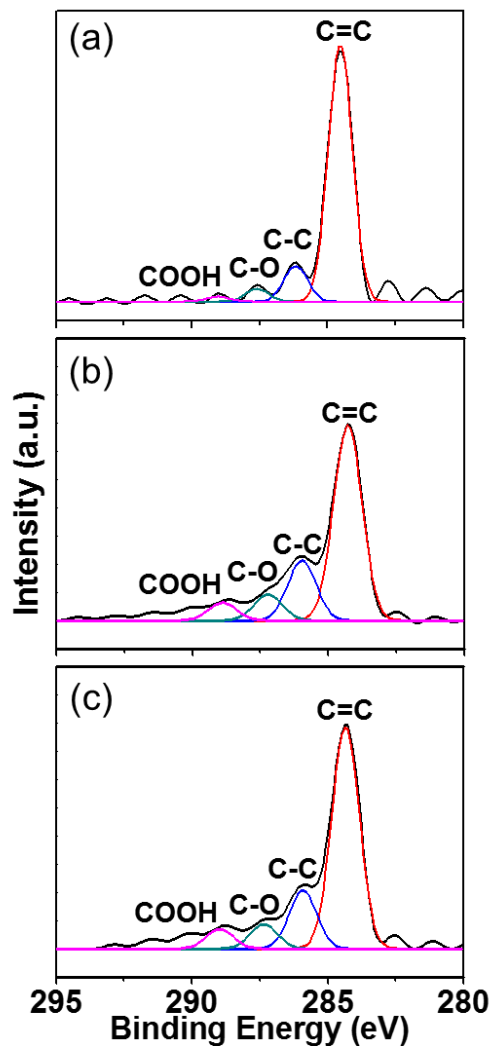


Figure 5.3. C1s photoemission spectra of graphite (a), EG* (b) and EG (c).

Table 5.1. Compositions of chemical bonds relevant to carbon estimated from C1s photoemission spectra in Figure 5.3.

		C=C	C-C	C-O	COOH
graphite	Position(eV)	284.5	268.1	287.6	289.0
	Area(%)	82.7	11.6	4.1	1.6
EG*	Position(eV)	284.3	286.0	287.2	288.9
	Area(%)	65.2	20.4	8.6	5.8
EG	Position(eV)	284.4	286.0	287.4	288.9
	Area(%)	68.5	18.0	7.5	6.0

Raman spectroscopy was used to investigate the structural transformation in terms of the degree of graphitization (Figure 5.4). An additional D band (disorder band) appeared in EG* and EG while only a sharp peak of the G band (graphite band) was observed in the bare graphite. The mild oxidation caused disorder by forming defects from the breakage of sp^2 configuration and formation of functional groups as detected in the XPS study. Also, the G band was broadened and blue-shifted to higher wavenumber in EG* (Figure 5.4) as the amorphization by oxidation proceeds. The broadening of the G band results from vibrational states dispersed by bond-bending disorder or softening of non-six-fold rings.¹²⁵ There are several suggested explanations for the blue shift. When defects are developed in graphite, a new band called D' appears at $\sim 1620\text{ cm}^{-1}$ and merged with the existing G band.¹²⁶ Also, the G band is blue-shifted from 1581 cm^{-1} to 1585 cm^{-1} when the attractive forces between graphitic layers are weakened.¹²⁷ After the subsequent thermal reduction, the intensity of the G band of EG increased compared with that of EG* (Figure 5.4c), implying that the degree of graphitization was partially redeemed.

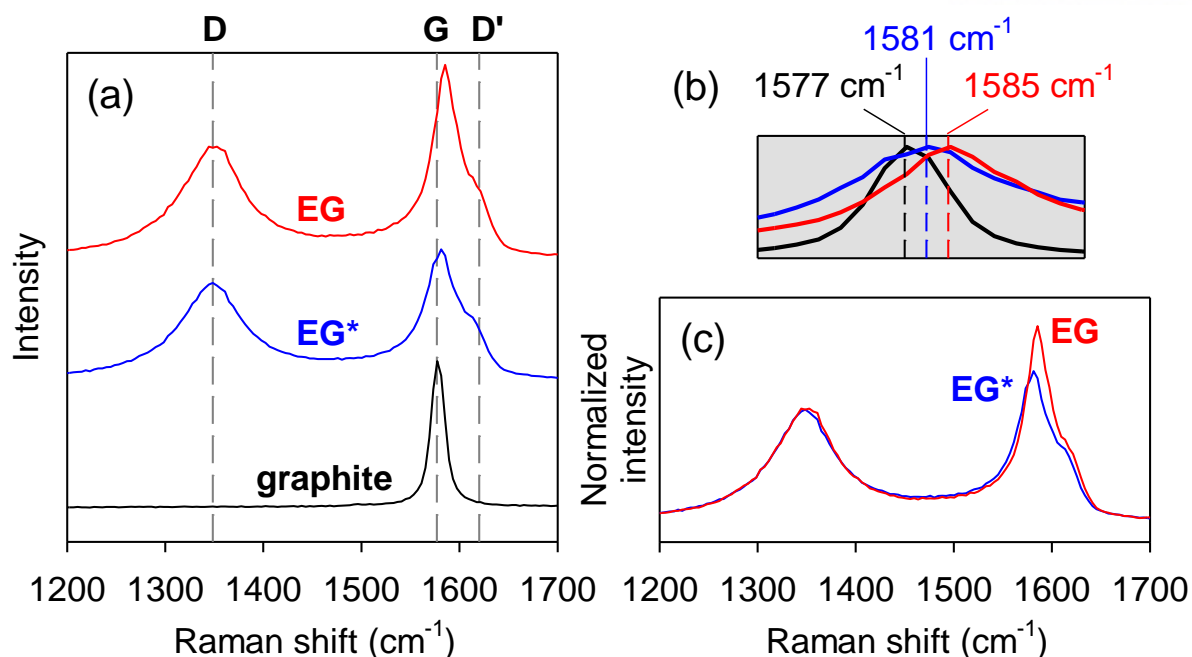


Figure 5.4. Characterization of graphitization by Raman spectra. (a) Raw data. Three different bands (G, D and D') were indicated by dashed lines. (b) Comparison of Raman shifts at peaks of the G band. The same colors of the corresponding samples were used in (a). (c) Comparison between EG* and EG by normalizing intensities by that of the D band.

Based on the d-spacing expansion by the mild oxidation and the redeemed graphitization by the subsequent thermal reduction, enhancement of lithium ion movement within interlayer channels is expected. To confirm and prove the improved kinetics, electrochemical performances were evaluated at different current rates (Figure 5.5). During delithiation at 0.1 C, the expanded graphites (EG and EG*) exhibited capacities at 290 and 183 mAh g⁻¹ respectively lower than that of graphite at 365 mAh g⁻¹ near the theoretical capacity of graphite. No significant decrease of capacity from the value at 0.1 C ($Q_{0.1C}$) was observed until 10 C for all samples. The capacities of EG and EG* were maintained close to their $Q_{0.1C}$ (90% and 85% at 30 C) even after 30 C while that of bare graphite rapidly decreased to 68% of its $Q_{0.1C}$ at 30 C. The gap of relative % capacities between the expanded and bare graphites was more intensified as the delithiation rates reached up to 50 C: 84% for EG and 77% for EG* versus 18% for the bare graphite. Even in terms of the capacity values in mAh g⁻¹, EG* and EG overcame their demerits of low initial capacities from 30 C and 40 C respectively.

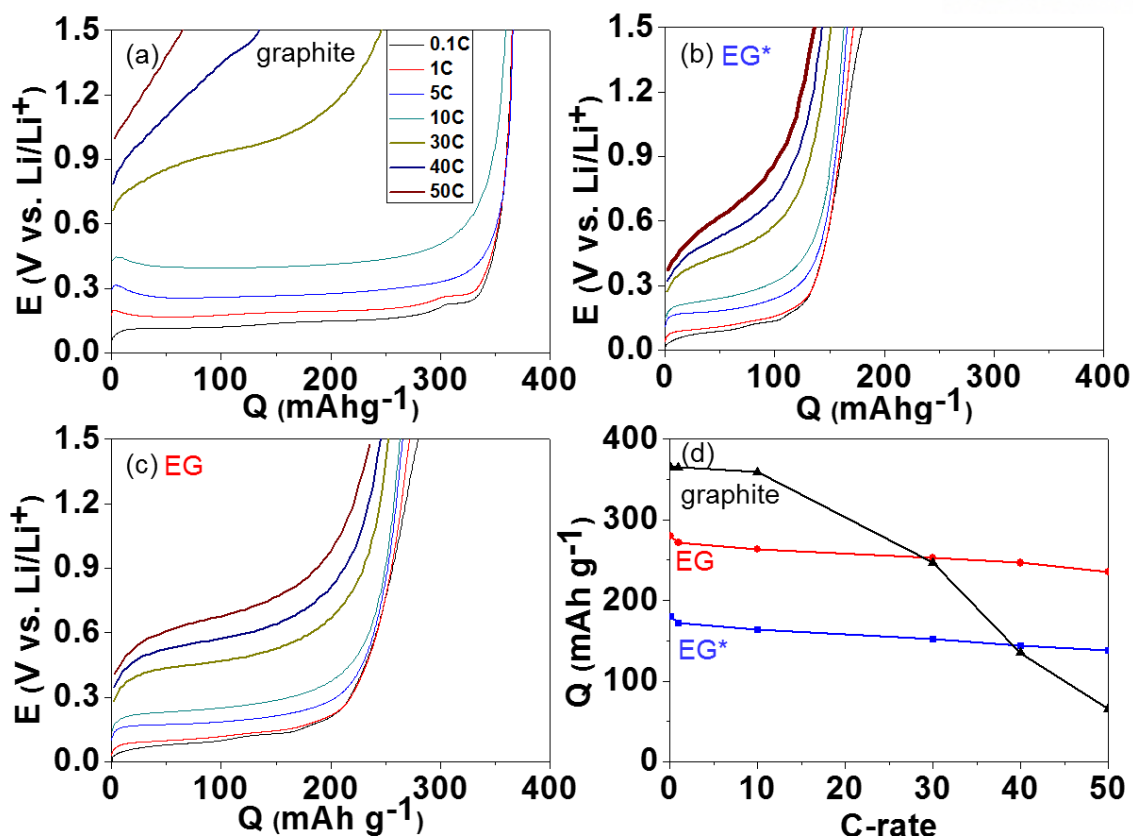


Figure 5.5. Galvanostatic delithiation at different current rates. (a to c) Potential profiles of the bare graphite (a), EG* (b) and EG (c). (d) C-rate dependency of capacities.

The available capacity (assumed to be $Q_{0.1C}$) of the expanded graphites inferior to that of the bare graphite can be explained by several reasons. Functional groups on the basal planes and more dominantly at the edges of graphitic layers trap lithium ions, resulting in larger irreversible capacities.¹²⁸ Also, more amount of solid-electrolyte interface (SEI) films are formed due to the electrochemical activity of surface defects of graphitic sheets and the larger surface area of expanded structures, leading to irreversible lithium ion storage.¹²⁹ The integrated area of EG in its differential capacity curve, which is proportional to the amount of SEI layer formation, was estimated to be ten times larger than that of bare graphite (Figure 5.6). The sp^3 carbon configuration is considered as another possible reason. The bare graphite is composed of sp^2 carbons which fully contribute to the capacity. However, both EG* and EG contain not only sp^2 carbons but also sp^3 carbons that may not generate the LiC_6 complex during lithiation.

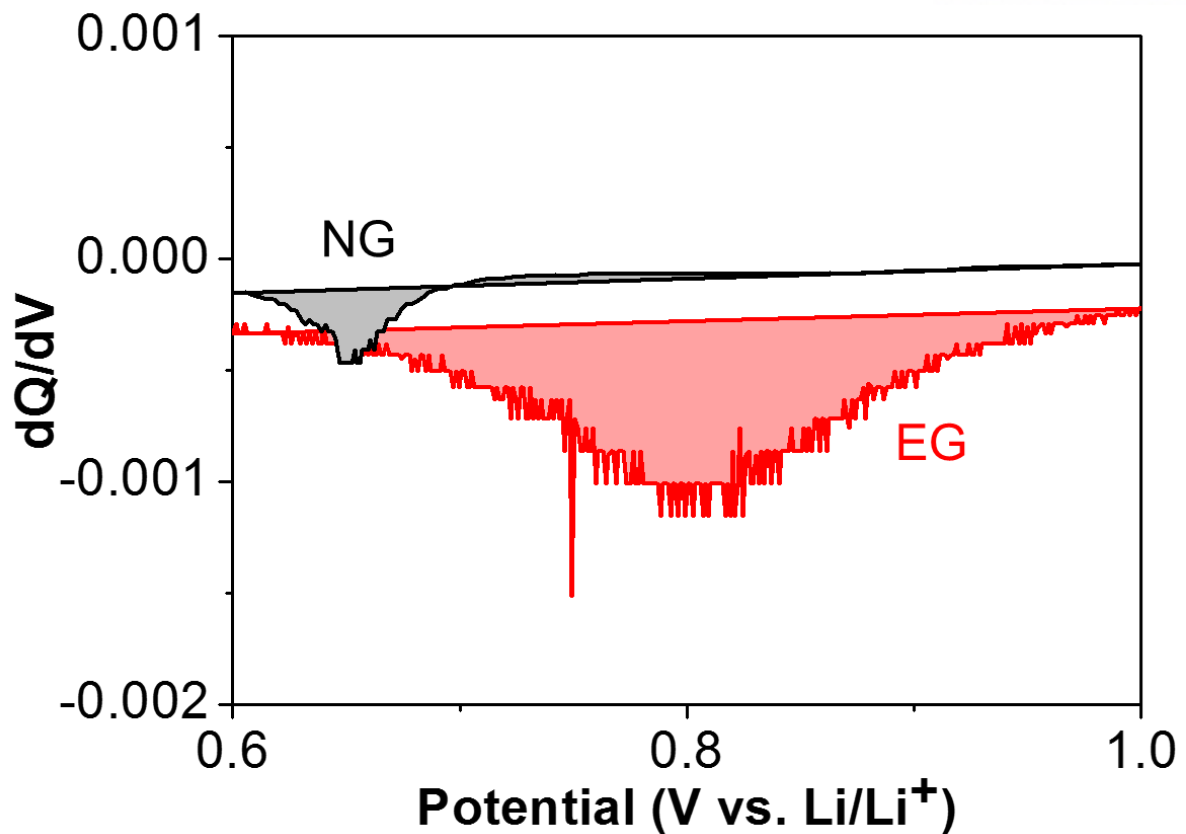


Figure 5.6. Differential capacity (dQ/dV) curves of bare graphite and EG during the 1st lithiation. Integrated areas are directly related to the amounts of SEI layer.

From the kinetic viewpoint, however, it is clear that lithium ion movement in the expanded graphites was faster than that in the bare graphite. Four reasons can be provided. Both EG* and EG have wider channels through which lithium ions travel, which is indicated by the d-spacing increase after the mild oxidation. Smaller domain size of graphitized crystallites is also a helpful factor by shortening the ionic diffusion length. Thinner SEI layers of EG* and EG than that of bare graphite facilitate lithium ion transport. The thickness of the SEI layer was characterized by depth profiles of X-ray photoelectron spectroscopy (XPS) and time-of-flight secondary ion mass spectrometry (TOF-SIMS). A dramatic increase of the atomic concentration of carbon is detected at the interface between the SEI layer and graphite. The intensity of the carbon-related XPS peak of EG* and EG gradually increased after 10 min sputtering (Figure 5.7). In contrast, no significant change in the peak was observed with bare graphite even after 30 min sputtering. It implies that the SEI layer of bare graphite is much thicker than EG* and EG. The depth profile of TOF-SIMS more clearly supports development of the thinner SEI layer of EG* and EG (Figure 5.8). The concentration of carbon was saturated after 300 s in bare graphite while saturated earlier in EG* and EG. It should be noted that the larger amount of the SEI layer of the

expanded graphites is not contradictory to the thinner SEI layer development on the same materials because EG* and EG provide higher surface areas exposed to the electrolyte than bare graphite. The fourth reason is based on the polarized-charge dispersion model suggested by Wang et al.¹³⁰ By our mild oxidation, the C-C bonds (therefore, C-H bonds) and other functional groups containing C-OH and COOH were developed. The hydrogen-containing bonds in functional groups are polarized through the electrostatic interactions or hydrogen bonding between the hydrogen atoms belonging to graphites and highly electronegative oxygen atoms of carbonate solvent molecules in the electrolyte. Consequently, partially induced negativity of carbons in graphite reduces the energy barrier of lithium ion intercalation.

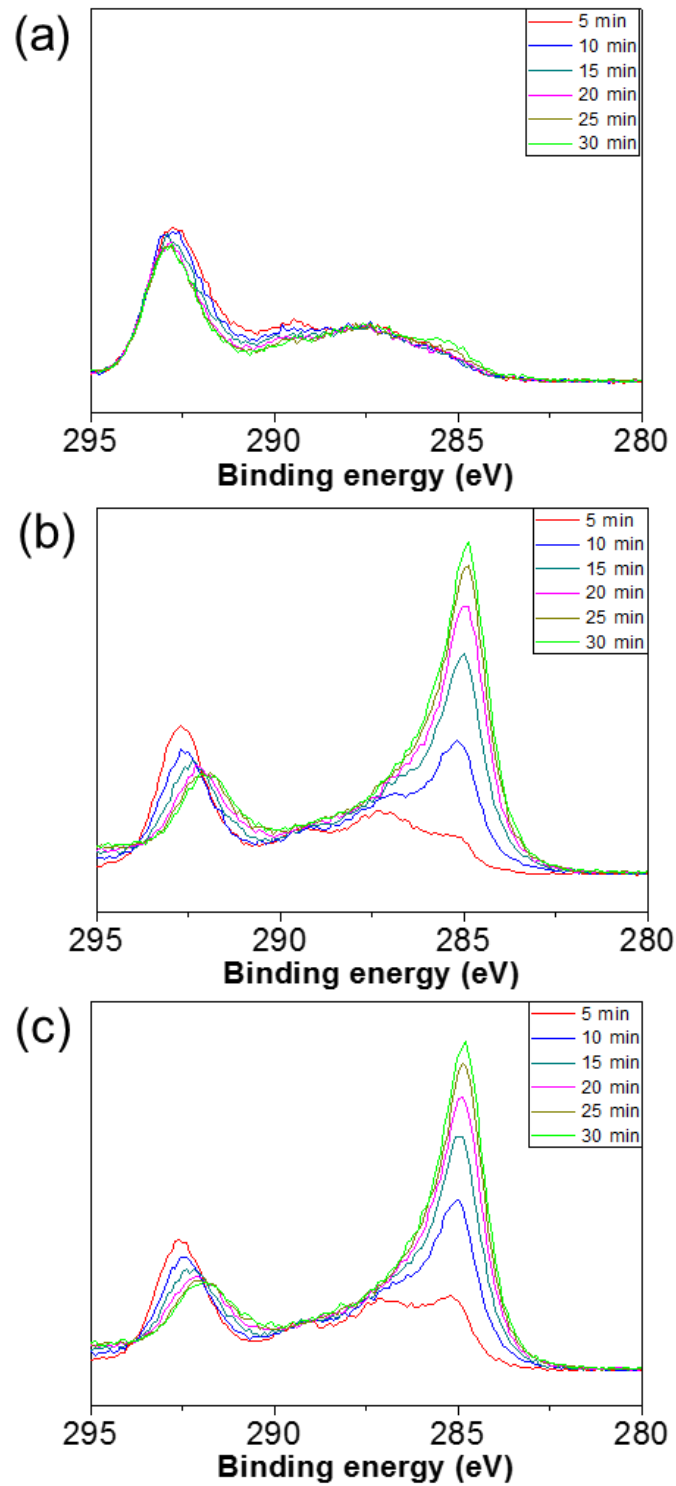


Figure 5.7. XPS depth profiles of C1s spectra of (a) bare graphite, (b) EG* and (c) EG. There were no significant changes of peak at 285 eV with NG. However, the peaks of EG* and EG increased with time.

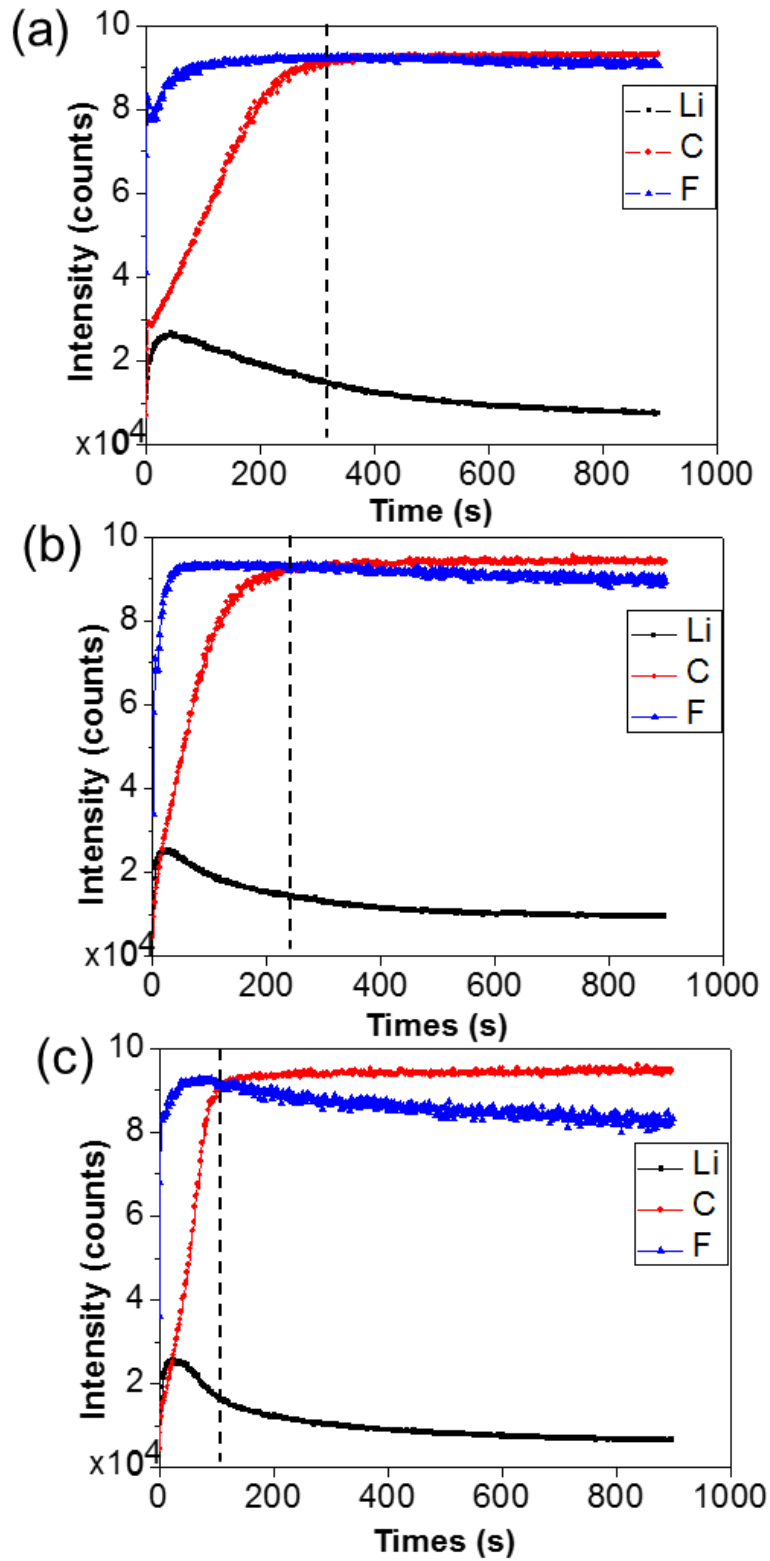


Figure 5.8. TOF-SIMS depth profiles of (a) bare graphite, (b) EG* and (c) EG.

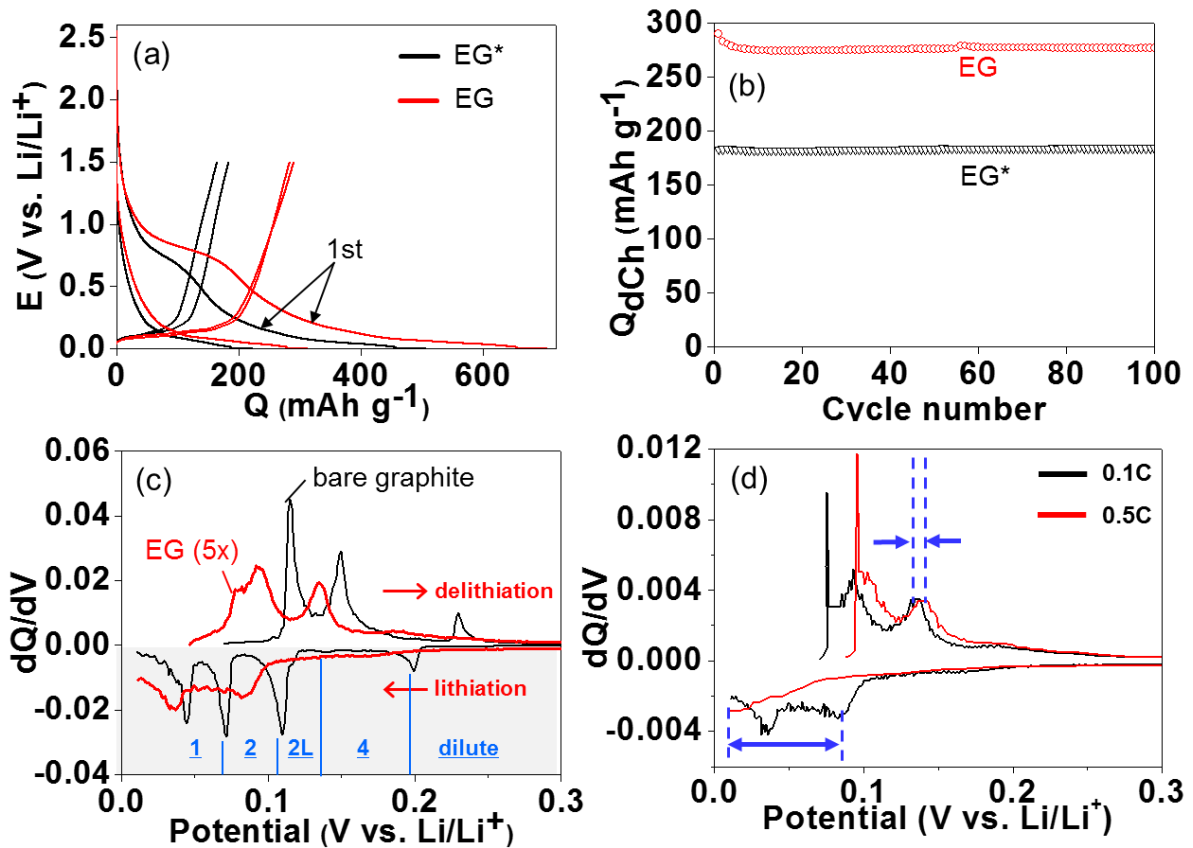


Figure 5.9. (a) Potential profiles of EG* and EG at the first and second cycles during lithiation at 0.1 C and delithiation at 0.1 C. (b) Capacity retention of EG* and EG along cycles consisting of lithiation at 0.1 C followed by delithiation at 0.1 C. (c) Differential capacity curves of the bare graphite and EG at the second cycle. The red arrows indicate the potential scan directions. Stages were indicated in blue. (d) Differential capacity curves of EG at 0.1 C and 0.5 C. The gaps between blue dotted lines mean the overpotential.

Figure 5.9a shows potential profiles of EG* and EG at the first and the second cycle. At the first cycle, the expanded graphites showed profiles similar to hydrogen-containing carbon materials.¹³¹ The plateau around 0.8 V during lithiation is related to the SEI layer formation due to decomposition of EC in the electrolyte.¹³² Once the SEI layer was formed at the first lithiation process, the plateau at 0.8 V was not observed during the second lithiation. Below 0.8 V, lithium ions are stored on or in graphites based on two different mechanisms. First, lithium ions are stored in the surface defects of EG* and EG. A portion of lithium ions are consumed at this process, resulting in irreversibility.^{118, 129} Second, lithium ions are inserted or intercalated between graphitic layers. After the first lithiation, the reversibility of

lithiation/delithiation was guaranteed with EG* and EG (Figure 5.9b). The capacity of both EG* and EG was maintained up to higher than 95% of the capacity at the first cycle even after 100 cycles.

Lithiation of the bare graphite proceeds stage by stage (Figure 5.9c).²³ Lithium ions are inserted into the empty interspacing layers where the energy barriers of intercalation are minimized. If all interspacing layers were identically defined, lithium ions would be intercalated in a way that minimizes the interaction between Li⁺-filled layers. Therefore, Li⁺-filled layers are periodically generated. Subsequently, lithium ions seek the layers for intercalation far away from the layers at which lithium ions are already filled. The periodicities of the filled layer determine the stages: e.g. stage 4 means lithium ions were intercalated every four layers (numbers in blue in Figure 5.9c). Each stage transition is identified by its own electrochemical potential that is distinguished from the other stage transition (blue vertical lines). The stage behavior of the bare graphite was clearly observed in the differential capacity (dQ/dV) curve (Figure 5.9c).

However, lithiation/delithiation behavior of EG was deviated from the well-defined staging behavior. The plateau potentials were not clearly defined so that the peaks responsible for the stage transitions in the dQ/dV curve were broadened. The peak broadness originates from the d-spacing distribution as well as the irregular structure of EG compared with the bare graphite. Also, the potentials at which stages are changed were shifted to the negative direction of potential. During lithiation, lithium species move sluggishly inside EG due to slow electron supply caused by its lower electric conductivity even if the wider d-spacing of EG facilitates the insertion of lithium ions through the entrance of graphites. Lithium ions are stuck nearby the edge region, resulting in an intercalation potential shift to the negative direction (more overpotential). During delithiation, in contrast, lithium ions can be deintercalated in an easier way through the wider d-spacing gate, opening the pathway for their slow followers. Therefore, the deintercalation potential of EG is still more negative (less overpotential) compared with that of bare graphite. Figure 5.9d strongly supports the asymmetric overpotential of EG between lithiation and delithiation by comparing differential capacity curves between two different Crates. At a higher C-rate (0.5 C) with respect to a lower C-rate (0.1 C), a larger overpotential (more than 100 mV) indicated by the negative shift of the first lithiation potential was observed during lithiation while only a small overpotential (~10 mV) was investigated during delithiation. The C-rate dependency of the lithiation processes also confirmed the asymmetric behavior of overpotential of EG (Figure 5.10). The serious decrease of lithiation capacity is contrasted with a relatively insignificant change in delithiation capacity (Figure 5.5d).

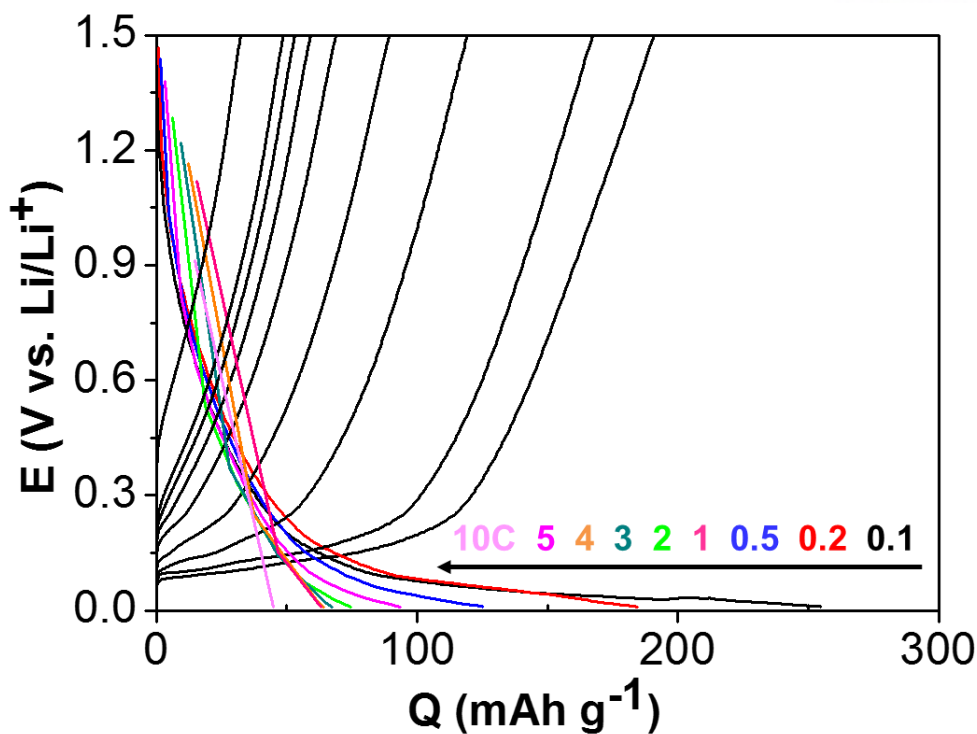


Figure 5.10. Galvanostatic lithiation of EG at different C-rates with a fixed current (0.1C) during delithiation.

Electrochemical impedance spectra (EIS) were measured in situ every 10 min during delithiation at 0.1 C (Figure 5.11). The size of semicircles of both EG and bare graphite gradually decreased as delithiation progressed. The depressed semicircles in the Nyquist plot result from overlapping of charge transfer processes at the two different interfaces in electrolyte|SEI layer| graphite systems. At the initial period of delithiation (SOC = 100%), EG fully utilized its kinetic advantage caused by wider channels. Smaller resistance (size of the semicircle) was involved with EG at the first time (as soon as delithiation began) when compared with that of the bare graphite. As delithiation proceeds, the effects of larger d-spacing of the expanded graphites on kinetics decrease. From 95% of state of charge (SOC), the sizes of semicircles were reversed between EG and the bare graphite. That is to say, the bare graphite became kinetically superior to EG after the critical state of charge (SOC) at the latter part of delithiation. The discussion also explains why the expanded graphites (EG* or EG) are superior to the bare graphite especially at very high rates such as 50 C. It should be noted that the resistances estimated from the diameter of semicircles are the function of C-rates when impedance spectra are measured in situ during galvanostatic delithiation or lithiation (our preliminary experiments). The effective resistances estimated from the diameter of semicircles are expected to be smaller with EG than bare graphite in the

SOC range of full delithiation at 30 C to 50 C even if it is difficult to measure them due to instrumentation limits (impedance spectra cannot be measured in situ within the time period (72 s) of full delithiation at 50 C). At the high rates, only the SOC range favorable to EG could be utilized without using the latter part of delithiation in which EG is inferior to the bare graphite.

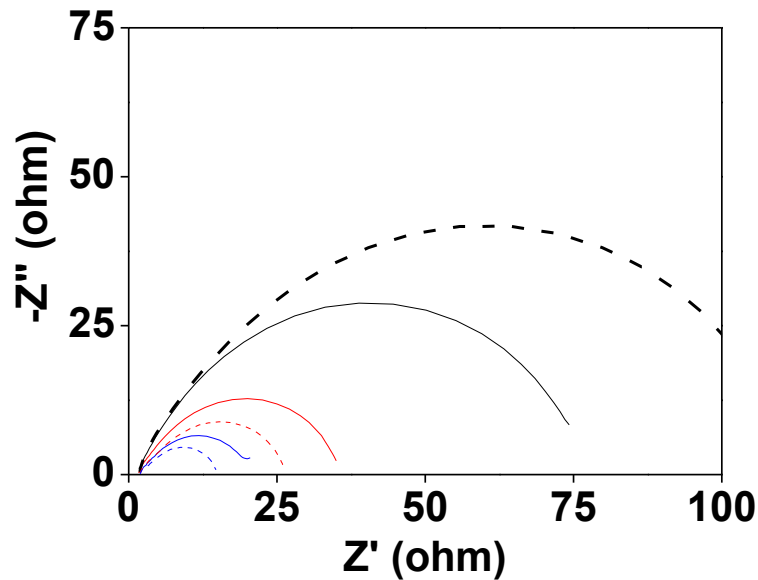


Figure 5.11. Electrochemical impedance spectra of the bare graphite (dotted lines) and EG (solid lines) measured in situ during galvanostatic delithiation at 0.1 C.

5.4 Conclusion

In this work, the effects of d-spacing and functional groups on electrochemical performances of graphite were investigated. The d-spacing between graphitic layers was controlled by oxidizing graphite in a mild degree at which the p-p stacking was maintained without exfoliation. In the subsequent thermal reduction, the degree of graphitization was partially redeemed. Simultaneously, oxygen-containing functional groups were generated at edges or planes of graphite in the first oxidation step and then removed by the second reduction step. The expanded graphites (EG* and EG) were lithiated/delithiated via intercalation/de-intercalation basically like graphite, which is distinguished from the adsorption mechanism shown in graphite oxide or graphene oxide. They exhibited enhanced capacities especially at fast rates over 30 C when compared with the original graphite. The larger d-spacing facilitated lithium ion movement between graphitic layers. Also, functional groups at the edges of graphite induced polarization of charge, decreasing activation energy required to extract lithium ions from graphite. We believe that modification of graphite opens a new possibility of old-fashioned but still dominantly used graphite anodes especially at high-rate applications. Even in the cases of silicon-

graphite composites for higher capacities, high current cannot be extracted from silicon as a high-energy component. Only the modified graphites such as EG* and EG shown in this work would cover the high-rate performances.

Chapter 6. Summary

Li ions diffusion and electron conduction are very important factors for better performance of LIBs. To enhance the ionic conductivities, I have designed the morphologies of electroactive materials. Although LMP has many advantages such as high working potential around 4.1 V, stable structure due to strong covalent bonding between O^{2-} and P^{5+} , and low cost due to Mn ions, poor ionic and electronic conductivities made many researchers hesitate to drive LMP as an alternative cathode. The ionic conductivity of LMP was improved due to shorter diffusion length of nanoparticles synthesized by sequential precipitation method using the difference of solubility product. The LMP nanoparticles prepared by sequential precipitation was one-third size of a LMP by co-precipitation method, leading to good performances at high current rates. In addition, carbon coating shell helped electrons moving faster. Magnetite (Fe_3O_4) is attractive anode material based on conversion reaction due to 3 fold-larger capacity than natural graphite. Hollow sphere nanostructure enabled Li ions to diffuse onto electrode surface, resulting in good rate capabilities. Inner void provided space for volume expansion not to be pulverized and electrically isolated. Carbon shell also suppressed volume expansion and gave better electron conduction. Two different morphology of Co_3O_4 were investigated in a micro-scale level. Both Co_3O_4 were composed of 10 nm primary particles but with different nanoporous secondary structures and macroscopic architectures such as plate and rod shapes. Rod- Co_3O_4 showed better cyclability and rate capability than plate- Co_3O_4 . This was caused by the interconnection between primary nanoparticles. Rod- Co_3O_4 nanoparticles were inter-connected by each other, so polymeric film inevitably formed onto the surface of electrode during lithiation did not hinder electron pathway, while plate- Co_3O_4 nanoparticles independently existed were isolated by insulating polymeric film. In addition, inner plate- Co_3O_4 were isolated from electric pathways. It demonstrated that hierarchical architecture with inter-connected nanoparticles are good solution due to shorter diffusion length and good electric pathway.

On the other hand, I modified Li ions diffusion resistance by expanding d-spacing distance between graphitic layers. Larger distance reduced the diffusion resistance, accelerating lithium ions diffusion within graphitic layers. In addition, the activation energy of Li ion solid-state diffusion was reduced by polarized charge effect induced by hydrogen bonding between oxygen atoms of carbonated in organic electrolytes and hydrogen atoms of edge functional groups.

Chapter 7. References

1. Mizushima, K.; Jones, P.; Wiseman, P.; Goodenough, J. B. Li_xCoO_2 ($0 < x < 1$): A new cathode material for batteries of high energy density. *Mater. Res. Bull.* **1980**, *15*, 783-789.
2. Buchmann, I. What's the Best Battery? http://batteryuniversity.com/learn/article/whats_the_best_battery
3. Abbas A. Akhil; Georgianne Huff; Aileen B. Currier; Benjamin C. Kaun; Dan M. Rastler; Stella Bingqing Chen; Andrew L. Cotter; Dale T. Bradshaw; Gauntlett, W. D. *EOD/EPRI 2013 Electricity Storage Handbook in Collaboration with NRECA*; July 2013.
4. Ozawa, K. In *Lithium Ion Rechargeable Batteries: Materials, Technology, and New Applications*; Eds.; Wiley: 2009; pp 13.
5. Huggins, R. Materials Science Aspects. In *Advanced Batteries*; Eds.; Springer: 2008; pp 162.
6. Cho, J.; Kim, C. S.; Yoo, S. I. Improvement of Structural Stability of LiCoO_2 Cathode during Electrochemical Cycling by Sol-Gel Coating of SnO_2 . *Electrochem. Solid-State Lett.* **2000**, *3*, 362-365.
7. Cho, J.; Kim, Y. J.; Kim, T. J.; Park, B. Zero-strain intercalation cathode for rechargeable Li-Ion cell. *Angew. Chem.* **2001**, *113*, 3471-3473.
8. Wang, Y.; Wang, Y.; Hosono, E.; Wang, K.; Zhou, H. The design of a LiFePO_4 /carbon nanocomposite with a core-shell structure and its synthesis by an in situ polymerization restriction method. *Angew. Chem. Int. Ed.* **2008**, *47*, 7461-7465.
9. Kang, B.; Ceder, G. Battery materials for ultrafast charging and discharging. *Nature.* **2009**, *458*, 190-193.
10. Kavan, L.; Rathouský, J.; Grätzel, M.; Shklover, V.; Zukal, A. Surfactant-templated TiO_2 (anatase): Characteristic features of lithium insertion electrochemistry in organized nanostructures. *J. Phys. Chem. B.* **2000**, *104*, 12012-12020.
11. Chen, C.; Vaughey, J.; Jansen, A.; Dees, D.; Kahaian, A.; Goacher, T.; Thackeray, M. Studies of Mg-Substituted $\text{Li}_{4-x}\text{Mg}_x\text{Ti}_5\text{O}_{12}$ Spinel Electrodes ($0 \leq x \leq 1$) for Lithium Batteries. *J. Electrochem. Soc.* **2001**, *148*, A102-A104.
12. Levi, M.; Levi, E.; Aurbach, D. The mechanism of lithium intercalation in graphite film electrodes in aprotic media. Part 2. Potentiostatic intermittent titration and in situ XRD studies of the solid-state ionic diffusion. *J. Electroanal. Chem.* **1997**, *421*, 89-97.
13. Vu, A.; Qian, Y.; Stein, A. Porous Electrode Materials for Lithium-Ion Batteries—How to Prepare Them and What Makes Them Special. *Adv. Energy Mater.* **2012**, *2*, 1056-1085.
14. Das, S. K.; Darmakolla, S.; Bhattacharyya, A. J. High lithium storage in micrometre sized mesoporous spherical self-assembly of anatase titania nanospheres and carbon. *J. Mater. Chem.* **2010**,

20, 1600-1606.

15. Wang, D.; Choi, D.; Yang, Z.; Viswanathan, V. V.; Nie, Z.; Wang, C.; Song, Y.; Zhang, J.-G.; Liu, J. Synthesis and Li-ion insertion properties of highly crystalline mesoporous rutile TiO₂. *Chem. Mater.* **2008**, *20*, 3435-3442.

16. Lim, S.; Yoon, C. S.; Cho, J. Synthesis of nanowire and hollow LiFePO₄ cathodes for high-performance lithium batteries. *Chem. Mater.* **2008**, *20*, 4560-4564.

17. Jiao, F.; Bao, J.; Hill, A. H.; Bruce, P. G. Synthesis of ordered mesoporous Li-Mn-O spinel as a positive electrode for rechargeable lithium batteries. *Angew. Chem. Int. Ed.* **2008**, *47*, 9711-9716.

18. Wang, G.; Liu, H.; Horvat, J.; Wang, B.; Qiao, S.; Park, J.; Ahn, H. Highly ordered mesoporous cobalt oxide nanostructures: synthesis, characterisation, magnetic properties, and applications for electrochemical energy devices. *Chemistry-A European Journal.* **2010**, *16*, 11020-11027.

19. Kim, H.; Cho, J. Hard templating synthesis of mesoporous and nanowire SnO₂ lithium battery anode materials. *J. Mater. Chem.* **2008**, *18*, 771-775.

20. He, M.; Kravchyk, K.; Walter, M.; Kovalenko, M. V. Monodisperse Antimony nanocrystals for high-rate Li-ion and Na-ion battery anodes: nano versus bulk. *Nano Lett.* **2014**, *14*, 1255-1262.

21. Zhu, C.; Yu, Y.; Gu, L.; Weichert, K.; Maier, J. Electrospinning of Highly Electroactive Carbon-Coated Single-Crystalline LiFePO₄ Nanowires. *Angew. Chem. Int. Ed.* **2011**, *50*, 6278-6282.

22. Chan, C. K.; Peng, H.; Liu, G.; McIlwrath, K.; Zhang, X. F.; Huggins, R. A.; Cui, Y. High-performance lithium battery anodes using silicon nanowires. *Nature nanotechnology.* **2008**, *3*, 31-35.

23. Chan, C. K.; Zhang, X. F.; Cui, Y. High capacity Li ion battery anodes using Ge nanowires. *Nano Lett.* **2008**, *8*, 307-309.

24. Kim, H.; Seo, M.; Park, M. H.; Cho, J. A Critical Size of Silicon Nano-Anodes for Lithium Rechargeable Batteries. *Angew. Chem. Int. Ed.* **2010**, *49*, 2146-2149.

25. Son, Y.; Park, M.; Son, Y.; Lee, J.-S.; Jang, J.-H.; Kim, Y.; Cho, J. Quantum confinement and its related effects on the critical size of GeO₂ nanoparticles anodes for lithium batteries. *Nano Lett.* **2014**, *14*, 1005-1010.

26. Liu, H.; Cao, Q.; Fu, L. J.; Li, C.; Wu, Y.; Wu, H. Doping effects of zinc on LiFePO₄ cathode material for lithium ion batteries. *Electrochem. Commun.* **2006**, *8*, 1553-1557.

27. Veluchamy, A.; Ikuta, H.; Wakihara, M. Boron-substituted manganese spinel oxide cathode for lithium ion battery. *Solid State Ionics.* **2001**, *143*, 161-171.

28. Carewska, M.; Scaccia, S.; Croce, F.; Arumugam, S.; Wang, Y.; Greenbaum, S. Electrical conductivity and ^{6,7}Li NMR studies of Li_{1+y}CoO₂. *Solid State Ionics.* **1997**, *93*, 227-237.

29. Julien, C.; Camacho-Lopez, M.; Mohan, T.; Chitra, S.; Kalyani, P.; Gopukumar, S. Combustion synthesis and characterization of substituted lithium cobalt oxides in lithium batteries. *Solid State Ionics.*

2000, 135, 241-248.

30. Shi, S.; Ouyang, C.; Lei, M.; Tang, W. Effect of Mg-doping on the structural and electronic properties of LiCoO₂: A first-principles investigation. *J. Power Sources*. **2007**, *171*, 908-912.

31. Chung, S.-Y.; Bloking, J. T.; Chiang, Y.-M. Electronically conductive phospho-olivines as lithium storage electrodes. *Nat. Mater.* **2002**, *1*, 123-128.

32. Cheon, S.; Kwon, C.; Kim, D.; Hong, S.; Kim, H.; Kim, S. Effect of binary conductive agents in LiCoO₂ cathode on performances of lithium ion polymer battery. *Electrochim. Acta*. **2000**, *46*, 599-605.

33. Spahr, M. E.; Goers, D.; Leone, A.; Stallone, S.; Grivei, E. Development of carbon conductive additives for advanced lithium ion batteries. *J. Power Sources*. **2011**, *196*, 3404-3413.

34. Guoping, W.; Qingtang, Z.; Zuolong, Y.; MeiZheng, Q. The effect of different kinds of nano-carbon conductive additives in lithium ion batteries on the resistance and electrochemical behavior of the LiCoO₂ composite cathodes. *Solid State Ionics*. **2008**, *179*, 263-268.

35. Oh, S. W.; Myung, S. T.; Oh, S. M.; Oh, K. H.; Amine, K.; Scrosati, B.; Sun, Y. K. Double carbon coating of LiFePO₄ as high rate electrode for rechargeable lithium batteries. *Adv. Mater.* **2010**, *22*, 4842-4845.

36. Wang, X.; Cao, X.; Bourgeois, L.; Guan, H.; Chen, S.; Zhong, Y.; Tang, D. M.; Li, H.; Zhai, T.; Li, L. N-Doped Graphene-SnO₂ Sandwich Paper for High-Performance Lithium-Ion Batteries. *Adv. Funct. Mater.* **2012**, *22*, 2682-2690.

37. Choi, D. W.; Wang, D. H.; Bae, I. T.; Xiao, J.; Nie, Z. M.; Wang, W.; Viswanathan, V. V.; Lee, Y. J.; Zhang, J. G.; Graff, G. L.; Yang, Z. G.; Liu, J. LiMnPO₄ Nanoplate Grown via Solid-State Reaction in Molten Hydrocarbon for Li-Ion Battery Cathode. *Nano Lett.* **2010**, *10*, 2799-2805.

38. Oh, S. M.; Oh, S. W.; Yoon, C. S.; Scrosati, B.; Amine, K.; Sun, Y. K. High-Performance Carbon-LiMnPO₄ Nanocomposite Cathode for Lithium Batteries. *Adv. Funct. Mater.* **2010**, *20*, 3260-3265.

39. Yoo, H.; Jo, M.; Jin, B. S.; Kim, H. S.; Cho, J. Flexible Morphology Design of 3D-Macroporous LiMnPO₄ Cathode Materials for Li Secondary Batteries: Ball to Flake. *Adv. Energy Mater.* **2011**, *1*, 347-351.

40. Li, G.; Azuma, H.; Tohda, M. LiMnPO₄ as the cathode for lithium batteries. *Electrochem. Solid-State Lett.* **2002**, *5*, A135-A137.

41. Delacourt, C.; Poizot, P.; Morcrette, M.; Tarascon, J.-M.; Masquelier, C. One-step low-temperature route for the preparation of electrochemically active LiMnPO₄ powders. *Chem. Mater.* **2004**, *16*, 93-99.

42. Bramnik, N. N.; Ehrenberg, H. Precursor-based synthesis and electrochemical performance of LiMnPO₄. *J. Alloys Compd.* **2008**, *464*, 259-264.

43. Martha, S. K.; Grinblat, J.; Haik, O.; Zinigrad, E.; Drezen, T.; Miners, J. H.; Exnar, I.; Kay, A.; Markovsky, B.; Aurbach, D. $\text{LiMn}_0.8\text{Fe}_0.2\text{PO}_4$: an advanced cathode material for rechargeable lithium batteries. *Angew. Chem. Int. Ed.* **2009**, *48*, 8559-8563.
44. Martha, S.; Markovsky, B.; Grinblat, J.; Gofer, Y.; Haik, O.; Zinigrad, E.; Aurbach, D.; Drezen, T.; Wang, D.; Deghenghi, G. LiMnPO_4 as an advanced cathode material for rechargeable lithium batteries. *J. Electrochem. Soc.* **2009**, *156*, A541-A552.
45. Wang, D.; Buqa, H.; Crouzet, M.; Deghenghi, G.; Drezen, T.; Exnar, I.; Kwon, N.-H.; Miners, J. H.; Poletto, L.; Grätzel, M. High-performance, nano-structured LiMnPO_4 synthesized via a polyol method. *J. Power Sources.* **2009**, *189*, 624-628.
46. Delacourt, C.; Laffont, L.; Bouchet, R.; Wurm, C.; Leriche, J.-B.; Morcrette, M.; Tarascon, J.-M.; Masquelier, C. Toward understanding of electrical limitations (electronic, ionic) in LiMPO_4 (M= Fe, Mn) electrode materials. *J. Electrochem. Soc.* **2005**, *152*, A913-A921.
47. Needham, S.; Wang, G.; Liu, H.; Drozd, V.; Liu, R. Synthesis and electrochemical performance of doped LiCoO_2 materials. *J. Power Sources.* **2007**, *174*, 828-831.
48. Park, O. K.; Cho, Y.; Lee, S.; Yoo, H.-C.; Song, H.-K.; Cho, J. Who will drive electric vehicles, olivine or spinel? *Energy Environ. Sci.* **2011**, *4*, 1621-1633.
49. Padhi, A. K.; Nanjundaswamy, K.; Goodenough, J. Phospho-olivines as positive-electrode materials for rechargeable lithium batteries. *J. Electrochem. Soc.* **1997**, *144*, 1188-1194.
50. Amine, K.; Yasuda, H.; Yamachi, M. Olivine LiCoPO_4 as 4.8 V electrode material for lithium batteries. *Electrochem. Solid-State Lett.* **2000**, *3*, 178-179.
51. Wolfenstine, J.; Allen, J. $\text{Ni}^{3+}/\text{Ni}^{2+}$ redox potential in LiNiPO_4 . *J. Power Sources.* **2005**, *142*, 389-390.
52. Lee, M.-H.; Kim, J.-Y.; Song, H.-K. A hollow sphere secondary structure of LiFePO_4 nanoparticles. *Chem. Commun.* **2010**, *46*, 6795-6797.
53. Rissouli, K.; Benkhouja, K.; Ramos-Barrado, J.; Julien, C. Electrical conductivity in lithium orthophosphates. *Materials Science and Engineering: B.* **2003**, *98*, 185-189.
54. Morgan, D.; Van der Ven, A.; Ceder, G. Li conductivity in Li_xMPO_4 (M= Mn, Fe, Co, Ni) olivine materials. *Electrochem. Solid-State Lett.* **2004**, *7*, A30-A32.
55. Dean, J. A. In *Lange's Handbook of Chemistry*; Eds.; McGraw-Hill: New York, 1985; pp.
56. Boyle, F. W.; Lindsay, W. L. Diffraction Patterns and Solubility Products of Several Divalent Manganese Phosphate-Compounds. *Soil Sci. Soc. Am. J.* **1985**, *49*, 761-766.
57. Maldonado-Hodar, F.; Moreno-Castilla, C.; Rivera-Utrilla, J.; Hanzawa, Y.; Yamada, Y. Catalytic graphitization of carbon aerogels by transition metals. *Langmuir.* **2000**, *16*, 4367-4373.
58. Lee, C. J.; Park, J.; Jeong, A. Y. Catalyst effect on carbon nanotubes synthesized by thermal

- chemical vapor deposition. *Chem. Phys. Lett.* **2002**, *360*, 250-255.
59. Poizot, P.; Laruelle, S.; Grugeon, S.; Dupont, L.; Tarascon, J. M. Nano-sized transition-metaloxides as negative-electrode materials for lithium-ion batteries. *Nature.* **2000**, *407*, 496-499.
60. Cabana, J.; Monconduit, L.; Larcher, D.; Palacin, M. R. Beyond intercalation-based Li-ion batteries: the state of the art and challenges of electrode materials reacting through conversion reactions. *Adv. Mater.* **2010**, *22*, E170-192.
61. Morin, F. Electrical Properties of α -Fe₂O₃ and α -Fe₂O₃ Containing Titanium. *Phys. Rev.* **1951**, *83*, 1005-1010.
62. Behera, S. K. Facile synthesis and electrochemical properties of Fe₃O₄ nanoparticles for Li ion battery anode. *J. Power Sources.* **2011**, *196*, 8669-8674.
63. Lee, G. H.; Park, J. G.; Sung, Y. M.; Chung, K. Y.; Cho, W. I.; Kim, D. W. Enhanced cycling performance of an Fe⁰/Fe₃O₄ nanocomposite electrode for lithium-ion batteries. *Nanotechnology.* **2009**, *20*, 295205.
64. Wang, L.; Yu, Y.; Chen, P. C.; Zhang, D. W.; Chen, C. H. Electrospinning synthesis of C/Fe₃O₄ composite nanofibers and their application for high performance lithium-ion batteries. *J. Power Sources.* **2008**, *183*, 717-723.
65. Li, J.; Dahn, H. M.; Krause, L. J.; Le, D.-B.; Dahn, J. R. Impact of Binder Choice on the Performance of α -Fe[_{sub 2}]O[_{sub 3}] as a Negative Electrode. *J. Electrochem. Soc.* **2008**, *155*, A812.
66. Xiong, Q. Q.; Tu, J. P.; Lu, Y.; Chen, J.; Yu, Y. X.; Qiao, Y. Q.; Wang, X. L.; Gu, C. D. Synthesis of Hierarchical Hollow-Structured Single-Crystalline Magnetite (Fe₃O₄) Microspheres: The Highly Powerful Storage versus Lithium as an Anode for Lithium Ion Batteries. *J. Phys. Chem. C.* **2012**, *116*, 6495-6502.
67. Chen, Y. X.; He, L. H.; Shang, P. J.; Tang, Q. L.; Liu, Z. Q.; Liu, H. B.; Zhou, L. P. Micro-sized and Nano-sized Fe₃O₄ Particles as Anode Materials for Lithium-ion Batteries. *J. Mater. Sci. Technol.* **2011**, *27*, 41-45.
68. Balan, L.; Ghanbaja, J.; Willmann, P.; Billaud, D. Novel tin-graphite composites as negative electrodes of Li-ion batteries. *Carbon.* **2005**, *43*, 2311-2316.
69. Sun, X. M.; Liu, J. F.; Li, Y. D. Oxides@C core-shell nanostructures: One-pot synthesis, rational conversion, and Li storage property. *Chem. Mater.* **2006**, *18*, 3486-3494.
70. Taberna, P. L.; Mitra, S.; Poizot, P.; Simon, P.; Tarascon, J. M. High rate capabilities Fe₃O₄-based Cu nano-architected electrodes for lithium-ion battery applications. *Nat. Mater.* **2006**, *5*, 567-573.
71. Ji, L.; Zhang, X. Manganese oxide nanoparticle-loaded porous carbon nanofibers as anode materials for high-performance lithium-ion batteries. *Electrochem. Commun.* **2009**, *11*, 795-798.
72. Muraliganth, T.; Vadivel Murugan, A.; Manthiram, A. Facile synthesis of carbon-decorated single-

crystalline Fe₃O₄ nanowires and their application as high performance anode in lithium ion batteries. *Chem. Commun.* **2009**, 7360-7362.

73. Ban, C.; Wu, Z.; Gillaspie, D. T.; Chen, L.; Yan, Y.; Blackburn, J. L.; Dillon, A. C. Nanostructured Fe₃O₄/SWNT electrode: Binder-free and high-rate li-ion anode. *Adv. Mater.* **2010**, *22*, E145-149.

74. Zhou, G.; Wang, D.-W.; Li, F.; Zhang, L.; Li, N.; Wu, Z.-S.; Wen, L.; Lu, G. Q.; Cheng, H.-M. Graphene-Wrapped Fe₃O₄ Anode Material with Improved Reversible Capacity and Cyclic Stability for Lithium Ion Batteries. *Chem. Mater.* **2010**, *22*, 5306-5313.

75. Chen, W.; Li, S.; Chen, C.; Yan, L. Self-assembly and embedding of nanoparticles by in situ reduced graphene for preparation of a 3D graphene/nanoparticle aerogel. *Adv. Mater.* **2011**, *23*, 5679-5683.

76. Kang, E.; Jung, Y. S.; Cavanagh, A. S.; Kim, G.-H.; George, S. M.; Dillon, A. C.; Kim, J. K.; Lee, J. Fe₃O₄ Nanoparticles Confined in Mesocellular Carbon Foam for High Performance Anode Materials for Lithium-Ion Batteries. *Adv. Funct. Mater.* **2011**, *21*, 2430-2438.

77. Liu, J.; Zhou, Y.; Liu, F.; Liu, C.; Wang, J.; Pan, Y.; Xue, D. One-pot synthesis of mesoporous interconnected carbon-encapsulated Fe₃O₄ nanospheres as superior anodes for Li-ion batteries. *RSC Adv.* **2012**, *2*, 2262.

78. Lee, K. T.; Jung, Y. S.; Oh, S. M. Synthesis of tin-encapsulated spherical hollow carbon for anode material in lithium secondary batteries. *J. Am. Chem. Soc.* **2003**, *125*, 5652-5653.

79. NuLi, Y.; Zeng, R.; Zhang, P.; Guo, Z.; Liu, H. Controlled synthesis of α -Fe₂O₃ nanostructures and their size-dependent electrochemical properties for lithium-ion batteries. *J. Power Sources.* **2008**, *184*, 456-461.

80. Wang, Z.; Luan, D.; Madhavi, S.; Li, C. M.; Lou, X. W. α -Fe₂O₃ nanotubes with superior lithium storage capability. *Chem. Commun.* **2011**, *47*, 8061-8063.

81. Wang, Z.; Luan, D.; Madhavi, S.; Hu, Y.; Lou, X. W. Assembling carbon-coated α -Fe₂O₃ hollow nanohorns on the CNT backbone for superior lithium storage capability. *Energy Environ. Sci.* **2012**, *5*, 5252.

82. Titirici, M. M.; Antonietti, M.; Thomas, A. A generalized synthesis of metal oxide hollow spheres using a hydrothermal approach. *Chem. Mater.* **2006**, *18*, 3808-3812.

83. Chen, D.; Ji, G.; Ma, Y.; Lee, J. Y.; Lu, J. Graphene-encapsulated hollow Fe₃O₄ nanoparticle aggregates as a high-performance anode material for lithium ion batteries. *ACS Appl. Mater. Interfaces.* **2011**, *3*, 3078-3083.

84. Wang, B.; Chen, J. S.; Wu, H. B.; Wang, Z.; Lou, X. W. Quasiemulsion-templated formation of α -Fe₂O₃ hollow spheres with enhanced lithium storage properties. *J. Am. Chem. Soc.* **2011**, *133*, 17146-17148.

85. Chen, Y.; Xia, H.; Lu, L.; Xue, J. Synthesis of porous hollow Fe₃O₄ beads and their applications in

- lithium ion batteries. *J. Mater. Chem.* **2012**, *22*, 5006.
86. Koo, B.; Xiong, H.; Slater, M. D.; Prakapenka, V. B.; Baasubramanian, M.; Podsiadlo, P.; Johnson, C. S.; Rajh, T.; Shevchenko, E. V. Hollow Iron Oxide Nanoparticles for Application in Lithium Ion Batteries. *Nano Lett.* **2012**, *12*, 2429-2435.
87. Zhang, Q.; Shi, Z.; Deng, Y.; Zheng, J.; Liu, G.; Chen, G. Hollow Fe₃O₄/C spheres as superior lithium storage materials. *J. Power Sources.* **2012**, *197*, 305-309.
88. Zhang, W.; Wang, X.; Zhou, H.; Chen, J.; Zhang, X. Fe₃O₄-C open hollow sphere assembled by nanocrystals and its application in lithium ion battery. *J. Alloys Compd.* **2012**, *521*, 39-44.
89. Chou, S. L.; Wang, J. Z.; Chen, Z. X.; Liu, H. K.; Dou, S. X. Hollow hematite nanosphere/carbon nanotube composite: mass production and its high-rate lithium storage properties. *Nanotechnology.* **2011**, *22*, 265401.
90. Zhao, Y.; Li, J.; Wu, C.; Ding, Y.; Guan, L. A Yolk-Shell Fe₃O₄@ C Composite as an Anode Material for High-Rate Lithium Batteries. *ChemPlusChem.* **2012**, *77*, 748-751.
91. Lou, X. W.; Wang, Y.; Yuan, C.; Lee, J. Y.; Archer, L. A. Template-Free Synthesis of SnO₂ Hollow Nanostructures with High Lithium Storage Capacity. *Adv. Mater.* **2006**, *18*, 2325-2329.
92. Sun, X.; Li, Y. Ga₂O₃ and GaN semiconductor hollow spheres. *Angew. Chem.* **2004**, *43*, 3827-3831.
93. Lee, M. H.; Kim, J. Y.; Song, H. K. A hollow sphere secondary structure of LiFePO₄ nanoparticles. *Chem. Commun.* **2010**, *46*, 6795-6797.
94. Zhang, W.-M.; Wu, X.-L.; Hu, J.-S.; Guo, Y.-G.; Wan, L.-J. Carbon Coated Fe₃O₄ Nanospindles as a Superior Anode Material for Lithium-Ion Batteries. *Adv. Funct. Mater.* **2008**, *18*, 3941-3946.
95. Li, B.; Cao, H.; Shao, J.; Qu, M. Enhanced anode performances of the Fe₃O₄-carbon-rGO three dimensional composite in lithium ion batteries. *Chem. Commun.* **2011**, *47*, 10374-10376.
96. Zhou, J.; Song, H.; Ma, L.; Chen, X. Magnetite/graphene nanosheet composites: interfacial interaction and its impact on the durable high-rate performance in lithium-ion batteries. *RSC Adv.* **2011**, *1*, 782.
97. Sun, X.; Li, Y. Colloidal carbon spheres and their core/shell structures with noble-metal nanoparticles. *Angew. Chem.* **2004**, *43*, 597-601.
98. Laruelle, S.; Grugeon, S.; Poizot, P.; Dolle, M.; Dupont, L.; Tarascon, J. On the origin of the extra electrochemical capacity displayed by MO/Li cells at low potential. *J. Electrochem. Soc.* **2002**, *149*, A627-A634.
99. Xu, X.; Cao, R.; Jeong, S.; Cho, J. Spindle-like mesoporous α-Fe₂O₃ anode material prepared from MOF template for high-rate lithium batteries. *Nano Lett.* **2012**, *12*, 4988-4991.
100. Banerjee, A.; Singh, U.; Aravindan, V.; Srinivasan, M.; Ogale, S. Synthesis of CuO nanostructures from Cu-based metal organic framework (MOF-199) for application as anode for Li-ion batteries. *Nano*

Energy. **2013**, *2*, 1158-1163.

101. Liu, B.; Zhang, X.; Shioyama, H.; Mukai, T.; Sakai, T.; Xu, Q. Converting cobalt oxide subunits in cobalt metal-organic framework into agglomerated Co₃O₄ nanoparticles as an electrode material for lithium ion battery. *J. Power Sources*. **2010**, *195*, 857-861.

102. Kim, T.-H.; Park, H.-S.; Lee, M.-H.; Lee, S.-Y.; Song, H.-K. Restricted growth of LiMnPO₄ nanoparticles evolved from a precursor seed. *J. Power Sources*. **2012**, *210*, 1-6.

103. Lu, Y.; Wang, Y.; Zou, Y.; Jiao, Z.; Zhao, B.; He, Y.; Wu, M. Macroporous Co₃O₄ platelets with excellent rate capability as anodes for lithium ion batteries. *Electrochem. Commun.* **2010**, *12*, 101-105.

104. Wang, X.; Guan, H.; Chen, S.; Li, H.; Zhai, T.; Tang, D.; Bando, Y.; Golberg, D. Self-stacked Co₃O₄ nanosheets for high-performance lithium ion batteries. *Chem. Commun.* **2011**, *47*, 12280-12282.

105. Lee, K. J.; Kim, T.-H.; Kim, T. K.; Lee, J. H.; Song, H.-K.; Moon, H. R. Preparation of Co₃O₄ electrode materials with different microstructures via pseudomorphic conversion of Co-based metal-organic frameworks. *Journal of Materials Chemistry A*. **2014**, *2*, 14393-14400.

106. Poizot, P.; Laruelle, S.; Grugeon, S.; Dupont, L.; Tarascon, J. Nano-sized transition-metal oxides as negative-electrode materials for lithium-ion batteries. *Nature*. **2000**, *407*, 496-499.

107. Jiao, F.; Bao, J.; Bruce, P. G. Factors influencing the rate of Fe₂O₃ conversion reaction. *Electrochem. Solid-State Lett.* **2007**, *10*, A264-A266.

108. Chen, Y.; He, L.; Shang, P.; Tang, Q.; Liu, Z.; Liu, H.; Zhou, L. Micro-sized and nano-sized Fe₃O₄ particles as anode materials for lithium-ion batteries. *J. Mater. Sci. Technol.* **2011**, *27*, 41-45.

109. Manthiram, A. Materials Aspects: An Overview. In *LITHIUM BATTERIES: Science and Technology*; Nazri, G.-A., Pistoia, G., Eds.; Springer: New York, 2009; pp 35.

110. Kim, T. H.; Park, J. S.; Chang, S. K.; Choi, S.; Ryu, J. H.; Song, H. K. The current move of lithium ion batteries towards the next phase. *Adv. Energy Mater.* **2012**, *2*, 860-872.

111. Ding, N.; Xu, J.; Yao, Y.; Wegner, G.; Fang, X.; Chen, C.; Lieberwirth, I. Determination of the diffusion coefficient of lithium ions in nano-Si. *Solid State Ionics*. **2009**, *180*, 222-225.

112. Ruffo, R.; Hong, S. S.; Chan, C. K.; Huggins, R. A.; Cui, Y. Impedance analysis of silicon nanowire lithium ion battery anodes. *J. Phys. Chem. C*. **2009**, *113*, 11390-11398.

113. Park, J.-S.; Lee, M.-H.; Jeon, I.-Y.; Park, H.-S.; Baek, J.-B.; Song, H.-K. Edge-Exfoliated Graphites for Facile Kinetics of Delithiation. *ACS Nano*. **2012**, *6*, 10770-10775.

114. Tossici, R.; Berrettoni, M.; Rosolen, M.; Marassi, R. Electrochemistry of KC8 in Lithium-Containing Electrolytes and Its Use in Lithium-Ion Cells *J. Electrochem. Soc.* **1997**, *144*, 186-192.

115. Ein-Eli, Y.; Koch, V. R. Chemical Oxidation: A Route to Enhanced Capacity in Li-Ion Graphite Anodes. *J. Electrochem. Soc.* **1997**, *144*, 2968-2973.

116. Menachem, C.; Wang, Y.; Flowers, J.; Peled, E.; Greenbaum, S. G. Characterization of lithiated

- natural graphite before and after mild oxidation. *J. Power Sources*. **1998**, *76*, 180-185.
117. Yoo, E.; Kim, J.; Hosono, E.; Zhou, H.-s.; Kudo, T.; Honma, I. Large Reversible Li Storage of Graphene Nanosheet Families for Use in Rechargeable Lithium Ion Batteries. *Nano Lett.* **2008**, *8*, 2277-2282.
118. Xiang, H. F.; Li, Z. D.; Xie, K.; Jiang, J. Z.; Chen, J. J.; Lian, P. C.; Wu, J. S.; Yu, Y.; Wang, H. H. Graphene sheets as anode materials for Li-ion batteries: preparation, structure, electrochemical properties and mechanism for lithium storage. *RSC Adv.* **2012**, *2*, 6792.
119. Mukhopadhyay, A.; Guo, F.; Tokranov, A.; Xiao, X.; Hurt, R. H.; Sheldon, B. W. Engineering of Graphene Layer Orientation to Attain High Rate Capability and Anisotropic Properties in Li-Ion Battery Electrodes. *Adv. Funct. Mater.* **2013**, *23*, 2397-2404.
120. You, S.; Sundqvist, B.; Talyzin, A. V. Enormous Lattice Expansion of Hummers Graphite Oxide in Alcohols at Low Temperatures. *ACS Nano*. **2013**, *7*, 1395-1399.
121. Stankovich, S.; Dikin, D. A.; Piner, R. D.; Kohlhaas, K. A.; Kleinhammes, A.; Jia, Y.; Wu, Y.; Nguyen, S. T.; Ruoff, R. S. Synthesis of graphene-based nanosheets via chemical reduction of exfoliated graphite oxide. *Carbon*. **2007**, *45*, 1558-1565.
122. Jo, K.; Lee, T.; Choi, H. J.; Park, J. H.; Lee, D. J.; Lee, D. W.; Kim, B.-S. Stable aqueous dispersion of reduced graphene nanosheets via non-covalent functionalization with conducting polymers and application in transparent electrodes. *Langmuir*. **2011**, *27*, 2014-2018.
123. McAllister, M. J.; Li, J.-L.; Adamson, D. H.; Schniepp, H. C.; Abdala, A. A.; Liu, J.; Herrera-Alonso, M.; Milius, D. L.; Car, R.; Prud'homme, R. K. Single sheet functionalized graphene by oxidation and thermal expansion of graphite. *Chem. Mater.* **2007**, *19*, 4396-4404.
124. Shin, Y.-R.; Jung, S.-M.; Jeon, I.-Y.; Baek, J.-B. The oxidation mechanism of highly ordered pyrolytic graphite in a nitric acid/sulfuric acid mixture. *Carbon*. **2012**, *50*, 1465-1476.
125. Ferrari, A. C.; Robertson, J. Interpretation of Raman spectra of disordered and amorphous carbon. *Physical Review B*. **2000**, *61*, 14095-14107.
126. Kudin, K. N.; Ozbas, B.; Schniepp, H. C.; Prud'homme, R. K.; Aksay, I. A.; Car, R. Raman Spectra of Graphite Oxide and Functionalized Graphene Sheets. *Nano Lett.* **2008**, *8*, 36-41.
127. Graf, D.; Molitor, F.; Ensslin, K.; Stampfer, C.; Jungen, A.; Hierold, C.; Wirtz, L. Spatially resolved raman spectroscopy of single- and few-layer graphene. *Nano Lett.* **2007**, *7*, 238-242.
128. Nazri, G.-A.; Yebka, B. Reactivity and safety aspects of carbonaceous anodes used in Lithium-ion batteries - Correlation of structural parameters and reactivity. In *Materials for Lithium-Ion Batteries*; Julien, C., Stoyanov, Z., Eds.; Kluwer Academic Publishers: The Netherlands, 2000; pp 162.
129. Pan, D. Y.; Wang, S.; Zhao, B.; Wu, M. H.; Zhang, H. J.; Wang, Y.; Jiao, Z. Li Storage Properties of Disordered Graphene Nanosheets. *Chem. Mater.* **2009**, *21*, 3136-3142.

130. Wang, S.; Zhang, Y.; Yang, L.; Liu, Q. The effect of carbonizing conditions on the capacity of carbon anodes derived from poly (p-phenylene). *Solid State Ionics*. **1996**, *86*, 919-924.
131. Winter, M.; Besenhard, J. O.; Spahr, M. E.; Novak, P. Insertion electrode materials for rechargeable lithium batteries. *Adv. Mater.* **1998**, *10*, 725-763.
132. Nazri, M.; Yebka, B.; Nazri, G.-A. Graphite-Electrolyte Interface in Lithium-Ion Batteries. In *LITHIUM BATTERIES: Science and Technology*; Nazri, G.-A., Pistoia, G., Eds.; Springer: New York, 2009; pp 203.

Chapter 8. Acknowledgements

모든 이름 위에 뛰어나신 하나님 아버지께 감사드립니다. 가는 길에 대한 확신이 사라지고 용기가 절망이 되어 포기하고 싶어질 때마다 말씀으로 저를 붙들어 주시고 제 뜻과 생각이 아닌 하나님의 뜻과 생각을 구하게 하심에 감사드립니다. 당신이 아니었으면 저는 지금 없습니다.

5년 6개월간 저의 집보다 더 편하게 생활한 eclat 연구실과 사람들에게 감사드립니다. 송현곤 지도교수님, 연구할 수 있는 좋은 조건을 마련해 주셔서 부족함 없이 연구할 수 있었습니다. 교수님의 기대만큼 부응해드리지 못해 죄송합니다. 치기 어린 모습에도 칭찬과 격려로 고민과 갈등 때마다 힘이 되어주신 김영수 박사님, 어리바리하던 나를 가장 잘 챙겨준 명희 누나, 나의 첫 사수이자 마지막 사수 진영 누나, 나한테 늘 툭툭 되고 철부지 누나였지만 유니스트를 떠나고 같은 처지가 되면서 서로에게 큰 힘이 되고 위로가 되어 준 려윤 누나. 우리의 우정은 여든까지도 쭉~! 나와 가장 많은 시간을 함께한 한샘 씨, 많이 부딪치기도 했지만, 서로의 날카로움을 다듬는 의미 있는 시간이었다고 생각합니다. 어린 동생을 선배 대접해주느라 수고 많았어요. 부디 잘 버텨내시길. 나의 입학 동기이자 졸업 동기 영훈이 형, 내가 하자는 건 뭐든 웃으며 받아준 Yes맨 정석이, 내 친구 정임이 평생 행복하게 해줘. 나를 가장 지지해주고 잘 따라 준 지은이, 하필 그 시기에 우리가 함께 있어 너에겐 늘 미안하다. 제멋대로지만 일에 대한 열정만큼은 그 누구보다 커서 내게 도전을 준 유일한 후배 치현이, 형이 실패한 길 답습하지 말고 부디 좋은 연구자가 되길 기도할게.

유니스트에서 만난 수많은 사람이 저에게 큰 자양분입니다. 엄격한 자기 관리와 연구에 대한 열정으로 늘 저를 채찍질해주신 조재필 교수님, 부드럽지만 강한 카리스마로 연구에 소소한 부분까지 가르쳐주신 문회리 교수님, 꼼꼼함과 자상함으로 저를 가르쳐주신

김병수 교수님, 학생보다 더 열심히 노력하며 공부하는 모습으로 감동을 주신 박수진 교수님, 그 외 수업과 연구로 만난 수많은 교수님께 감사드립니다. 또한, 수많은 동기와 선배에게도 감사드립니다. 애인 같은 보람이 형, 친구 같은 서진이 형, 내가 만나본 가장 착한 남자 재환이, 까칠한듯하지만 속은 누구보다 따뜻한 신호, 하나님 앞에 무릎 꿇을 줄 아는 사나이 정민이, 나의 부족한 지식을 끊임없이 채워주는 수경이 형, 고박 4년을 나와 한집에서 먹고 잔 나의 룸메 동우, 나의 훌륭한 코워커 은경이와 경주, 그리고 연구지원본부 선생님들, 특히 김영기 선생님 감사드립니다.

내게 신앙을 심어준 안종양 선생님, 글의 즐거움을 알게 해 준 김지연 국어 선생님, 진정한 스승의 모습을 보여주시고 박사 학위를 할 수 있는 가장 큰 원동력이 되어 주신 탁용석 교수님, 학교 연구실 밖 시야를 보여주신 성주환 박사님, 매주 하나님의 말씀으로 저를 붙잡아주시는 조 운 목사님, 미흡한 나를 세워주시고 무엇보다 강력한 말씀으로 가장 힘들었던 시기를 버틸 수 있게 해주신 윤용돈 목사님, 거룩함을 몸소 보여주시고 나의 폐부까지 들춰내어 가장 많이 혼내주신 유명화 목사님, 목사님 말씀들 기억하면서 죄수가 아닌 제자로 살고자 노력합니다.

'아들이 하는 일이라면 다 믿는다'며 깊이 묻지 않으시고 묵묵히 지켜봐 주신 아버지, 어머니 정말 감사드립니다. 그동안 고생 많으셨습니다. 평생 보답하며 살겠습니다. 애 셋 키우느라 자신의 삶을 잃어버린 듯 살지만 늘 긍정적인 웃음으로 동생을 응원해 준 우리 누나, 연구의 길을 먼저 걸어간 경험으로 좋은 조언을 아끼지 않는 자형, 삼촌 말은 잘 안 듣지만, 존재 그 자체로 예쁜 건우, 선우, 현우, 그리고, 2009년에 만나 나를 세상에서 가장 멋진 남자로 살게끔 내 옆에서 사랑해주고 기도해주고 가장 큰 힘을 주는 하나님이 주신 동역자 윤채진, 당신들은 내가 살아가는 이유입니다.

지면에 다 표현하지 못한 마음은 평생 갚으면서 살겠습니다.

Curriculum Vitae

Personal Data

Tae-Hee Kim

Jan/03/1985

Combined master's-doctoral course

School of Energy and Chemical Engineering, UNIST, Ulsan 689-798, Korea

ryan0103@unist.ac.kr

T) +82-52-217-2962, M) +82-10-2935-0177

ResearchGate: https://www.researchgate.net/profile/Tae_Hee_Kim3

EDUCATION

Ph.D., Energy Engineering (08/2015, Expected graduation)

Ulsan National Institute of Science and Technology (UNIST), Republic of Korea

Prof. Hyun-Kon Song, Advisor

B.S., Chemical Engineering (02/2010)

Inha University, Republic of Korea

Prof. Ggeon Joong Kim, Advisor

EXPERIENCE

Research Assistant (09/2011 - 08/2015)

Department of Energy Engineering, UNIST, Ulsan, Republic of Korea

Teaching Assistant (03/2010 - 08/2011)

Department of Energy Engineering, UNIST, Ulsan, Republic of Korea

TECHNICAL EXPERTISE

Electrochemistry

- Electrochemical impedance spectroscopy (EIS)
- *in situ* electrochemical impedance spectroscopy (EIS)
- Cyclic voltammetry, chronoamperometry, linear sweep voltammetry, galvanostatic cycling

Material Characterization

- Structural characterization technique: scanning electron microscope (SEM), transmission electron microscope (TEM)
- Spectroscopic technique: UV/visible spectroscopy, Fourier transform infrared spectroscopy (FT-IR), Zeta potential measurement
- Thermal analysis technique: thermal gravimetric analyzer (TGA)
- X-ray analysis: X-ray diffractometer (XRD)
- Dilatometer

Cell fabrication

- 2016/2032 coin-type cell

Publications

1. Chihyun Hwang, **Tae-Hee Kim**, Yoon-Gyo Cho, Jieun Kim, Hyun-Kon Song

Scientific Reports, 2015, 5, 8623

“All-in-one assembly based on 3D-intertangled and cross-jointed architectures of Si/Cu 1D-nanowires for lithium ion batteries”

2. Sinho Choi‡, **Tae-Hee Kim**‡, Jung-In Lee, Hyun-Kon Song, Soojin Park

ChemSusChem, 2014, 7, 3483

“General approach for high-power lithium-ion batteries: Multiscale lithographic patterning of electrodes”

‡ **Authors contributed equally**

3. Ju-Myung Kim, Han-Saem Park, Jang-Hoon Park, **Tae-Hee Kim**, Hyun-Kon Song*, Sang-Young Lee*

ACS Applied materials and interfaces, 2014, 6, 12789

“Conducting polymer-skinned electroactive materials of lithium ion batteries: Ready for mono-component electrodes without additional binders and conductive agents”

4. Kyung Joo Lee‡, **Tae-Hee Kim**‡, Tae Kyung Kim, Jae Hwa Lee, Hyun-Kon Song*, Hoi Ri Moon*

Journal of Materials Chemistry A, 2014, 2, 14393

“Preparation of Co₃O₄ electrode materials with different microstructures via pseudomorphic conversion of Co-based metal-organic frameworks”

‡ **Authors contributed equally**

5. **Tae-Hee Kim**‡, Eun Kyung Jeon‡, Younghoon Ko, Bo Yun Jang, Byeong-Su Kim, Hyun-Kon Song*

Journal of Materials Chemistry A, 2014, 2, 7600

“Enlarging the d-spacing of graphite and polarizing its surface charge for driving lithium ions fast”

‡ **Authors contributed equally**

6. Jieun Kim, Han-Saem Park, **Tae-Hee Kim**, Sung Yeol Kim, Hyun-Kon Song*

Physical Chemistry Chemical Physics, 2014, 16, 5295

“An inter-tangled network of redox-active and conducting polymers as a cathode for ultrafast rechargeable batteries”

7. **Tae-Hee Kim**, Hyun-Kon Song*

Electrochimica Acta, 2013, 105, 47

“Hollow versus nonhollow: the electrochemical preference in a case study of the conversion reaction of Fe_3O_4 ”

8. Han-Saem Park, **Tae-Hee Kim**, Myeong-Hee Lee, Hyun-Kon Song*

Journal of Materials Chemistry, 2012, 22, 20305

“Catalytic carbonization of an uncarbonizable precursor by transition metals in olivine cathode materials of lithium ion batteries”

9. **Tae-Hee Kim**, Jeong-Seok Park, Sung Kyun Chang, Seungdon Choi*, Ji Heon Ryu*, Hyun-Kon Song*

Advanced Energy Materials, 2012, 2, 860

“The current move of lithium ion batteries towards the next phase”

10. Myeong-Hee Lee, **Tae-Hee Kim**, Young-Soo Kim, Jeong-Seok Park, Hyun-Kon Song*

Journal of Materials Chemistry, 2012, 22, 8228

“Optimized evolution of a secondary structure of LiFePO_4 : Balancing between shape and impurity

11. **Tae-Hee Kim**, Han-Saem Park, Myeong-Hee Lee, Sang-Young Lee*, Hyun-Kon Song*

Journal of Power Sources, 2012, 210, 1

“Restricted growth of LiMnPO_4 nano particles evolved from a precursor seed”

12. Geun Gi Min, Younghoon Ko, **Tae-Hee Kim**, Hyun-Kon Song, Seung Bin Kim, Su-Moon Park*

Journal of The Electrochemical Society, 2011, 158, A1267

“Fourier transform electrochemical impedance spectroscopic studies on LiFePO_4 nanoparticles of hollow sphere secondary structures”

13. Viswanathan S. Saji, Young-Soo Kim, **Tae-Hee Kim**, Jaephil Cho, Hyun-Kon Song

Physical Chemistry Chemical Physics, 2011, 13, 19226

“One-dimensional (1D) nanostructured and nanocomposited LiFePO_4 : its perspective advantages for cathode materials of lithium ion batteries”

14. Young-Soo Kim, **Tae-Hee Kim**, Hochun Lee, Hyun-Kon Song*

Energy and Environmental Science, 2011, 4, 4038

“Electronegativity-induced enhancement of thermal stability by succinonitrile as an additive for Li ion batteries”

15. Myeong-Hee Lee, **Tae-Hee Kim**, Young-Soo Kim, Hyun-Kon Song*

The Journal of Physical Chemistry C, 2011, 115, 12255

“Precipitation revisited: shape control of LiFePO_4 nano particles by combinatorial precipitation”

Conferences

1. **Tae-Hee Kim**, Eun Kyung Jeon, Younghoon Ko, Byeong-Su Kim, Hyun-Kon Song

Oral, Spring Meeting of the Korean Electrochemical Society, Changwon, Korea (April 10~12, 2014).

"Enlarging d-spacing of graphite and polarizing its surface charge for driving lithium ions fast"

2. **Tae-Hee Kim**, Hyun-Kon Song

Oral, Spring Meeting of the Korean Electrochemical Society, Changwon, Korea (April 11~13, 2013)

"Hollow Versus Nonhollow: The Electrochemical Preference in a Case Study of The Conversion Reaction of Fe_3O_4 "

3. **Tae-Hee Kim**, Hyun-Kon Song*

Poster, IUPAC 8th International Conference on Novel Materials and their Synthesis, Xian, China (October 14~19, 2012)

"HOLLOW VERSUS NONHOLLOW: THE ELECTROCHEMICAL PREFERENCE IN A CASE STUDY OF THE CONVERSION REACTION OF Fe_3O_4 "

4. **Tae-Hee Kim** and Hyun-Kon Song

Poster, The 16th International Meeting on Lithium Batteries, ICC Jeju, Korea (June 17~22, 2012)

"A hollow $\text{Fe}_3\text{O}_4/\text{C}$ templated by carbon spheres as an anode material for high performance"

5. **Tae-Hee Kim**, Han-Saem Park, Myeong-Hee Lee and Hyun-Kon Song*

Poster, KECS-KCS joint winter symposium, Danyang, Korea (February 6, 2012)

"NANOSTRUCTURING LITHIUM METAL PHOSPHATES"

6. **Tae-Hee Kim**, Myeong-Hee Lee, Han-Sem Park, Young Soo Kim and Hyun-Kon Song*

Poster, 2nd Nano Today Conference, Marriott Resort Waikoloa, Hawaii, USA (December 11~15, 2011)

"Evolution of a secondary structure of LiMnPO_4 nanoparticles for a cathode material of lithium ion batteries"

7. **Tae-Hee Kim**, Han-Saem Park, Myeong-Hee Lee and Hyun-Kon Song

Poster, Korean Battery Society Meeting, Jeju, Korea (December 1~3, 2011)

"Nanostructuring of Lithium Metal Phosphate"

8. **Tae-Hee Kim**, Hyun-Kon Song

Oral, Korean Chemical Society Meeting, Jeju, Korea (April 28~29, 2011)

"Evolution of a secondary structure of LiMnPO_4 nanoparticles for a cathode material of lithium ion batteries"

Patents

1. Hyun-Kon Song, Myeong-Hee Lee, **Tae-Hee Kim**, Soojin Park, Jaephil Cho,

10-1205456

"METHOD OF PREPARING POSITIVE ACTIVE MATERIAL FOR RECHARGEABLE LITHIUM BATTERY USING IRON(III) OXIDE, POSITIVE ACTIVE MATERIAL FOR RECHARGEABLE LITHIUM BATTERY PREPARED BY USING THE METHOD, AND RECHARGEABLE LITHIUM BATTERY INCLUDING THE SAME"